Karlsruhe Institute of Technology

Simulation and First Experimental Tests of an Electron Beam Transport System for a Laser Wakefield Accelerator

Zur Erlangung des akademischen Grades eines
DOKTORS DER NATURWISSENSCHAFTEN

der Fakultät für Physik
des Karlsruher Institutes für Technologie (KIT)

genehmigte
DISSERTATION
von

Dipl.-Phys.
Christina Widmann
aus Schramberg

Tag der mündlichen Prüfung: 6. Mai 2016
Referent: **Prof. Dr. Anke-Susanne Müller**
Korreferent: **Prof. Dr. Marc Weber**

Contents

1. Introduction

Particle accelerators are an important tool in science. They provide radiation as light sources and allow studies of the elementary particles as colliders. The Large Hadron Collider (LHC), the world's largest accelerator located in Geneva, Switzerland, is used to gain further insights into the elements of matter. In 2012 a new particle, the Higgs boson, was discovered [Aad et al., 2012, Chatrchyan et al., 2012]. Its characteristics and the search for further particles explaining e.g. the nature of the dark matter are focus of the research with this collider.

At light sources the radiation generated by deflected particles is used for a variety of applications such as imaging, chemical and structural analysis of condensed matter but also e.g. for micro-fabrication. The wide spectral range of the radiation reaching from hard x-ray to the far infrared and terahertz, the short duration of the synchrotron light pulses and the high brilliance, i.e. the number of photons per time, area, solid angle and spectral bandwidth, are the unique characteristics of synchrotron radiation generated in light sources such as the European Synchrotron Radiation Facility (ESRF) in Grenoble, France. With these characteristics a vast variety of properties and states of matter and material including thin layers and biological tissue can be investigated with high precision and to study the temporal evolution of processes. Free electron lasers (FELs) such as the Linear Coherent Light Source (LCLS) in Standford, USA, and the Spring-8 Angstrom Compact Free Electron Laser (SACLA) in Japan provide shorter synchrotron light pulses with temporal and spatial coherence, which opens possibilities for even more applications.

These conventional accelerators are reliable tools nowadays, however, they are very large and their operation is costly. As an alternative one is looking for compact accelerating structures which reach similar parameters. The limiting factor in conventional accelerators are the radio-frequency cavities used for acceleration. The maximum gradient they provide is 100 MV/m. To accelerate an electron to an energy of 1 GeV at least an acceleration length of 10 m is required. For more compact accelerators the radio-frequency cavities have to be replaced by structures providing higher acceleration gradients.

One approach is the acceleration of electrons in the fields of a plasma wave: The electron density in the plasma is modulated by a laser pulse or a driving particle bunch. Thus a plasma wave is generated with accelerating gradients three to four orders of magnitude higher than in conventional accelerators. That reduces the acceleration length from 10 m to 1 cm or less for an electron energy of 1 GeV.

In 2004 for the first time electron bunches with a quasi-monoenergetic peak in the energy distribution were generated using the principle of laser wakefield acceleration [Faure et al., 2004, Geddes et al., 2004, Mangles et al., 2004], for which the plasma wave is driven by a high energy laser pulse. Apart from the compact design of the laser wakefield accelerator (LWFA), the emitted bunches are intrinsically ultra-short with a bunch length the range of some micrometers, thus high peak currents are achieved. These properties make LWFAs quite attractive as drivers for a compact radiation source or even FELs [Jaroszynski et al., 2006, Grüner et al., 2007].

For future colliders based on plasma wakefield acceleration studies and experiments are performed by the AWAKE collaboration at CERN [Gschwendtner et al., 2014]. The plasma wave here is generated by a proton driver bunch, which is generated in a conventional accelerator. In comparison to laser wakefield accelerators, the maximum acceleration length is much longer, thus higher electron energies can be achieved.

One of the major drawbacks of the LWFA technology compared to conventional accelerators is the broad energy distribution of the accelerated electrons with a relative energy spread in the order of some percent. It is therefore three to four orders of magnitude higher than in conventional accelerators. Furthermore the intrinsic divergence in the range of some milliradians is quite large. With these parameters it is difficult to shape and transport the bunches of the LWFA. For any application, however, a proper transport and matching of the beam is essential or, in other words, without a good beam transport system the beams of the LWFA cannot be used for any application.

In some experimental setups at LWFAs a set of permanent quadrupole magnets to focus the beam [Fuchs et al., 2009] or a combination of permanent and electromagnetic quadrupoles [Brunetti et al., 2010] are applied. For a FEL study a setup was proposed for focusing and chirping the bunches[a] [Maier et al., 2012]. The focusing is done with quadrupoles and thereafter the chirp is generated in a dipoles chicane. However, the focusing strength of the quadrupoles varies with the electron energy. That means in configurations consisting of a number of quadrupoles only a small energy bandwidth is properly focused. Hence, only a fraction of the electron bunch in a small energy band therefore matches the required parameters at the experiment and a large fraction of the

[a] Chirp means here the correlation of the electron energies and their longitudinal position.

particles is lost. In contrast, an effective beam transport system for the LWFA should accept an energy bandwidth adapted to the energy spread of the bunches.

For the LWFA in Jena a setup for the generation of monochromatic undulator radiation is developed. It is completely adapted to the parameters of the LWFA: It includes a transverse gradient undulator (TGU) to keep the narrow radiation bandwidth of the undulator radiation despite the energy spread. The LWFA and the TGU are connected by a complex beam transport system with an energy acceptance in the range of the energy bandwidth of the LWFA-bunches. To achieve this acceptance of the beam transport system the error generated by the energy dependence of the focusing strength of the magnets has to be corrected.

The TGU is designed such that it prevents the broadening of the narrow-band undulator radiation spectrum by the large relative energy spread of the bunches of the LWFA [Fuchert et al., 2012]: The electron beam entering the TGU is spectrally dispersed in direction of the deflection of the undulator, i.e. electrons of different energies are spatially separated in one transverse plane. The single energies are matched to the magnetic flux density amplitude of the undulator, which has a gradient in this transverse direction. Therefore the matched electrons of different energies all radiate at the same wavelength and the typical narrow-band spectrum of the undulator radiation is preserved. It is proposed to use this concept for a FEL driven by bunches of a LWFA [Huang et al., 2012].

The beam transport system has to fulfill several requirements for the adaption to the LWFA parameters: The electron bunch with the large relative energy spread and divergence must be captured and shaped such that the optimum beam parameters are matched at the entrance of the TGU including the required dispersion of the beam in the deflection plane. To match the beam parameters over the energy range covered by a single bunch a chromatic correction of the transport system is necessary.

In this thesis the design and first tests for the realization of such a beam transport system at the LWFA in Jena are presented. Compact, strong focusing magnets capture the beam of the LWFA, transport it and focus it to the TGU with the required parameters. With the implementation of sextupole magnets for the compensation of the chromatic error of the quadrupoles the energy bandwidth accepted by the beam transport system can be extended to an energy range of about one percent, which is slightly below the measured energy spread of the bunches at the LWFA. In first experimental tests of the beam transport system it was shown that a simplified linear system can be realized and the quadrupoles can be aligned using the beam of the LWFA.

The design consideration, simulations and experiments are presented in the following chapters of this thesis. Chapter 2 gives an overview of the physical background

and the methods used, in chapter 3 the working principle of the TGU is explained and the conceptual design for the realization of a radiation source with a TGU is presented. Furthermore all components of the experimental setup at the LWFA in Jena are described including the LWFA itself, the superconducting TGU and the components of the beam transport system. The initial parameters of the LWFA and the required target parameters at the TGU are discussed in chapter 4. In chapter 5 the layout for the beam transport system and the simulations performed for the optimization are presented. In chapter 6 the results of the first experimental tests of the beam transport system are summarized.

2. Basic Definitions and Equations

In this thesis the design and optimization of a beam transport system from a laser wakefield accelerator (LWFA) to a transverse gradient undulator (TGU) are discussed. Therefore the basic terms and definitions for the description of an electron beam in the beam transport system and inside the undulator, the characteristics and properties of undulator radiation and those of the electron bunches generated in a LWFA are necessary. In this chapter these basic definitions are given with the equations used.

In section 2.1 a short introduction to the beam dynamics of charged particle beams is given. In section 2.2 the working principle of undulators and the characteristics of their radiation is summarized. In section 2.3 the acceleration process in a LWFA is described.

2.1. Dynamics of Charged Particle Beams

For any setup using particle beams the guiding and focusing of these beams is essential. A transport system has to be designed such that the required parameters of the particle beam at the position of the experiment such as beam size and angle of incidence are matched.

In this section the basic equations are summarized that are used in this thesis to design a transport system for a bunch of electrons moving at ultra-relativistic velocities. Ultra-relativistic here means that the total energy E_{tot} of the electrons is significantly larger than the rest energy E_0, i.e. that the relativistic gamma factor γ_e holds $\gamma_e = E_{tot}/E_0 \gg 1$. The electrons are almost moving at the speed of light, i.e. the relativistic velocity $\beta_e = v_e/c$ is approximately unity.

The definitions and argumentations in general follow the description of D.C. Carey [Carey, 1986a] and H. Wiedemann [Wiedemann, 2003].

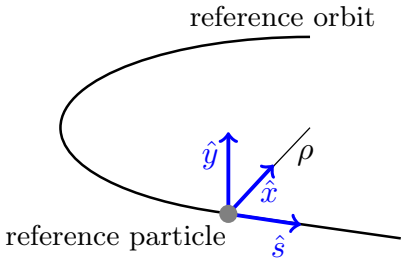

Figure 2.1.: Co-moving coordinate system for the particles in a bunch: The reference particle is its origin. ρ is the Larmor radius.

2.1.1. The Coordinate System

The force acting on a particle with charge q in an electromagnetic field is the *Lorentz force*

$$\vec{F}_L = q\left(\vec{E} + \vec{v} \times \vec{B}\right). \tag{2.1}$$

In particle accelerators in general electric fields are used for the acceleration of the particle, i.e. the increase of the longitudinal momentum. The guiding and deflection in transverse direction is done with magnetic fields.

In a homogeneous magnetic field $\vec{B}$ a particle with momentum p moving in the plane perpendicular to the magnetic field lines is deflected by the Lorenz force and moves on a circle with the *Larmor radius*

$$\rho_L = \frac{p}{qB}. \tag{2.2}$$

The location and momentum of the particle are defined by six coordinates, the three local coordinates and the momentum along each of the coordinate axes. The time is eliminated in this system by replacing it with the distance s the particle travels during a certain time interval. This six-dimensional space is called *phase space*.

For the description of a particle bunch a orthogonal coordinate system co-moving with the reference particle shown in Fig. 2.1 is used. The reference particle is a particle with the design momentum. Its trajectory defines the reference orbit, which is determined by the momentum of the reference particle and the deflection of the bending magnets. The reference particle has the longitudinal momentum p_0 and per definition no transverse momenta. The path length along the reference orbit is described with the coordinate s.

The coordinates of other particles of the bunch are defined relative to the reference particle: x and y are the transverse displacement in the plane perpendicular to the

reference momentum, where x is usually the deflection plane of the bending magnets. The longitudinal displacement is l. Instead of the transverse momenta the fraction of each momentum and the reference momentum is used, i.e.

$$x' = \frac{p_x}{p_0} \quad \text{and} \quad y' = \frac{p_y}{p_0}. \tag{2.3}$$

This fraction is equivalent to the angle to the reference orbit if the transverse momenta are small compared to the longitudinal momentum. The deviation of the longitudinal momentum of the electron to the reference momentum is given by the momentum deviation δ with

$$p = p_0(1 + \delta). \tag{2.4}$$

A particle of the bunch is therefore defined by the vector $(x, x', y, y', l, \delta)^T$. A bunch consisting of several particles occupies a certain volume in phase space.

2.1.2. The Linear Equation of Motion

For the linear equation of motion only the terms of the magnetic fields that are constant or depend linearly on the transverse coordinates are considered. Furthermore mid plane symmetry is assumed with respect to the x-z-plane[a], in which the reference orbit is located. That means the scalar magnetic potential Φ with $\vec{B} = \vec{\nabla}\Phi$ is an odd function in y and an even function in x and z with $\Phi(x, y, z) = \Phi(-x, y, z) = -\Phi(x, -y, z) = \Phi(x, y, -z)$. With this assumption a constant field, that does not vanish in the mid plane, is only allowed in y direction.

The resulting linear equations of motion of the two transverse planes for the longitudinal coordinate s are therefore given by

$$x'' + K_x^2(s)x = \frac{1}{\rho}(s)\delta \tag{2.5}$$

$$y'' + K_y^2(s)y = 0, \tag{2.6}$$

where ρ is the deflection radius and K contains the terms of the magnetic fields. Note that the derivative is with respect to s. In the following the variable u is used instead of x or y for equations valid for both transverse planes. The solution of the homogeneous equation of motion is a linear combination of the sine-like solution $S(s)$ and the cosine-

[a] For the description of the magnets and their fields the usual Cartesian coordinate system with the longitudinal coordinate z is used.

like solution $C(s)$[b]:

$$C(s) = \cos(K_u s) \quad \text{and} \quad S(s) = \frac{1}{K}\sin(K_u s) \qquad \text{for } K_u^2 > 0 \tag{2.7}$$

$$C(s) = \cosh(|K_u|s) \quad \text{and} \quad S(s) = \frac{1}{|K|}\sinh(|K_u|s) \qquad \text{for } K_u^2 < 0 \tag{2.8}$$

The inhomogeneous equation in x is solved by the solution of the homogeneous equation of motion plus one explicit solution for the inhomogeneous case e.g. given by the Green's function, for this case

$$D_x(s) = \int_0^s \frac{1}{\rho}(\xi)\left(C_x(\xi)S_x(s) - C_x(s)S_x(\xi)\right) d\xi. \tag{2.9}$$

D is called *dispersion function* and describes the transverse position offset of a particle due to a momentum deviation δ from the reference momentum.

The solutions of equation 2.5 and 2.6 can be expressed by matrices and the initial parameters u_0 and u_0':

$$\begin{pmatrix} u \\ u' \\ \delta \end{pmatrix} = \begin{pmatrix} C(s) & S(s) & D(s) \\ C'(s) & S'(s) & D'(s) \\ 0 & 0 & 1 \end{pmatrix} \begin{pmatrix} u_0 \\ u_0' \\ \delta \end{pmatrix} \tag{2.10}$$

The longitudinal offset of an ultra-relativistic particle is particles given by the path length difference of the trajectory.[c] In first order approximation three terms influence this parameter: the starting position x_0, the initial angle x_0' and the momentum deviation δ with

$$\begin{aligned}(l|x_0) &= \int_0^s C_x(s)\frac{1}{\rho(s)}ds \\ (l|x_0') &= \int_0^s S_x(s)\frac{1}{\rho(s)}ds \\ (l|x_0) &= \int_0^s D_x(s)\frac{1}{\rho(s)}ds.\end{aligned}$$

With these three matrix elements the transfer matrix R for all parameters of a particle

[b] The sine-like solution has the initial condition $S(0) = 0$ and $S'(0) = 1$, the cosine-like solution $C(0) = 1$ and $C'(0) = 0$.

[c] As all particles are moving approximately at the speed of light the velocity difference can be neglected.

in a system with mid plane symmetry is given by

$$\begin{pmatrix} x(s) \\ x'(s) \\ y(s) \\ y'(s) \\ l(s) \\ \delta \end{pmatrix} = \begin{pmatrix} C_x(s) & S_x(s) & 0 & 0 & 0 & D_x(s) \\ C'_x(s) & S'_x(s) & 0 & 0 & 0 & D'_x(s) \\ 0 & 0 & C_y(s) & S_y(s) & 0 & 0 \\ 0 & 0 & C'_y(s) & S'_y(s) & 0 & 0 \\ (l|x_0) & (l|x'_0) & 0 & 0 & 1 & (l|\delta) \\ 0 & 0 & 0 & 0 & 0 & 1 \end{pmatrix} \begin{pmatrix} x_0 \\ x'_0 \\ y_0 \\ y'_0 \\ l_0 \\ \delta \end{pmatrix}. \tag{2.11}$$

By multiplying the transfer matrices of each element of an optical lattice, e.g. of the magnets and drift spaces in between, the transfer matrix of the whole transport system can be determined. For each magnet a single parameter for the strength is given in K. The field has therefore a rectangular shape in longitudinal direction and fringe fields are neglected. This model for the magnets is called the *hard edge model*. The explicit matrices of different elements are given in the next subsection.

The matrix elements of equation 2.11 are also referred to as R_{ij}. The parameter R_{56} for example gives the correlation of the longitudinal path length difference to the momentum deviation δ, which leads to a lengthening of the bunch if it does not vanish.

2.1.3. Different Elements and their Transfer Matrices

To calculate the linear transfer matrix of an accelerator or a beam transport system the matrices of the different elements along the beam path are multiplied. In this section the transfer matrices of the elements and magnets relevant for this thesis are summarized with the according. I restricted this summary to the so-called upright multipoles with mid plane symmetry. Since in this case the particle dynamics in the two transverse directions are decoupled, it is sufficient to discuss the 2×2 matrices for each transverse sub-space or, in case of a non-vanishing D the 3×3 representation (equation 2.10). For the rotated multipole fields I refer to the common literature, e.g. [Carey, 1986a, Wiedemann, 2003, Rossbach and Schmueser, 1994a].

Before giving the fields and transfer matrices for the magnets the simplest element, the drift space, is introduced.

Drift Space Along a drift space, i.e. a region without electric or magnetic fields, the electron moves with a constant momentum. Therefore the angle to the axis is constant, i.e. $u'(s) = u'_0$, but the transverse position changes linearly with the distance Δs traveled, i.e. $u(s) = u_0 + u'_0 \Delta s$. The transfer matrix for a drift space of length L is given

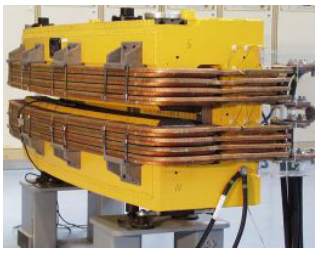

(a) Dipole

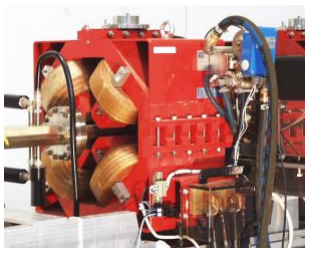

(b) Quadrupole

(c) Sextupole

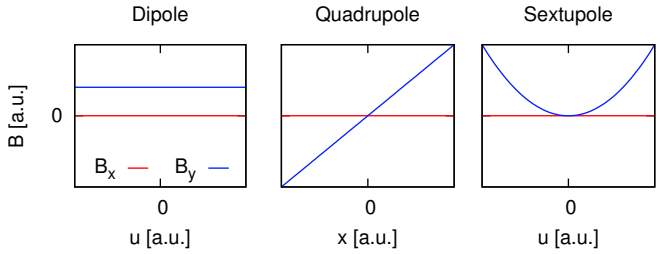

(d) Magnetic Field Components Along the Coordinat Axes

Figure 2.2.: (a) Dipole, (b) quadrupole and (c) sextupole of the synchrotron ANKA [ANKA Homepage, 2016], a conventional synchrotron light source. The magnets shown are electro-magnets with iron poles. (d) Transverse magnetic field components at the center (longitudinal) of the three magnets shown.

by

$$M_{\text{drift}} = \begin{pmatrix} 1 & L \\ 0 & 1 \end{pmatrix}. \tag{2.12}$$

Dipoles A dipole consists of two parallel poles as shown in Fig. 2.2a. Due to mid plane symmetry only the field component B_y differs from zero. A dipole deflects the particles according to their energy. It is therefore used for deflecting the reference orbit and for the generation of dispersion. The field is given by $\vec{B} = (0, B_y, 0)$, i.e. it is constant inside the dipole. The bending radius ρ_0 is given by equation 2.2, the total deflection angle is $\theta = L/\rho_0$.

A dipole basically acts like a drift space on a particle with a bent reference trajectory. Furthermore electrons with a momentum deviation δ have a different bending radius and therefore leave the dipole with an additional angle and shift. The bunch is dispersed. The transfer matrix M_d for the deflection plane and M_p for the plane perpendicular to the deflection plane of a rectangular shaped dipole[d] for the vectors (x, x', δ)

[d]The position of the dipole is symmetric to the reference trajectory. The angle of the pole face to the

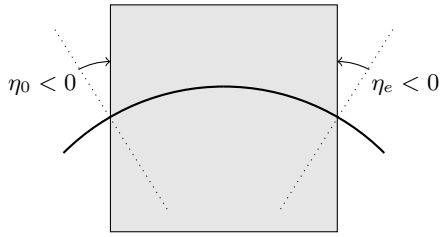

Figure 2.3.: Pole face rotation angle for the dipoles: The dotted lines are perpendicular to the particle trajectory (black line). The rotation angles η_0 and η_e are defined according to these perpendicular lines with the sign convention given in the sketch.

and (y, y') are given by

$$M^d_{\text{dip}} = \begin{pmatrix} 1 & \rho_0 \sin\theta & \rho_0(1-\cos\theta) \\ 0 & 1 & 2\tan(\theta/2) \\ 0 & 0 & 1 \end{pmatrix} \quad \text{and} \quad M^p_{\text{dip}} = \begin{pmatrix} 1 & \rho_0 \sin\theta \\ 0 & 1 \end{pmatrix}. \tag{2.13}$$

If the entrance or exit pole face is rotated by the angle η_0 or η_e with respect to the reference trajectory, like in our setup where the beam enters or leaves the dipole with rectangular poles perpendicular to the pole face, the path length of the trajectories inside the magnet and therefore the deflection changes with the transverse position. The angles η_0 and η_e are the angles between the pole phase and the transverse plane perpendicular to the reference trajectory at the entrance position of the reference particle in the dipole. The sign convention is shown in Fig. 2.3.

For the calculation of the transfer matrix the angle η_0 to the entrance and η_e to the exit pole face have be considered. The total transfer matrix of a dipole is given by $M_{\text{dip,total}} = M_{\eta_e} \cdot M_{\text{dip}} \cdot M_{\eta_0}$ with the dipole matrix from equation 2.13 and the index d for the deflection plane p for the plane perpendicular to it.

The focusing matrix for the deflection plane is given by

$$M^d_{\eta_{0/e}} = \begin{pmatrix} 1 & 0 \\ \frac{\tan\eta_{0/e}}{\rho_0} & 1 \end{pmatrix}. \tag{2.14}$$

Perpendicular to the deflection plane the fringe fields of the dipoles have a focusing effect on the beam. Assuming a linear drop of the fringe field the according matrix is

trajectory is $\eta_0 = \eta_e = -\theta/2$ at the entrance and exit of the dipole with the deflection angle θ.

given by

$$M^{p}_{\eta_{0/e}} = \begin{pmatrix} 1 & 0 \\ \frac{\tan\eta_{0/e}+\delta_{f_{0/e}}/3}{\rho_0} & 1 \end{pmatrix} \tag{2.15}$$

with the parameter $\delta_{f_{0/e}} = \frac{G}{\rho_0 \cos^2 \eta_{0/e}}$ and the total gap height $2G$.

Quadrupoles A quadrupole consists of four poles as shown in Fig. 2.2b. The field of a quadrupole is characterized by the linear-order multipole strength k. The field components, which are plotted in Fig. 2.2d for the horizontal plane, depend linearly on the transverse coordinates:

$$\frac{e}{cp}B_x = ky \quad \text{and} \quad \frac{e}{cp}B_y = kx \tag{2.16}$$

k is defined as

$$k = \frac{e}{cp}g = \frac{e}{cp}\frac{\partial B_y}{\partial x} = \frac{e}{\beta_e E_0}g \tag{2.17}$$

with the energy E_0 of the reference particle. The gradient g of the quadrupole is constant. The field of the quadrupole increases linearly with the distance to the center. The further the distance of the electron to the center is, the stronger is the deflection. In one plane the force is directed towards the center and the quadrupole focuses the beam. In the other plane the force points away from the center and the beam is defocused. The matrices for a quadrupole of length L are for the focusing plane

$$M_{qf} = \begin{pmatrix} \cos(\sqrt{k}L) & \frac{1}{\sqrt{k}}\sin(\sqrt{k}L) \\ -\sqrt{k}\sin(\sqrt{k}L) & \cos(\sqrt{k}L) \end{pmatrix} \tag{2.18}$$

and for a defocusing quadrupole

$$M_{qd} = \begin{pmatrix} \cosh(\sqrt{|k|}L) & \frac{1}{\sqrt{|k|}}\sinh(\sqrt{|k|}L) \\ \sqrt{|k|}\sinh(\sqrt{|k|}L) & \cosh(\sqrt{|k|}L) \end{pmatrix}. \tag{2.19}$$

According to the convention a positive k-value corresponds to a quadrupole focusing in x. To focus the beam in both planes a combination of quadrupoles, e.g. a doublet or triplet, has to be used. The focusing depends on the energy of the electron. For particles with an energy deviation the focal length changes and the system has a chromatic error, the so-called chromatic aberration.

If the focal length f of the quadrupole is significantly larger than the length L of the

quadrupole, the thin lens approximation can be applied with $f^{-1} = kL$. The length L goes to zero and the trigonometric terms in the matrix vanish. The transfer matrix can be simplified for this case to

$$M_{\text{q,thin}} = \begin{pmatrix} 1 & 0 \\ -\frac{1}{f} & 1 \end{pmatrix}. \tag{2.20}$$

In this thesis I neglect the shape of the fringe fields and calculate with a rectangular field model as the fringe fields drop fast and therefore their influence is small.

Sextupoles For the chromatic correction of the quadrupoles magnetic multipole fields of higher order are required. The next higher order multipole is the sextupole, which consists of six poles as shown in Fig. 2.2c. The fields of the sextupoles are characterized by the sextupole strength m with

$$\frac{e}{cp}B_x = mxy \quad \text{and} \quad \frac{e}{cp}B_y = \frac{1}{2}m(x^2 - y^2). \tag{2.21}$$

The sextupole strength m is defined as

$$m = \frac{e}{cp}s = \frac{e}{cp}\frac{\partial^2 B_y}{\partial x^2} \tag{2.22}$$

As the fields are non-linear, the effect of the sextupole on a particle cannot be described with linear equations. Its influence on the beam and a mathematical description thereof is given in subsection 2.1.5 together with a method for implementing a sextupole correction to a beam line.

Solenoids A further magnet to mention here is the solenoid. It is not part of the series of transverse multipoles as it does not consist of a number of alternating polarized poles. It consists of a longitudinal coil placed in rotation symmetry to the beam axis. Inside the coil there is only a longitudinal field. Due to Maxwell's equation div $\vec{B} = 0$ there are radial fringe fields, which accelerate the particles in azimuthal direction. With this azimuthal velocity component the electron is focused by the longitudinal field inside the solenoid. This focusing occurs in both transverse planes in contrast to a quadrupole. In approximation of a thin lens the focal length f_{sol} is given by [Rossbach and Schmueser, 1994b]

$$\frac{1}{f_{sol}} = \int \left(\frac{eB_s}{2p}\right)^2 ds. \tag{2.23}$$

It increases with the square of the momentum p. Therefore solenoids provide only in the range of low particle energy an effective focusing or, for higher particle energies a higher field strength is required. Solenoids are often used for a collimation of the beams after the particle source of a conventional accelerator or after the source of anti-particles. In the latter case due to the high energies superconducting magnets are used.

2.1.4. Phase Space and Emittance

The equations given up to here describe the movement of single electrons in magnetic fields. In general one is interested in calculating the evolution of a certain volume in phase space along a beam transport system. A distribution which is limited e.g. by a number of apertures can be approximated with an ellipse in the two dimensional transverse phase space and can be described with the beam matrix

$$\sigma = \begin{pmatrix} \sigma_{11} & \sigma_{12} \\ \sigma_{21} & \sigma_{22} \end{pmatrix} \quad \text{and} \quad \begin{pmatrix} x & x' \end{pmatrix} \sigma^{-1} \begin{pmatrix} x \\ x' \end{pmatrix} = 1. \tag{2.24}$$

The area of the ellipse is given by $\pi \cdot \det(\sigma)$.

According to the equations of the previous subsection the beam ellipse can be calculated at different positions along the beam transport system by transforming the variables x and x' with the matrices. In fact, the beam matrix itself can be transformed with $\sigma_1 = M\sigma_0 M^T$ with a transfer matrix M.

According to Liouville's theorem the phase space density in a conservative system is conserved. The area of the beam ellipse is proportional to the determinant of the beam matrix and the determinant of M is one. As the determinant of a product of matrices is equal to the product of the determinants of the single matrices, the area of the ellipse is constant along the beam transport system.

In Fig. 2.4 the phase space ellipse for the two-dimensional transverse phase space x-x' is shown. The maximum extension in both directions and the intersections with the axes are marked in the sketch. The quantities are expressed in terms of the *Twiss parameters* β, α and γ. With the emittance and the Twiss parameters the beam size $\sigma_{x,y} = \sqrt{\varepsilon_{x,y}\beta_{x,y}}$ and the divergence $\sigma_{x',y'} = \sqrt{\varepsilon_{x,y}/\gamma_{x,y}}$ is determined. Expressing the beam matrix in terms of the Twiss parameters gives the following equation:

$$\sigma = \begin{pmatrix} \sigma_{11} & \sigma_{12} \\ \sigma_{21} & \sigma_{22} \end{pmatrix} = \varepsilon \begin{pmatrix} \beta & -\alpha \\ -\alpha & \gamma \end{pmatrix} \tag{2.25}$$

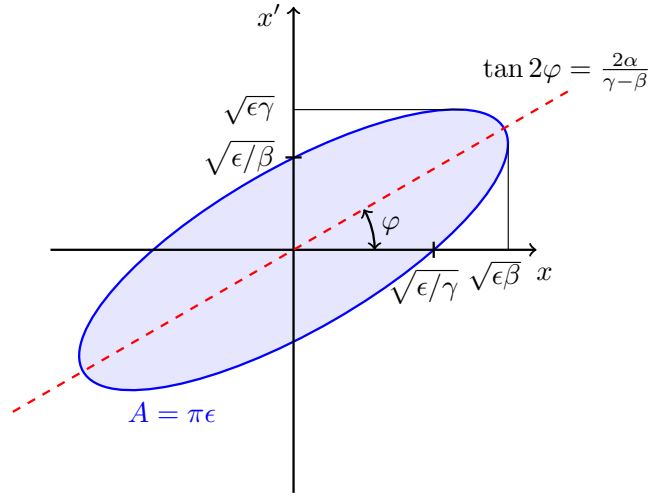

Figure 2.4.: Phase space ellipse in the two-dimensional transverse phase space x-x'. The intersection with the coordinate axes, the maximum extension along the axes and the angle of inclination of the ellipse in terms of the Twiss parameters β, α and γ and the emittance ε are given.

A direct transformation of the Twiss parameters using the matrix elements of the previously introduced transfer matrices from equation 2.10 is given by

$$\begin{pmatrix} \beta_1 \\ \alpha_1 \\ \gamma_1 \end{pmatrix} = \begin{pmatrix} C^2 & -2CS & S^2 \\ -CC' & CS' + SC' & -SS' \\ C'^2 & -2C'S' & S'^2 \end{pmatrix} \begin{pmatrix} \beta_0 \\ \alpha_0 \\ \gamma_0 \end{pmatrix}. \tag{2.26}$$

As the beam size is proportional to $\sqrt{\beta}$ at a beam waist β has a minimum. α is proportional to the derivative of β with $\alpha = -\beta'/2$, thus α is zero at a beam waist. γ depends on α and β with $\gamma = \frac{1+\alpha^2}{\beta}$.

The so-called geometric emittance in the phase space of position and propagation angle x-x' corresponds to the area of the phase space ellipse with $A = \pi\varepsilon$ and is constant for a fixed particle energy. In this thesis I consider the width of one σ for the quantities of Gaussian distribution.

For generalizing the definitions to a particle distribution the Twiss parameters and

the emittance can be determined as statistical quantities with the rms-values:

$$\varepsilon_u = \sqrt{< u^2 >< u'^2 > - < uu' >^2} \tag{2.27}$$

$$\beta_u = \frac{1}{\varepsilon_u}\left(< u^2 > - < u >^2\right) \tag{2.28}$$

$$\alpha_u = \frac{1}{\varepsilon_u}\left(< uu' > - < u >< u' >\right) \tag{2.29}$$

2.1.5. Second Order Systems and Chromatic Correction

In the previous part of this section only the linear components of the equation of motion are considered. This approximation is valid for particle beams with a negligible momentum spread δ occupying a small volume in phase space. With an increase of these quantities higher order effects have to be considered for an appropriate description of the beam dynamics.

Including second order effects, several additional terms appear in the transformation of the parameters, e.g. for the coordinate x [Carey, 1986b]

$$\begin{aligned} x =& (x|x_0)x_0 + (x|x'_0)x'_0 + (x|\delta)\delta + \\ & (x|x_0^2)x_0^2 + (x|x_0x'_0)x_0x'_0 + (x|x_0\delta)x_0\delta + (x|x'^2_0)x'^2_0 + (x|x'_0\delta)x'_0\delta + (x|\delta^2)\delta^2 + \\ & (x|x'_0y'_0)x'_0y'_0 + (x|y_0y'_0)y_0y'_0 + (x|y'^2_0)y'^2_0. \end{aligned}$$

The first line contains the familiar linear terms, the second and third line the additional second order terms[e]. A general equation for all coordinates with the initial vector $x(0) = (x_0, x'_0, y_0, y'_0, l_0, \delta)^T$ and the matrix elements $T_{ijk} = (x_i|x_j(0)x_k(0))$ is given by

$$x_i = \sum_j R_{ij}x_j(0) + \sum_{jk} T_{ijk}x_j(0)x_k(0). \tag{2.30}$$

The elements of T are divided in two groups: chromatic aberrations, which depend on the momentum deviation δ and are caused e.g. by a change of the focusing strength with the particle momentum, and geometrical aberrations involving the position and propagation angle of the particle. A derivation and a list of the single matrix elements is given e.g. in [Carey, 1986b].

The nonlinearities influence the shape of the phase space distribution, cause a transverse displacement of the particles or a shift of the focus position in longitudinal direc-

[e] Again, mid plane symmetry is assumed and only terms which do not vanish under this assumption are listed.

tion. Therefore one tries to compensate them. In this thesis I focus on the compensation of the chromatic aberration as the chromatic aberration caused by the quadrupoles dominates the second order effects for high energy particles beams, while the aberrations caused by dipoles are small.

For the chromatic correction sextupole magnets are used. The linear transfer matrix of these magnets equals a drift space, but the nonlinear component causes a geometrical aberration. For the compensation of the chromatic aberration the sextupole has to be placed in a region with dispersion. The dispersion allows a coupling of the geometrical aberration of the sextupole to the chromatic aberration of the beam transport system and therefore a correction of the latter [Carey, 1986b]. Unfortunately this correction in one transverse plane leads to a deterioration of the geometric aberration in the second. Hence a second sextupole of the same strength but opposite polarization should be placed at a position with similar beam functions where the dispersion is zero. With this the geometric aberration introduced by the first sextupole can be compensated. Often it is more effective to not compensate the chromatic aberration completely, but to choose a lower strength of the sextupoles to avoid generating additional geometric aberrations by the sextupoles.

2.2. Synchrotron Radiation Generated in Undulators

The electromagnetic radiation that is emitted by a charge moving on an arc with relativistic velocity is called *synchrotron radiation*. It is named after the synchrotron, a circular particle accelerator with a constant particle orbit[f] , in which this radiation was observed for the first time [Elder et al., 1947]. Synchrotrons were originally designed as successors of the betatron and cyclotron for high energy particle physics, but soon synchrotron radiation generated in the bending magnets during the deflection of the particles was discovered as a useful radiation source for absorption and calibration measurements in the far ultraviolet [Tomboulian and Hartman, 1956]. Several textbooks and lectures cover the topic of generation and properties of synchrotron radiation, e.g. [Turner, 1998, Hofmann, 2004, Clarke, 2004, Bernhard, 2011] from which most of the derivations and equations in this section are taken.

The typical spectrum of synchrotron radiation covers a broad frequency range up to hard x-rays. The maximum photon energy, which is reached, depends on the relativistic

[f] The particle orbit is constant in contrast to e.g. a cyclotron, where the radius of the particle orbit increases with increasing particle energy during acceleration. In a synchrotron the field of the bending magnets is increased with the particle energy during acceleration to keep the orbit constant.

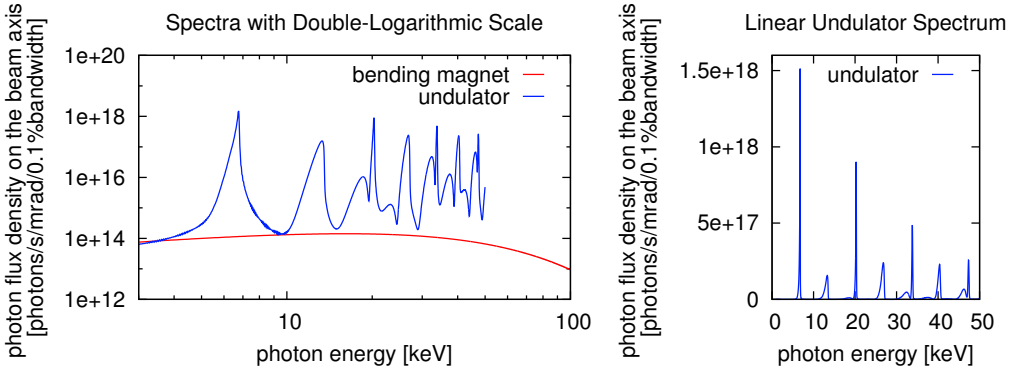

Figure 2.5.: Simulated spectrum of a bending magnet and an undulator: The parameters of the beam and the magnets correspond to the parameters of the European Synchrotron Radiation Facility (ESRF) with the in-vacuum undulator U17. (Simulated data from [Bernhard, 2011])

factor γ_e and the magnetic field of the bending magnets. An example for the spectrum emitted in a bending magnet of the European Synchrotron Radiation Facility (ESRF) is shown in Fig. 2.5. The radiation is emitted in a small cone with opening angle $1/\gamma_e$ in forward direction tangential to the particle trajectory. The time, this radiation cone passes e.g. a detector is in the of the order of some tens of picoseconds, thus the observer receives very short light pulses. Furthermore the radiation has well determined polarization properties: In the deflection plane it is linearly polarized in horizontal direction. The vertical polarization component increases with the distance to this plane and the synchrotron radiation has an elliptical polarization.

Its unique characteristics make the synchrotron radiation attractive for a large number of applications, e.g. for scattering, diffraction and spectroscopic experiments with different materials, but also for material processing, calibration and a lot more. As a consequence electron synchrotrons were built dedicated for the generation of synchrotron radiation[g]. These synchrotrons are the second generation light sources.

In third generation light sources additionally to the bending magnets insertion devices are installed in the straight sections of the ring between the bending magnets[h]. The most common insertion devices are planar wigglers and undulators, both magnetic structures consisting of a periodic sequence of alternating dipoles, which generate an alternating, periodic field along the propagation axis z and deflect the electrons many times.

[g] Electrons emit radiation at higher energies and intensities than proton due to their lower rest mass.
[h] The straight sections without magnets are called insertions.

The spectrum of the radiation emitted in a wiggler has the same shape as the spectrum of a bending magnet. As the electrons are not deflected once but N_p times, with N_p the number of poles of the magnetic field, the number of photons is also increased by a factor of N_p. In contrast to the bending magnets, where the field is determined by the deflection angle in the ring, the magnetic field in a wiggler and in turn the emitted spectrum can be varied in a certain range. A wiggler provides therefore a higher photon flux than a bending magnet and more flexibility in terms of the magnetic field.

The spectrum emitted by an undulator is different from the spectra of a bending magnet or a wiggler. In general the period length of its magnetic field is shorter than that of a wiggler and the field is weaker. That leads to constructive interference of the radiation of single electrons. These spectra of the single electrons add up to a total spectrum, which shows single peaks with a small bandwidth. The number of photons in these peaks is increased by a factor N_u^2 with N_u the number of undulator periods. An undulator provides a significantly larger number of photons for certain frequencies than a wiggler. In Fig. 2.5 the spectrum for an undulator of the ESRF with the characteristic peaks in the linear spectrum is shown.

One aims to develop compact, low-cost synchrotron radiation sources, for example by combining an undulator with a LWFA. For the design of such a setup it is necessary to adapt the conventional undulator technology to the properties of this accelerator. In this section the properties of conventional undulators and their influence on the electron bunches in linear accelerators are summarized to introduce the necessary parameters and effects for discussions in the following chapters.

2.2.1. Particle Trajectories inside the Undulator

For the description of the movement of a particle inside the undulator I am assuming an undulator consisting of N periods of length λ_u, where the *undulator period length* λ_u is the distance from one field maximum to the next. The particle is considered to have charge e and rest mass m_0 and to move with velocity v_e along the z-axis. Furthermore I assume that the field of the undulator deflects only in the horizontal x-z-plane and in the region of the particle motion the field does not vary along the x-axis. In the plane centered between the two undulator halves at the zero position of the vertical axis y, the mid plane of the undulator, the field is given by

$$B_y(z) = B_0 \cos k_u z \quad \text{with} \quad k_u = \frac{2\pi}{\lambda_u}. \tag{2.31}$$

The Lorentz force $\vec{F} = e\vec{v}_e \times \vec{B}$ acts on the particle. With the initial position of the particle $x = y = 0$ the relativistic equations of motion are

$$\gamma_e m_0 \ddot{x} = \gamma_e m_0 \frac{d^2x}{dt^2} = -eB_0 \cos(k_u z)\, \dot{z} \quad \text{and} \tag{2.32}$$

$$\gamma_e m_0 \ddot{z} = \gamma_e m_0 \frac{d^2z}{dt^2} = eB_0 \cos(k_u z)\, \dot{x}. \tag{2.33}$$

Equation 2.32 can be integrated directly:

$$\dot{x} = -\frac{eB_0}{\gamma_e m_0 k_u} \sin(k_u z) \tag{2.34}$$

The velocity of the particle is ultra-relativistic, i.e. the relativistic factors can be approximated with $\beta_e = \frac{v_e}{c} \approx 1$ and $\gamma_e = \sqrt{\frac{1}{1-\beta_e^2}} \gg 1$. The total velocity of the particle is constant with $\beta_e^2 c^2 = \dot{x}^2 + \dot{z}^2$. Solving for the longitudinal velocity gives

$$\dot{z} = \beta_e c \sqrt{1 - \frac{\dot{x}}{\beta_e^2 c^2}}. \tag{2.35}$$

Assuming that the deflection angle ψ of the particle trajectory is small, i.e. the transverse velocity $\dot{x}$ is small compared to the total velocity $\beta_e c$, the longitudinal velocity $\dot{z}$ is approximately $\dot{z} \approx \beta_e c$. The derivative of x with respect to z or the deflection angle ψ of the trajectory in this approximation is then given by

$$x'(z) = \psi = \frac{\mathrm{d}x(z)}{\mathrm{d}z} = \frac{\dot{x}}{\dot{z}} = -\frac{eB_0}{\beta_e c \cdot \gamma_e m_0 k_u} \sin(k_u z)\,. \tag{2.36}$$

All parameters of the coefficient of this expression, which are independent of the particle movement, are summarized in the *undulator parameter* K_u with

$$K_u = \frac{eB_0}{m_0 c k_u}. \tag{2.37}$$

The approximation of a constant motion of the particle along z with the velocity $\beta_e c$ holds for weak magnetic fields or $K_u \ll 1$. Such undulators are called *weak undulators*. The maximum deflection angle ψ_0 in such an undulator is smaller than the opening angle $1/\gamma_e$ of the synchrotron radiation cone. The undulators realized usually have a stronger magnetic field and the approximation made is not valid. In such a *strong undulator* $K_u > 1$ holds and the deflection angle is larger than the opening angle of the radiation. Equation 2.35 is still valid, but the second term under the square root cannot

be neglected in the particle motion. For the deflection angle therefore follows

$$x'(z) = \psi = \frac{K_u \sin(k_u z)}{\beta_e \gamma_e \sqrt{1 - \frac{K_u}{\beta_e^2 \gamma_e^2}}}. \tag{2.38}$$

The particle velocity in a strong undulator can be derived from these equations (see e.g. [Hofmann, 2004, Bernhard, 2011]) transforming the longitudinal coordinate back to the time t' of the system co-moving with the electron bunch[i]:

$$\dot{x}(t') = -\frac{cK_u}{\gamma_e} \sin(\Omega_u t') \tag{2.39}$$

$$\dot{z}(t') = \beta_e^* c + \frac{cK_u^2}{4\beta_e^2 \gamma_e^2} \sin(2\Omega_u t') \tag{2.40}$$

with the average longitudinal velocity

$$\beta_e^* c = \beta_e c \left(1 - \frac{K_u^2}{4\beta_e^2 \gamma_e^2}\right) < \beta_e c, \tag{2.41}$$

the oscillation frequency Ω_u and the reduced relativistic factor γ_e^*

$$\Omega_u = k_u \beta_e^* c \quad \text{and} \quad \gamma_e^* = \frac{1}{\sqrt{1 - \beta_e^{*2}}}. \tag{2.42}$$

An integration of equations 2.39 and 2.40 neglecting terms of order $\left(\frac{K_u}{\beta_e \gamma_e k_u}\right)^2$ gives the particle trajectory in the undulator:

$$\vec{R}(t') = \begin{pmatrix} \frac{K_u}{\beta_e \gamma_e k_u} \cos(\Omega_u t') \\ 0 \\ \beta_e^* c t + \frac{K_u^2}{8\beta_e^2 \gamma_e^2 k_u} \sin(2\Omega_u t') \end{pmatrix} \tag{2.43}$$

The trajectory has an oscillation in the longitudinal motion with the double frequency of the transverse oscillation. Therefore the particle performs a figure-of-eight motion in the co-moving frame of reference. As a consequence for the calculation of the radiation spectra not only the linear terms, but also terms of higher order have to be considered. In Fig. 2.6 a trajectory of an electron in an undulator is shown.

[i] The system moves with the averaged longitudinal velocity $\beta_e^* c$ given in equation 2.41.

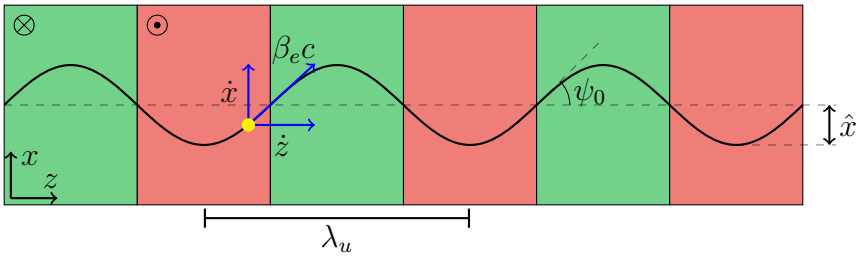

Figure 2.6.: Trajectory of an electron inside an undulator with period length λ_u: The electron has the total velocity $\beta_e c$, the transverse velocity $\dot{x}$ and the longitudinal velocity $\dot{z}$. $\hat{x}$ is the maximum excursion and ψ the maximum deflection angle of the electron. In the sketch the lower half of the undulator is displayed.

2.2.2. Undulator Radiation

The spectrum of the undulator radiation has the characteristic peaks at the fundamental frequency and at the odd higher harmonics of this frequency. Two different qualitative descriptions of the shape of the spectra are given in appendix A.1.

The radiation field of the undulator is calculated from the particle trajectory in the undulator and the Lienard-Wiechert potentials. A derivation is given the books and lecture notes, from which the equations and definitions summarized here are excerpted [Turner, 1998, Hofmann, 2004, Clarke, 2004, Bernhard, 2011].

The fundamental radiation frequency ω_1 and the corresponding wavelength at the position of an observer at the observation angle θ to the beam axis are given by

$$\omega_1 = \frac{4\pi\gamma_e^2}{\lambda_u \left(1 + K_u^2/2 + \gamma_e^2\theta^2\right)} \quad \text{and} \tag{2.44}$$

$$\lambda_1 = \frac{\lambda_u}{2\gamma_e^2}\left(1 + \frac{K_u^2}{2} + \gamma_e^2\theta^2\right). \tag{2.45}$$

The second equation is called *undulator equation*. The wavelength of the undulator radiation scales with the period length of the undulator, the undulator parameter and the particle energy. It increases with the angle to the beam axis.

The radiation bandwidth of the fundamental frequency on the beam axis scales with the number of undulator periods N_u with

$$\frac{\Delta_s\lambda_1}{\lambda_1} = \frac{1}{N_u}, \tag{2.46}$$

where $\Delta_s\lambda_1$ is the spectral width from the central frequency to the first minimum of the

spectral distribution.

The radiation field calculated from equation 2.43 is the radiation field emitted by a single particle. To determine the total radiation field emitted by a bunch of electrons, the single radiation fields are added incoherently.

2.2.3. Influence of the Fields of the Undulator on the Electron Beam

The fields of an undulator influence the beam parameters. In this section two major influences of the undulator on the electron beam in a linear system are discussed: a possible shift of the position or the propagation direction of the electron beam due to the magnetic field and the focusing effects inside the undulator.

Field Integral Minimization and Field Termination

The undulator has to be designed such that it generates no offset or deflection of the electron beam after passing the insertion device. It has, in other words, to be transparent. That is equivalent to the statement that the first and the second field integral I_1 and I_2 must vanish [Turner, 1998, Clarke, 2004]. The integrals are

$$I_1 = \int_{-\infty}^{\infty} B_y(z)dz \quad \text{and} \quad I_2 = \int_{-\infty}^{\infty}\int_{-\infty}^{z} B_y(z')dz'dz. \tag{2.47}$$

For minimizing both field integrals, the simplest and most common solution is to add two additional poles with $1/4$ and $-3/4$ of the magnetic field strength at each end and an additional pole at the center of the insertion device.

These end poles are also called matching periods.

Focusing inside the Undulator

A planar undulator as considered here consist only in the mid plane of pure dipole fields pointing in the vertical direction. Slightly above or below this plane the region of the pure dipole fields is quite small as shown in Fig. 2.7. The magnetic fields are dominated by fringe fields. These fields also act on the electrons and influence their trajectories. The field component B_y forces the electron on the usual sinusoidal path, whereas the longitudinal field component B_z between the poles leads to a focusing in the vertical plane.

To explain the focusing the trajectory of an electron that moves slightly above the mid plane, i.e. $y > 0$, is shown in Fig. 2.7. Between the poles, the horizontal transverse

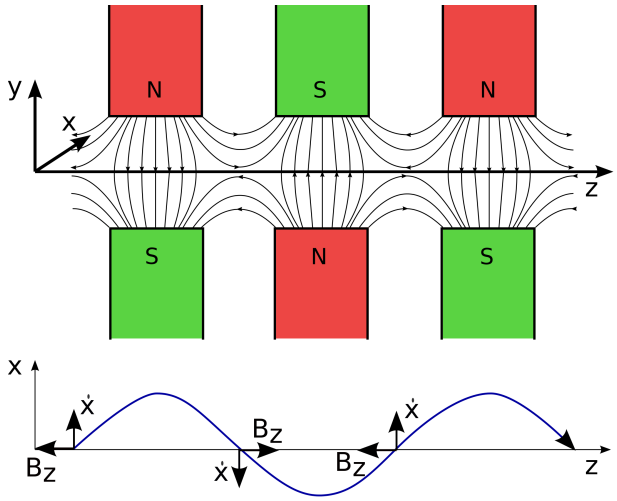

Figure 2.7.: *top:* Sketch of a cross section of an undulator with the magnetic field lines between the poles. *bottom:* Electron trajectory for $y > 0$ with the transverse velocity $\dot{x}$ and the longitudinal magnetic field B_z. The Lorentz force is acting towards the mid plane.

velocity $\dot{x}$ has its maximum, exactly at the point of the maximum longitudinal field component. The resulting force points in direction of the mid plane. For an electron moving on a trajectory with $y < 0$, the magnetic field points in the opposite direction and consequently the force acts towards the mid plane again.

From the equation of motion the focusing strength K_u can be derived (see A.2):

$$K_y(z) = -\left(\frac{e}{\gamma m_0 c}\right)^2 \int B_y dz \cdot \frac{dB_y}{dz}. \tag{2.48}$$

Is the focusing weak enough such that the focal length is long compared to the undulator period length λ_u, the focusing parameter K_u can be averaged over one undulator period with

$$\bar{K}_u = \frac{1}{\lambda_u}\int_0^{\lambda_u} K_y(z)dz = \frac{1}{\lambda_u}\left(\frac{e}{\gamma m_0 c}\right)^2 \int_0^{\lambda_u} B_y^2 dz. \tag{2.49}$$

For a pure sinusoidal field with period length λ_u and field amplitude B_0 the equation can be integrated to

$$\bar{K}_u = \left(\frac{e}{\gamma m_0 c}\right)^2 \frac{B_y^2}{2} = \frac{1}{2\rho_0^2} \tag{2.50}$$

with the bending radius ρ_0.

A planar undulator is focusing in y-direction and therefore influences the β-functions of the electron bunch, but it has no focusing effect on the bunch in x-direction.

2.2.4. State-of-the-Art in Undulator Technology

For achieving higher radiation frequencies the undulator period length has to be shortened or the electron energy has to be increased. As the latter increases the cost of the synchrotron facility ways to shorter period lengths are searched for. For short period undulators basically two different technologies are of interest for operation in synchrotrons and FELs: cryogenic permanent magnet undulators and superconducting undulators.

Cryogenic permanent magnet undulators (CPMUs) consist of permanent magnets. The performance of rare earth based magnets is increased with decreasing temperature, therefore technologies to cool the magnets to cryogenic temperatures were developed [Bahrdt and Ivanyushenkov, 2013]. To minimize the gap between the two undulator halves the magnets are in-vacuum. This technology has been well established in the last years and therefore a number of CPMUs are in operation in synchrotrons and in the FEL at SACLA.

Short period superconducting undulators (SCUs) consist of several superconducting coils forming the two undulator halves. A superconducting wire is wound on a so-called coil former or winding body, which consist of grooves and division bars separating the single coils. The current in the neighbouring coils goes in opposite directions, thus the alternating magnetic field is generated. In a planar undulator the coils are racetrack-shaped to get two planar planes facing each other. The alternating field is generated by the sum of the magnetic fields of each turn of the wire. The magnetic pole is at the position of the division bars, were the fields of the four surrounding coils add up.

It is possible to achieve higher fields with SCUs than with CPMUs and therefore a better performance in FELs or higher photon energies in synchrotrons. In addition the material damage due to radiation is smaller in SCUs and therefore smaller gaps can be realized without risking a decrease of the field quality [Emma et al., 2015]. Though, several technical challenges come with the SCUs: To achieve a field quality that is good enough for the operation in a storage ring or FEL tight mechanical tolerances have to be keep at cryogenic temperatures. A correction of the field errors such as the shimming in the CPMUs is not feasible for SCUs. Furthermore it has to be ensured that the coils stay at cryogenic temperatures despite the heating by the electron beam [Ivanyushenkov et al., 2013]. Dealing with these technical issues, the CPMUs are the technology mostly found in todays accelerators [Bahrdt and Ivanyushenkov, 2013]. However, there are promising recent achievements in the field of SCUs and their oper-

ation in synchrotrons [Ivanyushenkov et al., 2015, Casalbuoni et al., 2015].

2.3. Laser Wakefield Accelerators

In a laser wakefield accelerator (LWFA) electrons are accelerated in the fields of a plasma wave generated by a high-power laser pulse. The accelerating gradients in this plasma wave are up to four order of magnitude higher than in conventional radio-frequency cavities [Esarey et al., 2009]. The acceleration length is significantly reduced. Furthermore the bunches emitted by the LWFA are intrinsically ultra-short. That makes LWFAs interesting as compact accelerators for several applications, e.g. as drivers for compact light sources and as injectors for conventional accelerators.

However, the bunch parameters are not as stable as in conventional accelerators: The energy spread of the bunches in the range of one percent or more is some orders of magnitude higher than in conventional accelerators. The central energy also varies in this range. The divergence of the bunches in the range of some milliradian makes the shaping and transport of the bunches difficult.

In this section the acceleration process of the LWFA with its parameters and are shortly described mentioning the terms and quantities relevant for this thesis. The information summarized here is from review articles and lecture notes [Esarey et al., 2009, Malka et al., 2008, Schlenvoigt et al., 2010, Hooker, 2013, Kaluza, 2009].

2.3.1. The Acceleration Process in a LWFA

Generation of a Plasma Wave The high-power laser pulse is focused into a gas, where its leading edge generates a plasma. Propagating along the plasma the laser pulse pushes the electrons away from its propagation axis via the so-called ponderomotive force[j] as shown in Fig. 2.8. The ions which exhibit a much higher mass are almost not affected by the fast oscillating fields of the laser pulse. Their motion can be neglected. Therefore a region with positive charge is generated behind the laser pulse with a restoring force attracting the electrons. As a consequence the electrons are pulled

[j] The ponderomotive force is the net force that is generated by the strong gradient of the laser pulse. The electric field of the laser makes the electrons oscillate, but due to the gradient the restoring force close to the propagation axis of the laser on one half-period of the oscillation is stronger than in the second half-period. Therefore a net force opposite to the gradient of the laser pulse is generated, which pushes the electrons away from the propagation axis of the laser pulse.

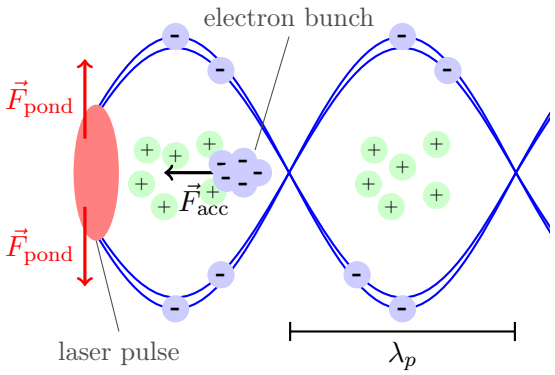

Figure 2.8.: Schematic sketch of the acceleration process of the LWFA: The electrons are pushed away from the laser propagation axis by the ponderomotive force F_{pond} and oscillate with the plasma frequency ω_p in transverse direction, while the ions can be considered as stationary. A plasma wave is generated as indicated by the blue lines. If an electron bunch is injected into this plasma wave, it is accelerated by the force F_{acc} of the strong longitudinal electrical fields of the plasma wave.

back towards the laser axis. They are forced to oscillate with the plasma frequency

$$\omega_p = \sqrt{\frac{n_e e^2}{m_e \varepsilon_0}}, \tag{2.51}$$

where n_e is the electron density of the undisturbed plasma and ε_0 the vacuum permittivity. The laser pulse moves along the plasma causing this density modulation to propagate with the velocity of the laser pulse $v_g \approx c$. A plasma wave is generated. The wavelength of this plasma wave is defined by the propagation velocity and the oscillation frequency of the electrons with $\lambda_p \approx 2\pi c/\omega_p$. For a typical electron density of $5 \times 10^{18}\,\text{cm}^{-3}$ the wavelength of the plasma wave is $\lambda_p \approx 2\pi c/\omega_p = 15\,\mu\text{m}$ with a oscillation period of $T_p = 2\pi/\omega_p = 50\,\text{fs}$.

For the optimum excitation of the plasma wave the pulse duration of the laser pulse should be equal or smaller than $T_p/2$. Most of the high power laser systems nowadays deliver such a pulse duration. During the excitation of the plasma wave the laser pulse is further compressed in its longitudinal and transverse dimensions by the interaction with the local electron density.

The separation of the positive and negative charges in the plasma wave causes strong electric fields. The longitudinal electric fields on the laser axis reach values in the range of 100 GV/m [Esarey et al., 2009]. These fields are used to accelerate electron bunches, that are injected into the plasma wave. Therefore an external generated electron bunch

can be injected into the plasma wave or the bunch is generated inside the plasma wave by so-called self-injection. In the following I limit the description to this self-injection of the bunches.

Acceleration of the Electron Bunch For the self-injecting of an electron bunch into the plasma wave the latter can be driven to a nonlinear regime by the laser pulse [Pukhov and Meyer-ter Vehn, 2002]. In this regime the electrons are completely expelled from the region directly after the laser pulse. When the plasma wave brakes, electrons from the rear side of this region are injected as a bunch and accelerated in the longitudinal field of this first period of the plasma wave as shown in Fig. 2.8.

This process depends on the nonlinear evolution of the plasma wave. Thus it is not stable. Several attempts were made to control this injection into the plasma wave and achieve more stability in the parameters of the electron bunches: Faure et al. use a second counter-propagating laser pulse which triggers the injection of the electron bunch into the plasma [Faure et al., 2006], several groups generated a density gradient or a density jump inside the plasma to trigger the electron injection by decelerating the plasma wave and facilitating injection [Bulanov et al., 1998, Geddes et al., 2008, Gonsalves et al., 2011]. With a controlled injection the acceleration length can be controlled and therefore the energy is stabilized. By limiting the injection process temporally the energy spread of the bunches might be reduced. Furthermore the plasma density and the acceleration length can be adapted such that the bunches do enter by entering regions of the plasma wave with decelerating fields, the so-called dephasing.

Dephasing is one of the limits of the acceleration in a LWFA: The electrons are moving with approximately the speed of light while the plasma wave propagates with the group velocity $v_g = c\eta$ of the laser, with the refractive index η for electro-magnetic waves with small amplitude moving in the plasma:

$$\eta = \sqrt{1 - \frac{\omega_L^2}{\omega_p^2}} \tag{2.52}$$

ω_L is the frequency of the laser pulse. So the electron bunch catches up with the plasma wave and enters fields with the wrong phase, that are directed such that they decelerate the electrons. That deteriorates the bunch profile and the momentum distribution of the electrons.

Further limiting factors are the depletion of the driving laser pulse by loosing energy to the plasma wave and the defocusing of the laser pulse shortly after the focus. The

self-focusing effects of the plasma wave due to the density gradient and self-guiding structures such as discharge capillaries can compensate the latter partly.

2.3.2. Different Plasma Targets

For the first experimental verification of the LWFA principle gas jets were used for the generation of the plasma. Supersonic gas jets provide a steep density profile at the transition to the vacuum. To reduce the fluctuations from shot to shot and therefore stabilize bunch parameters the gas jets were replaced by a gas filled capillary [Osterhoff et al., 2008]. In this capillary a density profile inside the plasma is formed to guide the laser pulse along longer distances like in a waveguide. It was also shown that it is possible to generate the plasma in the gas by pre-ionization with a high-voltage discharge[k], improve the guiding of the laser pulse and increase the acceleration length further [Leemans et al., 2006]. Today also gas cells, which reduce the fluctuations from shot to shot with a static density profile, but do not have a preformed waveguide are used.

These capillaries or gas cells were combined with optimized gradients or jumps in the density profile of the gas [Gonsalves et al., 2011]. The acceleration length in these capillaries or gas cells is in the range of some centimeters, the gas jet in contrast has usually a length of some millimeters. The energies achieved with capillaries or gas cells are in the range of some 100 MeV. The highest energies reported were 2 GeV accelerated in a gas cell of 7 cm length [Wang et al., 2013] and 1 GeV in a capillary of 3.3 cm length [Leemans et al., 2006]. Both groups worked with an electrical discharge.

2.3.3. Challenges of the Technique

The stability of the beam parameters currently achieved with LWFAs is far below the standard of conventional accelerators. The divergence and the propagation angle of the bunches fluctuate in the order of 1 mrad and the central energy spread in the range of some percent.

An improved design of the plasma target with a controlled injection and acceleration length can stabilize the energy and the energy bandwidth from bunch to bunch. For increasing the electron energy to the range of 10 GeV and more the acceleration length has to be extended. The pulse energy of the laser pulses has to be high enough to drive the plasma wave over long distances and a density profile in the plasma target has to

[k] The gas in the capillary is pre-ionized by a laser pulse and high-voltage discharge, such that a plasma channel is generated to guide the main laser pulse along the capillary.

be generated appropriate for preventing the dephasing of the plasma wave and the electron bunch. Alternatively the acceleration has to be divided in several stages.

Another big issue is the limited repetition rate of the bunches in LWFAs, which is usually in the range of 1 Hz. The repetition rates in conventional accelerators are at least four orders of magnitude higher. One of the factors limiting the repetition rate in LWFAs are the high power laser systems. New laser technologies based on fiber lasers and non-linear amplification processes as the optical parametric chirped pulse amplification (OPCPA) might deliver ultra-short high-power laser pulses at repetition rates of some kilohertz in future.

3. Conceptual Design of a Compact, LWFA-driven Undulator Radiation Source

LWFAs are compact accelerators that deliver ultra-short bunches. Accelerating gradients up to several 100 GV/m are obtained [Esarey et al., 2009], three to four orders of magnitude higher than in conventional accelerators. With an acceleration length in the range of a few millimeters to some centimeters electron energies up to 2 GeV are reached [Wang et al., 2013]. Combining this compact accelerator with a short period undulator gives a promising candidate for a compact light source in the far ultraviolet or the x-ray regime [Schlenvoigt et al., 2008, Fuchs et al., 2009] or even a free electron laser (FEL) [Grüner et al., 2007, Schroeder et al., 2006].

However, a major drawback is the large relative energy spread of the bunches of the LWFA. This energy spread deteriorates the monochromaticity of the undulator radiation and, as a consequence, reduces the photon flux at the central frequency. To overcome this problem the concept of transverse gradient undulators (TGUs) was proposed [Fuchert et al., 2012]: The electron bunch is dispersed in the deflection plane x of the undulator and matched to the magnetic flux density amplitude B_y of the TGU such that all electrons of different energies emit radiation with the same wavelength. This concept is intended to be demonstrated in a cooperation of the KIT with the Friedrich Schiller University of Jena.

The experimental setup is installed at the LWFA in Jena at the JETI-40 laser system. For the operation of an undulator with the bunches of this LWFA small bunch diameters in transverse direction and stable parameters from bunch to bunch are required. With the choice of the gas target and the adjustment of the target and laser pulse parameters these bunch parameters can be optimized.

The parameters of the TGU have to be adapted to the bunch parameters of the LWFA in Jena. For the design optimization studies of the beam dynamics and the trajectories in the TGU, but also the simulation of the radiation fields are necessary.

An essential part for the realization of the experimental setup is the beam transport system from the LWFA to the TGU, which is discussed in detail in the following chapters of this thesis. It is necessary to design the system such that it collimates the bunches from the LWFA and matches the beam parameters required by the TGU. Again, the energy spread of the bunches but also the large divergence of the source require a layout of the transport system and a magnet design of the focusing magnets that differs from conventional accelerators. Moreover limitations imposed e.g. by the available space in the laboratory have to be considered. Detailed simulations and design considerations for the beam transport system are described in chapter 5.

The operation of the LWFA and studies on the improvement of the parameters of the electron bunches generated with it are a focus of the research group in Jena. The TGU is modeled, designed, manufactured and tested at the KIT [Afonso Rodriguez et al., 2014].

In this chapter the conceptual design of the experiment is presented. First the working principle of the TGU is explained, then the parameters of the different components of the setup are summarized.

3.1. Working Principle of a Transverse Gradient Undulator

The fundamental wavelength emitted on axis by a conventional planar undulator is given by the undulator equation 2.45 for an observation angle $\theta = 0$ with

$$\lambda_1 = \frac{\lambda_u}{2\gamma_e^2}\left(1 + \frac{K_u^2}{2}\right) \quad \text{with} \quad K_u = \frac{eB_0}{m_0 c}\frac{\lambda_u}{2\pi}.$$

Generating radiation with LWF-accelerated bunches in such a planar undulator leads to a broadening of the spectrum due to the relative energy spread σ_δ of the electrons, which is in the order of some percent. In a TGU, in contrast, the magnetic flux density amplitude B_y and the relativistic factor γ_e of the dispersed electron bunch in the x-z-plane are functions of x. That leads to a modified undulator equation

$$\lambda_1 = \frac{\lambda_u}{2\gamma_e^2(x)}\left(1 + \frac{K_u(x)^2}{2}\right) \quad \text{with} \quad K_u(x) = \frac{eB_0(x)}{m_0 c}\frac{\lambda_u}{2\pi}. \tag{3.1}$$

The x-dependent flux density amplitude and dispersion of the electron bunch are matched such that the emitted wavelength λ_1 is constant despite the energy spread of the electron bunches for a certain energy range. That means that the electrons of different energies oscillate with the same amplitude and frequency inside the TGU.

The dispersion of the electron beam can be realized by including dipoles in the beam

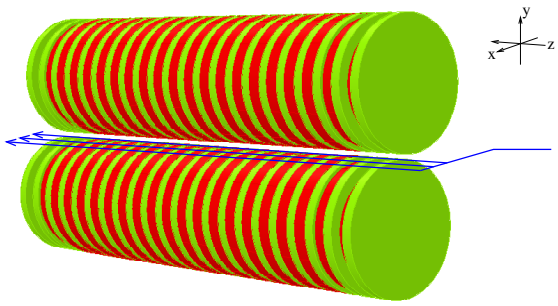

Figure 3.1.: Schematic sketch of a cylindrical TGU; the electron bunch is dispersed and passes the TGU slightly off the center at the region of the maximum gradient. (Courtesy P. Peiffer)

transport line from the LWFA to the TGU. The TGU is designed such that the gap between the two coils and therefore the magnetic flux density amplitude vary in x to achieve the required field gradient. Several design options for the TGU are discussed in [Fuchert et al., 2012]. For the parameters of the electron bunches at the LWFA in Jena a superconducting undulator consisting of two cylindrical coils is the best choice [Afonso Rodriguez et al., 2011]. A sketch of this TGU is shown in Fig. 3.1: The dispersed beam passes the TGU slightly off axis in x in the region of the maximum gradient.

The transverse field gradient causes a ponderomotive drift of the electron beam towards lower fields: The force on the electrons in the half period, in which they are deflected towards higher fields, is larger than the restoring force in the half period, in which they pass the lower field region. To ensure that each electron remains on a trajectory oscillating around the x-position the electron entered the TGU, a correction field has to be applied to compensate for this drift. This compensation can be realized with a constant force along the TGU, i.e. with a magnetic field that is constant along z and adapted to the ponderomotive drift of each electron energy in x.

A detailed description of the TGU designed for the setup in Jena and a list of its parameters is given in section 3.2.2.

3.2. Components of the Experimental Setup

As a first step towards a radiation source at a LWFA on the basis of a TGU one has to show that this theoretical principle can be realized. Therefore a proof-of-principle experiment is set up at the LWFA in Jena. The aim of this experiment is to keep the

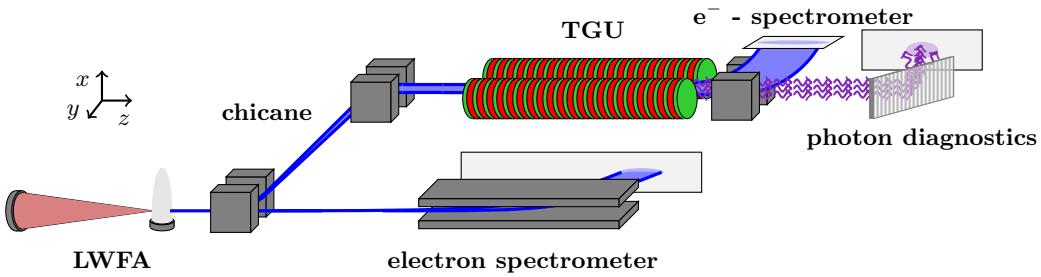

Figure 3.2.: Sketch of the setup at the LWFA in Jena: The electron bunches emitted by the LWFA are dispersed in the dogleg chicane by two dipole magnets and matched to the TGU by focusing magnets. The radiation generated in the TGU is analysed in a spectrometer. Two electron spectrometers are integrated in the setup for measuring the energy distribution of the bunches.

bandwidth $\Delta_s\lambda/\lambda_0$ of the TGU-radiation[a] close to the natural bandwidth of the fundamental wavelength of an undulator with $N_u = 100$ periods despite the energy spread of the LWFA, i.e.

$$\frac{\Delta_s\lambda}{\lambda_0} = \frac{1}{N_u} = 1\,\%. \tag{3.2}$$

The challenge of this proof-of-principle experiment is to combine all required parameters: the field gradient and the correction field of the TGU and the beam parameters of the electron bunch. On the one hand the technical limitations in the design of the TGU have to be considered and on the other hand the electron bunches with the parameters achieved at the LWFA in Jena have to be matched to the required beam parameters of the TGU.

A sketch of the setup is shown in Fig. 3.2. Leaving the LWFA, the beam can travel two alternative paths: In the dogleg chicane the electron bunches from the LWFA are dispersed and beam size and divergence are matched to the parameters required by the TGU. After passing the TGU the energetic distribution of the electrons is measured in a small electron spectrometer. The spatial and spectral distribution of the radiation is analyzed. By switching off the electromagnets in the chicane the energy distribution of the bunches can be measured in an electron spectrometer.

The design energy for the experimental setup is 120 MeV. This energy is well in the available energy range of up to 200 MeV of the LWFA setup in Jena. The energy bandwidth the TGU accepts is $\pm 10\,\%$ of the central electron energy. That covers not only the energy spread of a single electron bunch in the order of some percent but also fluctuations of the central energy from bunch to bunch.

[a] Again, the width from the maximum to the first minimum of the spectral distribution is considered.

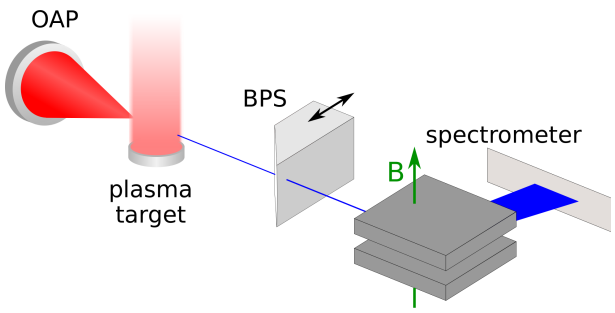

Figure 3.3.: Sketch of the setup of the LWFA: The laser pulse is focused by an off-axis parabolic mirror (OAP) to the plasma target. As diagnostics a removable beam profile screen (BPS) and an electron spectrometer are available. (Sketch according to [Schlenvoigt et al., 2008])

In the following paragraphs several components of the setup are described in detail.

3.2.1. The JETI Laser System and the Laser Wakefield Accelerator

The JETI-40 laser system is based on chirped pulse amplification. It consists of three amplifiers with Ti:sapphire-crystals. The central wavelength is 800 nm. The minimum pulse duration is 25 fs with a spectral width of 65 nm. The pulse energy at the target is about 700 mJ.

The setup of the LWFA is assembled in the target chamber for each measurement campaign. That gives the possibility to use different components for the experiments and vary single parameters of the emitted bunches. As shown in Fig. 3.3 the laser pulse is focused on a gas target with an off-axis parabola, which has a focal length of 0.65 m. The laser spot size in the focus is in the range of 10 µm to 20 µm (FWHM).

For the experiments discussed in this thesis two different gas targets were used: a supersonic gas jet and a gas cell. The gas jet has a diameter of 2.4 mm. The opening time of the valve that controls the gas flow is synchronized with the arrival time of the laser pulse. At the time the laser pulse arrives the steady flow of the gas forms a defined density profile. The gas used is helium or nitrogen or a mixture of both. The gas cell consists of small chamber with two cylinders forming the entrance and exit. The length of the cell can be adjusted with these cylinders. The working principle of the gas cell is similar to the gas jet: A valve controls the gas flow. At the time the laser pulse arrives there is a steady gas density profile inside the gas cell.

For the diagnostics of the electron bunch a beam profile (BPS) screen for measuring the transverse bunch profile and an electron spectrometer for measuring the energy

distribution of the bunch are used. The scintillating screen of the BPS has an angle of 45° to the beam axis. An image of the backside of the screen is captured with a 14-bit CCD camera perpendicular to the beam axis and at an angle of 45° to the scintillation screen. The image is therefore not distorted and the camera is not placed on the beam axis. Due to the inclination of the screen only a certain region around the center of the screen is imaged sharply. The extension of the region depends on the depth of sharpness of the imaging objective of the camera. With a smaller aperture the sharp region is larger, but the brightness of the image is reduced. In general the aperture is adapted to the bunch charge and the resulting brightness of the scintillation. The laser pulse is screened by a layer of aluminium foil directly attached to the screen. The scattering of the electrons in the aluminium has a negligible influence on the beam profile [Letzelter, 2015]. The resolution of the beam profile screen is limited by the pixel size of the camera and depends on the distance from the camera to the screen. The according values are given in later chapters with the description of the experimental setup.

The electron spectrometer consists of a permanent dipole magnet with a field of 0.7 T and a total length of 0.5 m, which is installed in a vacuum tube. The entrance aperture is an adjustable slit with a maximum aperture of 10 mm $\times$ 20 mm. Electron energies in the range of some MeV to 1 GeV are deflected to a scintillating screen, which is attached to the 1 mm thick outer wall of the aluminium vacuum chamber. An image of the screen is captured to analyze the energy distribution of the electrons. Due to the rectangular shape of the magnet the electrons of each energy are geometrically focused.

The resolution of the spectrometer depends on the electron energy. It is limited by the resolution of the CCD-camera, the acceptance angle of the spectrometer adjusted by the entrance slit and by the scattering of the bunches in the aluminium, which cannot be neglected in this case [Letzelter, 2015]. The influence of the resolution on the measurement results are discussed in the according chapter.

3.2.2. The Transverse Gradient Undulator

The TGU was designed by V. Afonso Rodriguez [Afonso Rodriguez, 2015]. It consists of two cylindrical superconducting coils. The coil former is made of copper. Therefore the TGU is completely iron-free. The design was optimized to achieve radiation frequencies as high as possible. Thus the period length was chosen as short as possible and the field on axis was maximized while keeping the gap large enough for the electron bunches to pass. All parameters and considerations for the design optimization can be found in [Afonso Rodriguez et al., 2013, Afonso Rodriguez et al., 2011]. A

Design Parameters of the TGU	
period length λ_u	10.5 mm
number of full periods N_u	100
pol radius r	30 mm
gap width on symmetry axis	1.1 mm
gap width at $x(120\,\mathrm{MeV})$	2.4 mm
flux density amp. $\tilde{B}_0$ at $x(120\,\mathrm{MeV})$	1.1 T
undulator parameter K_u at $x(120\,\mathrm{MeV})$	1.1
radiation wavelength λ_0	150 nm

Table 3.1.: Design parameters of the TGU optimized for an electron energy E_0 of 120 MeV with $\pm 10\,\%$ energy spread. A more detailed list of the design parameters is available in [Afonso Rodriguez et al., 2013].

report on the current status of the construction and measurements are published in [Afonso Rodriguez et al., 2014]. The parameters of the TGU which are relevant for the design and operation of the beam transport system are listed in Tab. 3.1.

In Fig. 3.4a a cross section of the TGU with the position of trajectories of different electron energies is shown. The higher the energy, the closer the trajectory is to the vertical symmetry plane of the TGU, which is the zero position of the transverse coordinate x. Figure 3.4b shows the position of the trajectories for different electron energies with the optimized magnetic flux density amplitude $\tilde{B}_y(x)$ and the resulting wavelength $\lambda(x)$ of the undulator radiation. With the optimized parameters the bandwidth of the radiation emitted by single electrons on the reference trajectory for each electron energy is $(\lambda_{max} - \lambda_{min})/\lambda_0 = 0.5\,\%$. The maximum difference of the emitted wavelengths is therefore smaller than the natural bandwidth $1/N_u = 1\,\%$ for a monoenergetic beamlet in an undulator with 100 periods. Simulations of the radiation of single electrons passing the field of a magnetic model of the TGU show, that the bandwidth of the emitted radiation can be kept in the required range [Braun, 2013].

The strength of the correction field B_y^{corr}, which prevents the drift of the electrons mentioned in the previous section, is plotted in Fig. 3.4b. This constant dipole-sextupole field is three orders of magnitude weaker than the field of the TGU. Therefore it can usually be neglected in the calculations of the beam dynamics inside the TGU. Instead it is assumed that the electrons keep oscillating around a constant x position along the TGU despite the transverse field gradient.

The coils of the TGU are wound with NbTi-superconductor, thus the TGU has to be operated at liquid helium temperature. The two coils are fixed in a support structure also made of copper, which keeps them in position and compensates the magnetic

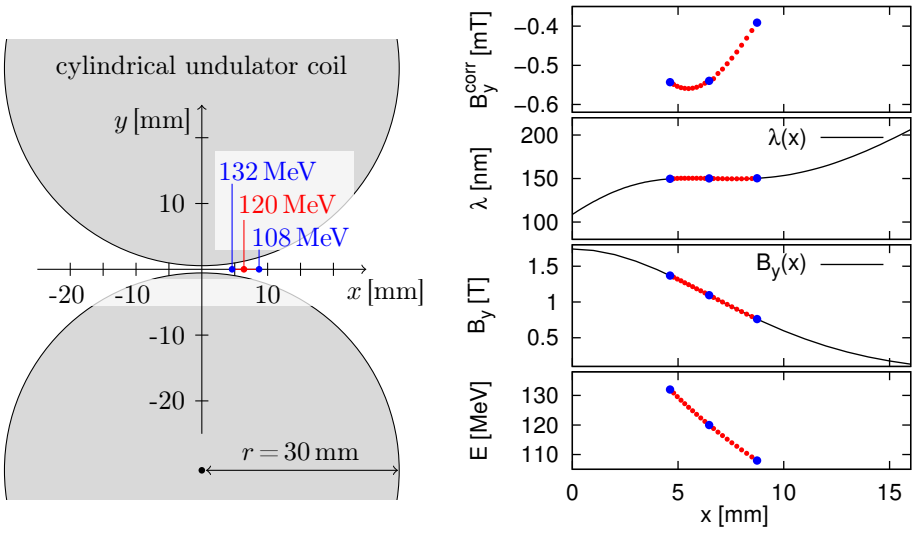

(a) Cross Section of TGU

(b) Fields and Emitted Wavelength

Figure 3.4.: (a) Cross section of the TGU with the positions of the reference trajectories of the central energy 120 MeV and the minimum and maximum energies 108 MeV and 132 MeV; (b) energy distribution $E(x)$ in the TGU, magnetic flux density amplitude $\tilde{B}_y(x)$, emitted wavelength $\lambda(x)$ determined using the undulator equation and the correction field B_y^{corr}. The blue dots are the minimum, central and maximum electron energy. The data is taken from [Afonso Rodriguez et al., 2011].

forces during operation. A picture of a 40-period TGU in the support structure is shown in Fig. 3.5a. The TGU with the support structure is mounted in a cryostat on top of a heat exchanger, which is cooled by liquid helium. A cross section of the cryostat with the TGU is shown in Fig. 3.5b. The cryostat[b] features three thermal shields, one at 4 K (dark blue in Fig. 3.5b), one at 20 K (light blue) and one at 70 K (light green). The total length of the cryostat is 1.67 m. The TGU is mounted at the center. The distance from the entrance of the cryostat to the center of the TGU is 0.885 m. There is no beam pipe foreseen to keep the magnetic gap small. The bunches of the LWFA pass the TGU only once and they have a small bunch charge. Thus the lack of a beam pipe does not cause effects on the beam due to the geometry of the TGU or the moderate vacuum in the cryostat, which deteriorate the beam profile significantly.

[b]The cryostat is designed and built by CryoVac GmbH & Co. KG [CryoVac, 2014].

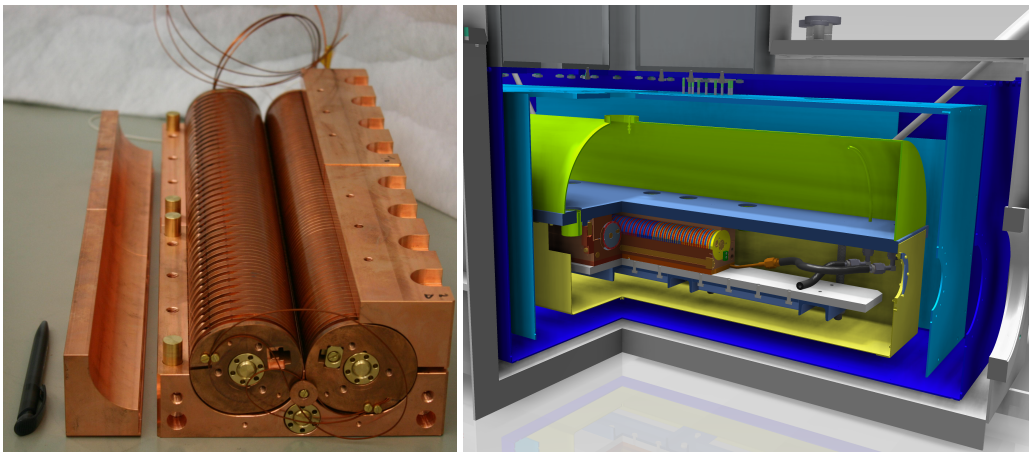

(a) Undulator in Support Structure (b) Cross Section of the Cryostat

Figure 3.5.: (a) TGU with 40 periods in support structure (courtesy V. Afonso Rodriguez); (b) cross section of cryostat with a 40-period TGU and its support structure (courtesy S. Schott and CryoVac).

3.2.3. Elements of the Beam Transport System

The beam transport system connects the LWFA with the TGU. It must be capable to collect the bunches emitted by the LWFA, transport them and match the parameters required for the operation of the TGU. Especially the dispersion, which determines the position an electron of a certain energy enters the TGU, and the size and convergence of the beam have to be adapted to the fields of the TGU.

The beam transport system is designed as a dogleg chicane with two oppositely poled dipoles to generate the dispersion and a number of focusing magnets to shape the beam and ensure a proper transport.

One important requirement is the compact design of the transport system because the whole concept aims at a laboratory scale radiation source. In the laboratory in Jena a total length of 5.6 m is available for the beam transport system, the TGU with its cryostat and the diagnostics for the undulator radiation. The beam optics therefore require compact, strong magnets and the total number of magnets has to be kept small. Long drift spaces between the magnets have to be avoided.

In chapter 4 and chapter 5 the general layout of the magnetic lattice and simulations of the beam dynamics along the TGU are presented. These calculations are important parts of my research and are described in detail in those chapters. In this section the parameters of the magnets designed for the beam transport are summarized.

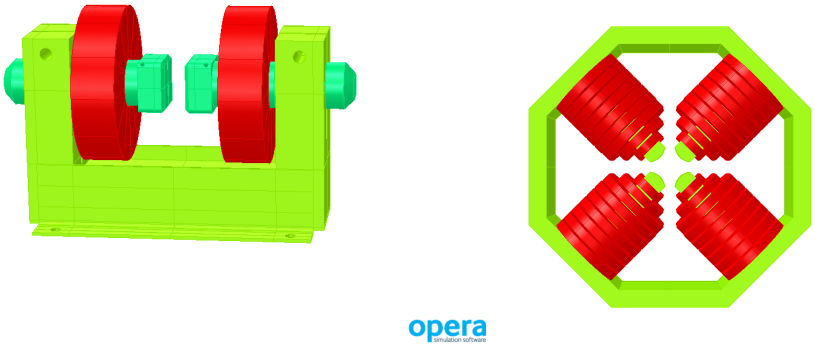

(a) Model of the Dipole (b) Model of the Quadrupole

Figure 3.6.: (a) Model of the dipole of GMW [GMW, 2013], (b) model of the quadrupole type I both generated with OPERA [OPERA, 2014] (courtesies W. Werner).

Magnets for the Beam Transport To fulfill the design requirements at electron energies of 120 MeV it was decided to use in-vacuum electromagnets. As one consequence there is no beam pipe necessary and the size of the magnetic gap can be decreased leading to stronger magnetic fields. Furthermore the setup is more flexible if the magnets can be moved in the vacuum chamber e.g. for alignment or to test different magnet configurations without taking care of a beam pipe.

For the setup three different magnet types are necessary: dipoles for deflection and the generation of the required dispersion, quadrupoles to shape the beam parameters of each monoenergetic beamlet and to focus the beam and sextupoles for a first order chromatic correction, which is necessary for beams with a large energy spread to compensate the chromatic aberration of the quadrupoles.

The dipoles are commercially available iron-dominated electromagnets[c]. The poles have a quadratic shape with a length of 50 mm. The maximum field B_y is 460 mT. As these magnets are not designed for in-vacuum operation, they are operated in an air chamber placed inside a vacuum housing. In Fig. 3.6a a model of the dipole is shown.

The quadrupoles and sextupoles are in-house designed and built electromagnets [Bernhard et al., 2015]. Their coils are water-cooled and they are designed such that they can be operated in vacuum.

There are two different types of quadrupoles implemented: Quadrupole type I with a coil design optimized for the quadrupole geometry and quadrupole type II with a slightly weaker field and with coils designed for the sextupole[d]. That was necessary

[c] GMW electromagnet model 4370

[d] Both quadrupole types have a modular design, where single parts as yokes or coils can be replaced for

because for the first setup no sextupoles but instead a larger number of quadrupoles was needed. The yoke length of the quadrupoles and sextupoles is 80 mm, the maximum gradient achieved for quadrupole type I is 35 T/m, for quadrupole type II 29 T/m and the maximum strength for the sextupole is 3500 T/m^2. A model of the quadrupole type I is shown in Fig. 3.6b.

For the operation of the magnets standard power supplies are used.[e] The power supplies are controlled remotely with a system based on EPICS [Werner, 2014]. For measuring the temperature of the magnet coils a semiconductor sensor is attached to one coil of each magnet. The temperature is logged and displayed by the control system. To prevent overheating of the coils during operation a soft and a hard temperature limit are implemented in the control system. The soft limit is part of the control software and sets the current to zero for all magnets if the temperature of one magnet exceeds 70 °C. The hard limit is part of the electronic hardware and switches off the power supplies if the temperature of any magnet exceeds 90 °C. Both limits are well below the temperature limit for the copper wire given by the supplier.

First field measurements at different currents show that the remanent field of the dipoles and quadrupoles is negligible. Nevertheless a cycling routine is implemented in the control system, which is applied after switching off or reversing the polarity of the magnets.

a good adaption to the experimental conditions.
[e] TDK Lambda Z+400 60-7

4. Start and End Parameters for the Design of the Beam Transport System

For the design of the beam transport system the start parameters and the end parameters are essential. The start parameters are the parameters of the bunches emitted by the LWFA. The first part of the beam transport system is adapted to these parameters such that it captures the electron bunches and shapes them to match the end parameters. The end parameters for the beam transport system are the beam parameters at the entrance of the TGU. These parameters are chosen such that the radiation spectra emitted by the bunches in the TGU have the required central wavelength and bandwidth.

Not all source parameters of the LWFA necessary for the design of the beam transport system were measured at the LWFA in Jena. Therefore in the first part of this chapter the parameter range of currently measured values at different LWFAs is given and compared to the setup in Jena. With this an estimation of the start parameters can be made. Due to the small bunch diameters space charge effects cannot be neglected. Their influence is estimated in a simulation presented at the end of the first section.

In the second part of the chapter the end parameters required at the entrance of the TGU are determined. The beam size along the undulator should be kept small to obtain good radiation spectra. For the description of the beam size along the TGU the analytical equations for the beam dynamics in planar undulators are adapted to the of the fields in the TGU. Based on this analytical description tracking studies were performed to include the three-dimensional field effects and calculate the resulting radiation spectra.

4.1. Start Parameters

Three groups [Faure et al., 2004, Geddes et al., 2004, Mangles et al., 2004] reported in 2004 the successful generation of electron bunches with a quasi-monoenergetic peak in the energy distribution. For the first time the operation of an LWFA in this regime was demonstrated. Subsequent studies and advancements of the laser system, plasma

target properties and diagnostics led to an improvement of the bunch parameters and the measurement techniques: Electrons energies in the range of 1 GeV to 2 GeV were reported [Leemans et al., 2006, Wang et al., 2013]. It was verified that the bunch length is in the range of few micrometers [Buck et al., 2011, Lundh et al., 2011]. The transverse bunch size inside the plasma was determined [Schnell et al., 2012, Plateau et al., 2012] and the evolution of the plasma wave was observed [Sävert et al., 2015].

Some of the source parameters of the LWFA are easily accessible in the experimental setup such as the divergence and the energy distribution of the electrons in the bunches. In contrast, the source size, the emittance and the bunch length have to be determined with a more complex setup that is not easy to implement.

Not all start parameters required for the design of the beam transport system were measured at the LWFA in Jena. The electron energy, the energy spread and the divergence are parameters usually determined during the measurements at this LWFA [Kaluza, 2012]. The source size, i.e. the bunch size at the exit of the LWFA, was measured at the LWFA in Jena with a setup usually not integrated in the diagnostics. The emittance had to be estimated by comparing the parameters of the LWFA in Jena with other LWFAs, where the emittance was measured. For further analysis also the bunch charge and the bunch length in longitudinal direction are interesting.

4.1.1. Estimation of the LWFA Source Parameters

In the following paragraphs the start parameters for the beam transport system expected at the LWFA in Jena are discussed. The values measured for several parameters at this LWFA are compared to the values achieved in measurements at other LWFA setups recently published to estimate the missing parameters and to determine the parameter range that is in general available at LWFAs.

Source Size The size of the electron bunch inside the plasma can be measured by analyzing the radiation emitted in the plasma during the acceleration process, the so-called betatron radiation. To determine the source size of the betatron radiation the radiation cone is blocked with a thin wire and the resulting diffraction pattern is analyzed. From this diffraction pattern one can estimate the size of the radiation source and therefore the transverse size of the electron bunch inside the plasma.

Such an experiment was performed at the LWFA in Jena. The measured FWHM of the transverse bunch size is $1.6 \pm 0.3\,\mu m$ for bunches with an electron energy of 120 MeV and a plasma density in the range of $1.8 \times 10^{19}\,cm^{-3}$ to $2.2 \times 10^{19}\,cm^{-3}$ in a gas jet

[Schnell et al., 2012].

At the LWFA at LOASIS, Berkeley, USA, a source size around 0.1 µm was measured with a discharge capillary as target for an electron energy of 400 MeV and at a plasma density of $5 \times 10^{18}\,\mathrm{cm}^{-3}$ [Plateau et al., 2012]. Note that the measured bunch size in the discharge capillary is one order of magnitude smaller than in the gas jet. The source size in our setup is expected to be similar to the one already measured in Jena using a gas jet or slightly smaller using a gas cell.

However, in both experiments the source size is measured inside the plasma, where the bunches are confined by the electric and magnetic fields of the plasma wave. At the transition from the plasma to the vacuum the plasma density drops rapidly, the forces get weaker and the bunches can expand in the transverse direction due to space charge effects. These effects, as shown by simulations later in this section, are expected to increase the source size to an effective value slightly larger than the values measured inside the plasma.

Energy, Energy Spread and Source Divergence The design energy for the experimental setup with the TGU is 120 MeV, a value that is in the stable range of the LWFA in Jena. The measured energy distribution at different LWFAs have an energy spread of the single bunches in the range of 1 % with fluctuations of 3 % [Wiggins et al., 2010], of 2 % to 4 % (FWHM) [Schnell et al., 2012] or in the range of up to 5 % (rms) for several bunches [Plateau et al., 2012].

For the design of the beam transport system I started with a monoenergetic electron bunch. Subsequently the energy spread was increased with an adaption of the chromatic correction of the beam transport system till the energy acceptance of the transport system reaches the range of the energy spread of the LWFA-bunches. The energy spread is therefore not explicitly a design parameter. Moreover, the transport system should match the end parameters at the entrance of the TGU for an energy spread as large as possible, but at least in the range of 1 % (FWHM).

The divergence at the LWFA in Jena is usually in the range of some milliradian, for a setup with a gas cell it is in the range of 1 mrad. Published results for measurements with a gas jet report similar values: The source divergence given is in the range of 2.5 mrad to 3.0 mrad at the LWFA in Jena [Schnell et al., 2012] or 2 mrad to 4 mrad [Brunetti et al., 2010] at the ALPHA-X setup in the UK. With gas cells or capillaries a more stable and more collimated beam and therefore smaller values of the divergence of 1 mrad or below can be achieved [Plateau et al., 2012, Weingartner et al., 2012]. As start value I chose 2.5 mrad expecting to use a gas jet as target in the experiments.

Emittance The emittance at the LWFA is measured with the pepperpot method or via a quadrupole scan.

The pepperpot is a mask with holes, which is placed into the beam path and splits the electron beam into several beamlets. From the position and the extension of these beamlets measured at a screen at known distance from the pepperpot the rms geometrical emittance can be determined. The averaged normalized emittance ε_n determined by E. Brunetti et al. with this method for an electron energy of 125 MeV is 2.2 π mm mrad with a best value of 1.1 π mm mrad [Brunetti et al., 2010]. The experiment was done at the ALPHA-X beam line, UK with a gas jet as target.

In this publication the normalized emittance is determined from the measured geometrical emittance with the equation $\varepsilon_n = \gamma_e \varepsilon_{x,y}$[a]. M. Migliorati et al. show, however, that this equation is not valid for calculating the normalized emittance of the beams of a LWFA [Migliorati et al., 2013]. Instead an additional term has to be considered:

$$\varepsilon_{n_{x,y}}^2 = < \gamma_e >^2 \left(\sigma_\delta^2 \sigma_{x,y}^2 \sigma_{x',y'}^2 + \varepsilon_{x,y}^2 \right) \tag{4.1}$$

The argumentation of the derivation of this equation presented in M. Migliorati's publication is summarized in Appendix B.1.

For the calculations presented in this thesis I only consider the geometrical emittance. For an estimation of the measured geometrical emittance in the experiment performed at the LWFA of the ALPHA-X project I calculated back to the geometrical emittance using the same equation as in the publication although it is not valid here. The resulting values are 9.0 π nm rad for the averaged geometrical emittance and 4.5 π nm rad for the minimum value measured.

In a quadrupole scan the change of the beam shape with the variation of the focusing strength is analyzed to determine the emittance. The change of the focusing can be done by varying the strength of the quadrupoles or by varying the electron energy. The beam size scales with the emittance and the β-function, thus the emittance as a constant in this calculation can be determined. With this method a normalized emittance ε_n of 0.21 π mm mrad for an electron energy of 245 MeV was determined [Weingartner et al., 2012] using a capillary as target.

In a quadrupole scan again the geometrical emittance is measured. Unfortunately in the publication it is not described how the normalized emittance was determined from the measured values. Assuming the same simplified equation mentioned above would lead to a value of 0.44 π nm rad, considering also the additional term in equa-

[a] β_e is neglected here as it is approximately one.

tion the measured geometrical emittance would be slightly smaller. Compared to the value measured with the setup using a gas jet, the geometrical emittance measured with capillary is about one order of magnitude smaller.

For both measured values of the emittance there is no definition given for the fraction of the particle number that is contained in the phase space volume.[b] However, for my calculations I assume a beam waist at the exit of the LWFA, in which case the geometric emittance is the product of the source size and the source divergence. For both quantities the value of one σ of the distribution is taken. The resulting value of $\varepsilon_{x,y}$ of $10\,\pi$ nm rad is in the range of the value measured with the setup using a gas jet.

Bunch Length The bunch length cannot be measured directly. An upper limit for the length of the electron bunches emitted by the LWFA is the wavelength of the plasma wave, which is around some micrometers. Two different indirect methods were applied to determine the bunch length: The measurement with direct imaging of the fields in the plasma wave [Buck et al., 2011] and the measurement by analysing the coherent radiation emitted by the electron bunches [Lundh et al., 2011].

The first method mentioned uses time-resolved polarimetry and plasma shadowgraphy.[c] Combining these techniques snapshots of the plasma wave during the acceleration process are measured with a probe pulse of 7.7 fs pulse duration at perpendicular incidence. After a deconvolution of the measured signal a bunch duration σ_t of 2.5 fs was determined, which corresponds to a bunch length σ_z of 0.75 µm.

For the second measurement the coherent transition radiation generated in an aluminium foil is analyzed. The bunch duration σ_t determined with this method is 1.4 fs to 1.8 fs. That corresponds to a bunch length σ_z of 0.42 µm to 0.54 µm. In this case the electrons were accelerated in a gas jet and the injection of the electrons into the plasma wave was triggered by a second laser pulse.

Bunch Charge The bunch charge is not a quantity, which is required for the design of the beam transport system. However, the intensity of the undulator radiation and the influence of space charge and coherent synchrotron radiation effects increase with the number of particles in the bunch. Bunches emitted by a LWFA usually consist of a part with high energy electrons forming the bunch and a background of electrons with

[b] For example for a Gaussian distribution for a width of σ for each distribution, 2σ etc. could be considered.

[c] For the polarimetry the rotation of the polarisation of a probe laser pulse in the magnetic fields of the plasma wave due to the Faraday effect is analyzed. For the shadowgraphy the shape of the plasma wave was determined with the deflection of the probe laser pulse due to the local plasma density.

lower energy. The background electrons of lower energy are of little interest for the transport system as they will be separated from the bunch in the first magnets and have therefore a negligible influence. At the exit of the plasma, however, this background of low-energetic electrons might increase the influence of space charge effects. As a consequence the divergence and emittance of the bunch might grow. The simulations to study this effect are presented in the following subsection.

The bunches of the LWFA in Jena typically have a bunch charge around 10 pC with a background of up to 1 nC [Kaluza, 2012].

4.1.2. Influence of Space Charge Effects

Space charge is the repelling force in a bunch of charged particles caused by Coulomb interaction. Due to the relativistic motion of the electrons, its influence is small at moderate charge densities and it decreases with increasing particle energy.

The total charge of the bunches of the LWFA with some tens of pico-Coulomb is quite low, but due to the ultra-short bunch length and the small transverse bunch size the charge density in the bunches reaches large values. As a consequence space charge effects can affect the bunches along the beam transport system.

To estimate the influence of space charge effects the propagation of bunches along a drift space was simulated with ASTRA [Floettmann, 2011]. The following scenarios were chosen: single bunches of different bunch charge with and without a background of low-energetic electrons.

The two parameter sets I used as initial conditions for the simulations are listed in Tab. 4.1. The values are taken from the results of the two experiments for measuring the bunch size inside the plasma cited in the previous subsection. The central energy of 110 MeV of the first set is close to the design of the beam transport system. The simulation was also done with a second set with an energy of 420 MeV to compare the influence of space charge at higher electron energies. For the energy spread, the divergence and the bunch size a Gaussian distribution is assumed. Each bunch consists of 1×10^5 macro-particles[d]. Details on the simulation parameters used in ASTRA are summarized in appendix B.2.

In this simulation the charge of the bunch is increased in steps from 2 pC to 0.5 nC, the charge of the background is set to 1 nC. As an indication for space charge effects on a bunch usually the increase of the emittance can be considered. The electron dis-

[d] ASTRA calculates with macro-particles. Their mass, charge etc. corresponds to a certain number of single particles.

	I [Schnell et al., 2012]	II [Plateau et al., 2012]
central energy E_0	110 MeV	460 MeV
energy spread	3 % (FWHM)	2.8 % (rms)
bunch size $\sigma_{x,y}$	1.6 µm	0.1 µm
divergence σ_ϑ	2.5 mrad	1.2 mrad
bunch charge Q	varied from 2 pC to 500 pC	
bunch length σ_z	0.3 µm	

Table 4.1.: Bunch parameters used for the simulation. The values of the parameters in the upper part of the table correspond to the values given in the according publication, the bunch charge is varied and the bunch length is assumed to be 0.3 µm.

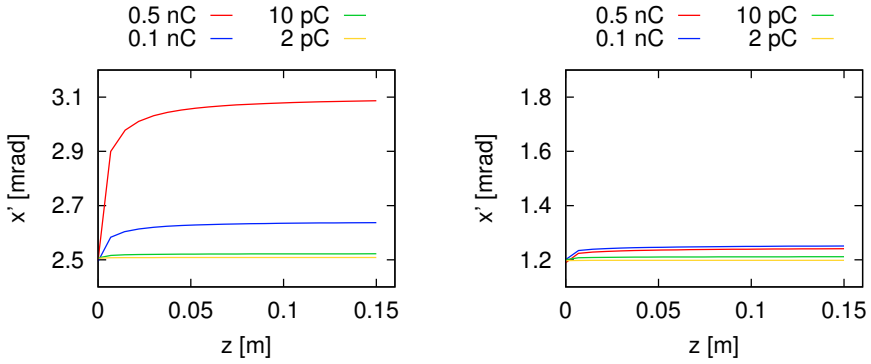

(a) Parameter Set I

(b) Parameter Set II

Figure 4.1.: Divergence bunches with the variation of the total charge 0.15 m after the source for (a) a central energy of 110 MeV and a source size of 1.6 µm and (b) central energy of 460 MeV and a source size of 0.1 µm.

tributions in the simulations are not monoenergetic. The emittance therefore increases during a propagation along a drift space according to equation 4.1. Thus the emittance cannot be used for the evaluation. Instead the evolution of the divergence is considered: Along a drift space the divergence is constant, if no space charge effects are present. In contrast, a significant influence of space charge leads to an increase of the divergence.

In Fig. 4.1 the divergence along 0.15 m distance after the source for the parameters listed in Tab. 4.1 is shown. For an electron energy of 110 MeV (Fig. 4.1a) and a bunch charge of 0.1 nC or higher the divergence increases along a small distance after the source due to space charge effects. For a bunch charge of 10 pC or smaller the change of the divergence due to space charge effects is in the range of the fluctuations of the divergence and can be neglected. For higher electron energies (Fig. 4.1b) an increase of

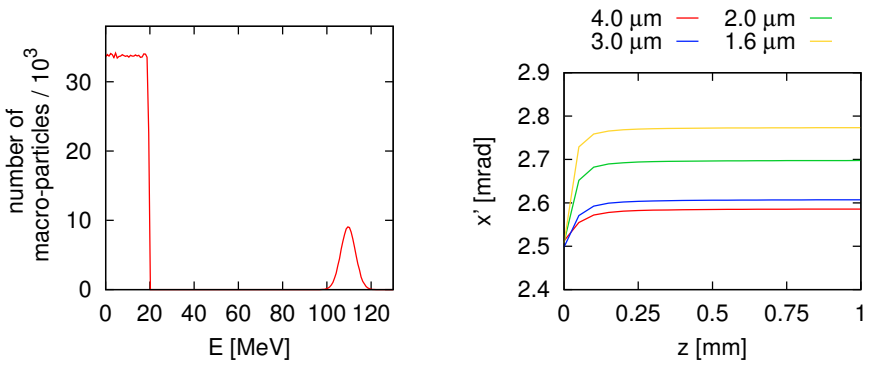

(a) Initial Energy Distribution (b) Divergence

Figure 4.2.: (a) Initial energy distribution of the macro-particles for the simulation with a charge of 10 pC of the peak and 1 nC of the background. (b) Influence of space charge effects on the divergence for different source sizes for the distribution shown in (a).

the divergence of less than 5 % is observed despite a smaller source size.

Usually a bunch emitted by the LWFA consists not only of a monoenergetic peak, but also contains a background of electrons with low kinetic energy up to a total charge of 1 nC. To include that in the simulation a background of macro-particles with the same dimension and equally distributed energies in the range of 1 MeV to 20 MeV was added to the particle distribution with an energy of 110 MeV. The initial energy distribution is shown in Fig. 4.2a. The high energy part of the bunch has a bunch charge of 10 pC. In Fig. 4.2b the divergence of this distribution for a source size varied in the range of 1.6 µm to 4.0 µm is given. For the source size of 1.6 µm the divergence is increased in the first millimeter after the source by about 11 %. For larger source sizes the influence of the space charge effects decreases.

In the experiment in Jena a bunch charge of 10 pC or less is expected at an energy of 120 MeV with a background of low-energetic electrons. The simulations show that for this case space charge effects cause an increase of the divergence in the first millimeters of propagation. After this short distance the effects are negligible along the beam transport system. To include the influence of space charge effects into the choice of the start parameters the source size is set to 4 µm. The values of the divergence is kept at 2.5 mrad as the divergence measurements mentioned before are performed outside the plasma and therefore already contain the influence of space charge.

For higher electron energies of 460 MeV the influence of space charge effects is negligible even for a bunch charge of 0.5 nC. In contrast, a stronger influence of these effects is expected even at low bunch charges for energies in the range of some 10 MeV.

4.1.3. Start Parameters Used for the Simulations

From the published parameters, the estimations of the space charge effects and the results of measurements performed at the LWFA in Jena the start parameters for the calculations were fixed.

Further assumptions were made concerning the geometry of the source: First, the same start parameters for both transverse planes were chosen. This assumption is not entirely correct as the divergence is slightly higher in the polarization plane of the laser due to an additional momentum transfer from the laser fields to the electrons [Lindau et al., 2008]. As the values for both planes are in the range of 1 mrad to 4 mrad, i.e. not well determined, it is not necessary to make a distinction of the two planes.

Second, a beam waist is assumed at the exit of the LWFA. This assumption neglects the influence of space charge. As shown in the previous subsection the influence of space charge effects is small. To take the slight increase of the emittance into account, I set the source size to 4.0 µm, a value a factor of two to three higher than in the plasma.

The divergence is measured in such a distance to the source that space charge effects can be neglected. Therefore the source divergence is set to 2.5 mrad, a value in the middle range of the measurements. With the assumption of a beam waist at the exit of the LWFA the geometrical emittance $\varepsilon_{x,y}$ is the product of the source size and the source divergence and therefore is $10\,\pi$ nm rad.

With these values and the previously made assumptions the Twiss parameters are also determined: The initial β-function is calculated from the emittance and the source size with $\beta_{x,y} = \sigma_{x,y}^2/\varepsilon_{x,y}$ and $\alpha_{x,y}$ is zero at the beam waist at the exit of the LWFA.

All start parameters are listed in Tab. 4.2.

central energy E_0	120 MeV
energy spread $\Delta E/E_0$	1 % to 4 %
source size $\sigma_{x,y}$	4.0 µm
source divergence $\sigma_{x',y'}$	2.5 mrad
geometrical emittance $\varepsilon_{x,y}$	$10\,\pi$ nm rad
bunch length σ_z	1 µm
bunch charge Q_{bunch}	10 pC
total charge Q_{total}	1 nC
$\beta_{x,y}$	1.6 mm
$\alpha_{x,y}$	0

Table 4.2.: List of initial parameters for the design of the beam transport system.

4.2. End Parameters at the TGU

The end parameters of the beam transport system at the entrance of the TGU determine the shape of the radiation spectra and their central wavelength. To find the optimum size of the beams along the TGU the influence of the undulator fields on the electron bunches have to be analyzed. Therefore the usual effects of undulators on the electron beam but also the additional effects of the transverse gradient have to be considered.

The TGU is designed such that electrons of different energies enter at a certain position x_E in x, where its field and the correction field are adapted to this electron energy such that the central wavelength is the same for all electron energies. The electrons ideally oscillate around this position x_E along the TGU. In terms of beam parameters that means that the dispersion D at the exit of the beam transport system has to be matched to the gradient of the TGU and stay constant along the TGU, i.e. the derivative D' of the dispersion has to be zero along the TGU.

For the TGU design, however, only single electrons, not electron bunches with a finite extension in both transverse planes were considered. To analyse bunches consisting of several electrons in a certain energy range the electron beam is divided into a set of monoenergetic beamlets with different central energies as shown in Fig. 4.3. The single energies cover the energy range of the beam. The propagation of each beamlet in the chicane and along the undulator can be analysed separately.

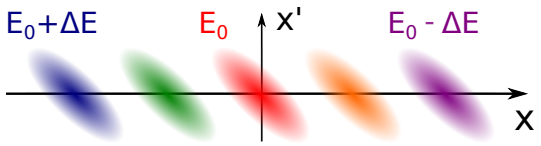

Figure 4.3.: Schematic sketch of the electron beam in the x-x' phase space split up into monoenergetic beamlets covering the energy range $E_0 \pm \Delta E$ of the beam. In a dispersive region of the beam transport system the beamlets are separated locally in x.

In the x-z-plane such a beamlet is ideally traversing only a field which corresponds to its energy. As the beamlet has a finite transversal extension σ_x, however, parts of the beamlet traverse a non ideally matched field and the radiation emitted by this part of the beam has a slightly different wavelength. To keep the bandwidth of the undulator radiation narrow, σ_x must be small such that the difference in wavelength is smaller than the natural bandwidth of the undulator radiation.

To estimate the maximum beam size $\sigma_{x,\max}$ which is allowed for keeping the monochromatic spectrum the wavelength of the radiation emitted by single electrons shifted in x was determined with the undulator equation [Afonso Rodriguez et al., 2011]. The

maximum shift in x allowed is $\pm 0.05\,\mathrm{mm}$ with respect to the optimum position x_E for keeping the emitted wavelength in the required range of $\Delta\lambda/\lambda_0 = 1\,\%$.

In the y-z-plane the usual focusing in undulators described in section 2.2.3 is the major effect influencing the beam parameters. The finite extension of each beamlet in contrast does not directly lead to an broadening of the spectrum. In the TGU the field lines are bent. For a large beam size this changes the beam shape. For example, the x-component B_x of the magnetic field increases with increasing distance to the mid plane. Coupling between the two transverse planes is induced. However, if the beam size is small along the TGU, these fields are weak and the coupling is a minor effect, which can be neglected.

The effects of the TGU-field on the electron beams are first described with simple analytical equations. With these equations several cases can be compared with little effort and without time-consuming simulations. It helps to understand the beam dynamics inside the TGU and to extend the considerations to general studies e.g. with varying field gradients and electron energies. Nevertheless the results have to be compared to the results obtained with tracking simulations and finally the radiation spectra are necessary to proof the validity of the analytic assumptions made. These studies are summarized in this section.

4.2.1. Optimum Beam Size along the TGU Derived Analytically

For an analytical description of the beams along the TGU the Twiss parameters $\alpha_{x.y}$, $\beta_{x,y}$ and $\gamma_{x,y}$ and the matrix formalism with the matrices of focusing quadrupoles are used. For both planes I search for the minimum beam size, i.e. the minimum $\beta_{x,y}$ along the TGU. Note that the actual beam size in the TGU is given by $\sigma_{x,y} = \sqrt{\varepsilon_{x,y}\beta_{x,y}}$, thus it depends also on the geometrical emittance.

For achieving the minimum $\beta_{x,y}$ along the length L of the TGU two cases can be distinguished: First, the TGU is considered as a drift space of length L with no or weak focusing fields or, second, the beam is focused along the TGU. In the first case the minimum $\beta_{x,y}$ is achieved for a focused beam with beam waist at the center of the TGU and $\beta_{\mathrm{center}} = L/2$ ([Wiedemann, 2003], p. 164). For the second case the focusing influences the beam size. For a certain beam size the focusing exactly compensates the divergence of the beam and a constant beam size along the undulator can be achieved. The smallest beam size is achieved with the constant beam size or with an initially focused beam depending on the strength of the focusing of the undulator fields.

In the following paragraphs equations for the focusing along the undulator for the

deflection plane x-z and the transverse plane y-z perpendicular to the deflection plane are derived and the optimum parameters with respect to the minimum $\beta_{x,y}$ for both transverse planes are given.

Focusing Perpendicular to the Deflection Plane In the y-z plane the focusing strength $\bar{K}_y$ averaged over one undulator period is according to equation 2.49 and 2.50

$$\bar{K}_y = \frac{1}{\lambda_u}\left(\frac{e}{\gamma_e m_0 c}\right)^2 \int_0^{\lambda_u} B_y^2(z)dz = \left(\frac{e}{\gamma_e m_0 c}\right)^2 \frac{\tilde{B}_y^2}{2}, \tag{4.2}$$

where the last equality holds for a pure sinusoidal field $B_y(z) = \tilde{B}_y \sin(k_u z)$. It is assumed that the beam has a small diameter and moves close to the mid plane, where the bending of the field lines and therefore B_x is small. The field components in x-direction are neglected. Hence, the focusing is similar to the focusing effect in a planar undulator with the difference that the focusing parameter $\bar{K}_y$ varies with the electron energy and the magnetic field B_y.

The TGU can be considered as a long focusing device with the focusing parameter $\bar{K}_y$. The transfer matrix for the TGU is the matrix of a focusing quadrupole given in equation 2.18. A constant β_y along the undulator is achieved if β_{y_0} at the entrance and $\beta_{y_{\text{end}}}$ at the exit have the same value and if there is a beam waist at the entrance, i.e. $\alpha_{y_0} = 0$. A derivation of the resulting condition

$$\beta_{y_0} = \sqrt{\frac{1}{\bar{K}_y}} \qquad \text{and} \qquad \alpha_{y_0} = 0 \tag{4.3}$$

is given in appendix A.3. In Tab. 4.3 the focusing strength and the value β_{y_c} for the constant β_y are listed for some electron energies. Note that for each energy a different β_{y_c} is given.

E / MeV	$\tilde{B}_y$ / T	$\bar{K}_y$ / m^{-2}	β_{y_c} / m
132	1.366	4.81	0.456
126	1.230	4.28	0.483
120	1.034	3.73	0.518
114	0.927	2.97	0.580
108	0.755	2.19	0.676

Table 4.3.: Parameters for the focusing in the vertical plane y-z for different electron energies E: the magnetic flux density amplitude $\tilde{B}_y$ at the ideal position x_E for each energy with the focusing parameter $\bar{K}_y$ and β_{y_c} for a constant beam size along the TGU.

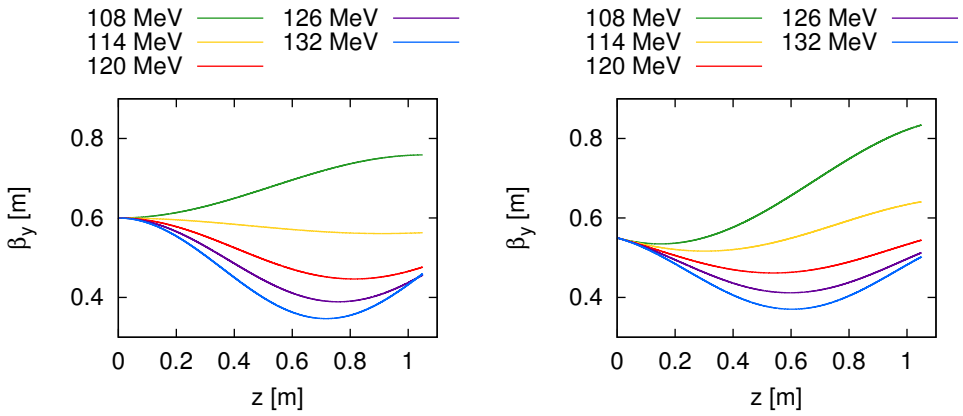

(a) Collimated Beams (b) Slightly Focused Beams

Figure 4.4.: β_y along the TGU for (a) a collimated beam with $\beta_{y_0} = 0.6\,\text{m}$ and $\alpha_0 = 0$ and (b) a slightly focused beam with $\beta_{y_0} = 0.55\,\text{m}$ and $\alpha_{y_0} = 0.05$.

For easier handling during the optimization of the beam transport system, I chose the same initial value β_{y_0} for all energies: For $\beta_{y_0} = 0.6\,\text{m}$ and $\alpha_{y_0} = 0$ a good compromise for the beam sizes of all energies is achieved. In Fig. 4.4a the course of β_y for different energies is shown for this case. For all energies above 114 MeV β_y decreases along the TGU, thus the beams are focused. For energies below 114 MeV β_y increases, but it just reaches values slightly above the value for a constant β_{y_c} for these energies.

A smaller β-function along the TGU cannot be achieved with focused beams at the entrance. Figure 4.4b shows β_y of different energies for the case of a smaller β_{y_0} at the entrance and a slightly focused beam with $\alpha_{y_0} = 0.05$. Near the entrance of the TGU β_y is smaller for all energies, but it reaches larger values at the end of the TGU than in the previous case. For stronger initial focusing this effect is even increased. Therefore the best parameters having the same values for all energies are $\beta_{y_0} = 0.6\,\text{m}$ with a collimated beam at the entrance of the TGU.

Focusing in the Deflection Plane Along x the TGU has a gradient $\frac{dB_y}{dx}$ which influences the electron bunches. The schematic in Fig. 4.5 shows the trajectories of three electrons with the same energy along one period of the TGU moving in the mid plane of the TGU: the black line is the reference trajectory, the blue line a trajectory closer to the center of the TGU, which is at $x = 0$, and the green line a trajectory with a displacement away from the center. In the first half-period shown the magnetic fields are positive and the gradient is pointing towards the center of the TGU. The trajectories of electrons closer to the center have a smaller Larmor radius than the reference trajectory,

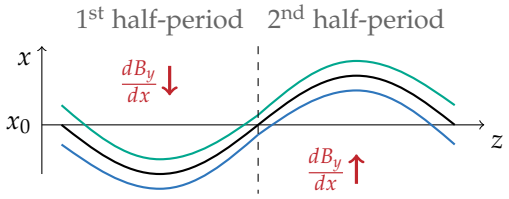

Figure 4.5.: Schematic for the focusing in the x-z-plane: For three electrons with the same energy and an offset in x the deflection in the field of the TGU is different. For electrons moving in higher fields the Larmor radius is smaller than the one of the reference trajectory (black), for the electron moving in lower fields it is larger. The beams are focused in one half-period and defocused in the other.

the trajectories of electrons moving further away from the center have a larger one. The beam is geometrically focused. In the next half-period the direction of the deflection is inverted due to the change of the sign of the magnetic field and the beam is geometrically defocused. Thus the beamlets experience an alternating focusing and defocusing along the TGU.

In the following this effect will be described analytically. The transverse field of the cylindrical TGU is given by ([Fuchert, 2009], p. 64)

$$\vec{B} = \tilde{B} \sin\left(\frac{2\pi z}{\lambda_u}\right) \left[K_1\left(\frac{2\pi\rho_u}{\lambda_u}\right)\hat{e}_{\rho_u} + K_1\left(\frac{2\pi\rho_l}{\lambda_u}\right)\hat{e}_{\rho_l}\right] \tag{4.4}$$

where $\hat{e}_{\rho_{u/l}}$ is the vector pointing radially away from the center of the upper or lower undulator coil, respectively, $\rho_{u/l}$ is the distance to the coil center and K_1 is the Bessel function. For a certain transverse position the distances to the coils ρ_u and ρ_l are constant along the TGU. That means the term in the brackets with the Bessel functions is also constant for each transverse position. Hence, the field and the gradient, the derivative of the field with respect to x, can be described with an amplitude that depends on the transverse position and the oscillation of the field. For the analytical description it is therefore sufficient to know the maximum value of the gradient for a transverse position and the period of the oscillation.

In the region of the excursion of a beamlet along the TGU the field around a reference trajectory can be approximated linearly. The position of the reference trajectory is x_E, the deviation of the particle from the reference trajectory is $\Delta x = x - x_E$. The field is given by

$$B_y(\Delta x, z) \approx \left(\tilde{B}_y(x_E) + \left.\frac{d\tilde{B}_y}{dx}\right|_{x_E} \Delta x\right) \sin\left(k_u z\right). \tag{4.5}$$

Inserting this field in the equation of motion 2.32 with the longitudinal velocity $\dot{z} \approx c$ and $x'' = \ddot{x}/c^2$ one gets

$$x'' = \frac{e}{\gamma_e m_0 c} \left(\tilde{B}_y(x_E) + \left. \frac{d\tilde{B}_y}{dx} \right|_{x_E} \Delta x \right) \sin(k_u z) \,. \tag{4.6}$$

The solution of this differential equation is the trajectory of each electron. An analytical solution is not obvious. As one is interested in the focusing of the electron beam in this case, not in the oscillation of the trajectory, the equation of motion for the reference particle is subtracted from 4.6 (see appendix A.3 for details):

$$(\Delta x)'' - \frac{e}{\gamma_e m_0 c} \left. \frac{d\tilde{B}_y}{dx} \right|_{x_E} \sin(k_u z)\, \Delta x = (\Delta x)'' + K_x(x_E) \Delta x = 0 \tag{4.7}$$

This equation is similar to Hill's equation for an electron with the displacement Δx with respect to the reference trajectory and the focusing parameter

$$K_x(x_E) = -\frac{e}{\gamma_e m_0 c} \left. \frac{d\tilde{B}_y}{dx} \right|_{x_E} \sin(k_u z) \,. \tag{4.8}$$

K_x changes its sign each half-period. Averaged over one period the focusing parameter $\bar{K}_x$ is zero and therefore the beams are not focused. To see weaker effects the focusing parameter can be averaged over a half-period or smaller intervals. I divided each undulator period in a number of subspaces and calculated the average focusing in each subspace and its influence on β_x. For 200 subspaces the shape of β_x converged. In contrast to the y-z-plane the beam envelope is oscillating due to the alternating focusing and defocusing.

For an oscillation of β_x around a constant value in x along the TGU, again, the condition $\beta_{x_0} = \beta_{x_{\text{end}}}$ and $\alpha_{x_0} = 0$ has to be fulfilled. For the transfer matrix M_u of the TGU, which is the product of the matrices of the subspaces, the condition derived in appendix A.3, equation A.16 is

$$\beta_{x_0} = \bar{\beta}_x = \sqrt{\frac{M_u^{(1,3)}}{1 - M_u^{(1,1)}}} \tag{4.9}$$

which is the constant value $\bar{\beta}_x$ around which β_x is oscillating. $M_u^{(i,j)}$ is the matrix element in line i and column j of M_u.

E / MeV	$\frac{d\tilde{B}_y}{dx}\Big\vert_{x_E}$ / Tm^{-1}	$\bar{\beta}_x$ / m
108	-137	2.23
114	-149	2.16
120	-152	2.23
126	-149	2.39
132	-140	2.66

Table 4.4.: Field gradient $d\tilde{B}_y/dx\big\vert_{x_E}$ at the position of the reference trajectory for the energy E and the value $\bar{\beta}_x$ the β-function is oscillation around.

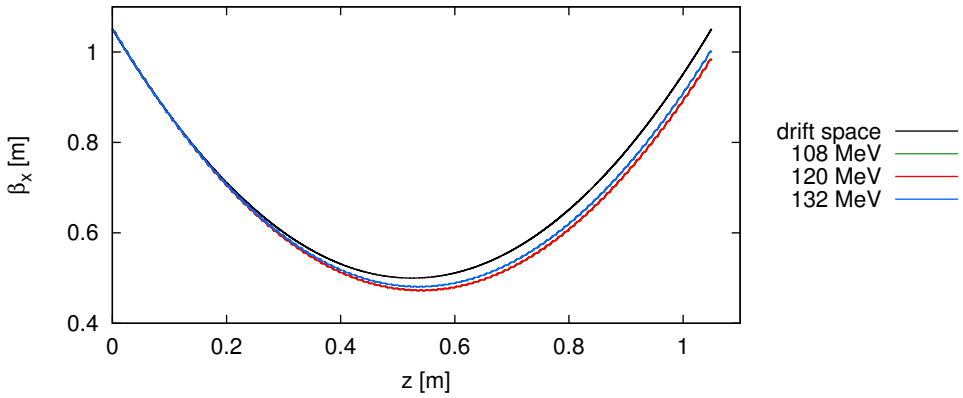

Figure 4.6.: β_x along the TGU for focused beams with a beam waist at the center of the TGU compared to β_x of a drift space.

The values for several energies are listed in Tab. 4.4. Again for each energy a different initial value is required. As the total focusing is much weaker than in y-direction the constant β_x is quite large. For higher gradients the focusing strength would increase and the values for a constant β_x would be smaller.

The maximum beam size allowed in the x-z plane is $\sigma_x = 0.05\,\text{mm}$ according to the estimations referred to at the beginning of the section. For $\beta_x = 2.0\,\text{m}$ this value is reached for a geometrical emittance of $1.25 \times 10^{-9}\,\text{mrad}$. The emittance values expected at the LWFA in Jena are larger than this value, thus no monochromatic spectrum could be achieved with the resulting beam size.

Lower values for β_x are achieved by focusing the beams to the center of the TGU. In this case β_x has a waist at the center of the TGU with the value $\beta_x = L/2$. At the entrance of the TGU this results in $\alpha_{x_0} = 1.0$ and $\beta_{x_0} = L$. β_x along the TGU is shown in Fig. 4.6. The functions are oscillating. For comparison β_x for a drift space is shown in this plot. The focusing of the TGU in the x-z-plane is weak, thus the shape of β_x along

the TGU is almost equal for the different energies. It is just slightly smaller than β_x of the drift space. Hence, for an approximation using an upper limit for the course of β_x along the TGU the focusing can be neglected and the values can be calculated according to a drift space.

4.2.2. Tracking Studies along the TGU and Radiation Field SimulationsTGU

The end values in the previous section were determined under the assumption of a sinusoidal field along the TGU with infinite length. However, the field of the TGU is not a pure sinusoidal field. It contains higher harmonics and there are end fields including the so-called matching periods at the beginning and the end of the TGU. Furthermore the field lines are bent, i.e. the field has an additional component B_x, which increases with the distance to the mid plane.

To take higher field harmonics and the matching periods into account the sinusoidal field is replaced with the simulated field data of the TGU in the calculation of the focusing along the TGU. Tracking studies in the three-dimensional field were performed to include the forces of all field components and the radiation spectra emitted by the bunches in the TGU are simulated.

Influence of the End Fields of the TGU At the beginning and end of the TGU there are the matching periods, which prevent an offset or a deflection of the particle beam by the undulator as described in subsection 2.2.3. To include the influence of the matching periods the field B_y of the magnetic model of the TGU with the matching at the beginning and end was inserted in the analytical equations for the description of the focusing. These data of the simulated field also contain higher field harmonics. As the periods in the middle part of the TGU are not influenced by the end fields, the calculation is performed for a 30-period model of the TGU with a total length of 0.315 m. The center of the TGU is at $z = 0$ m.

Again the field $B_y(z)$ of the TGU along a straight line is divided into subspaces and the average focusing in each subspace is calculated. The calculation starts at 0.925 m distance to the entrance of the TGU to include the fringe fields. The initial parameters at this distance are the parameters assuming a drift space with a beam waist of $\beta_{x,\text{center}} = 0.5$ m at the center of the TGU. The course of the β-function for the beamlet of 120 MeV in both transverse planes are shown in Fig. 4.7. For comparison the course of the β-function in a pure sinusoidal field is shown.

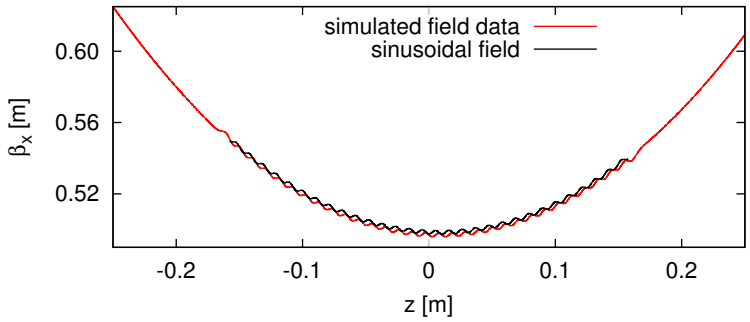

(a) Deflection Plane

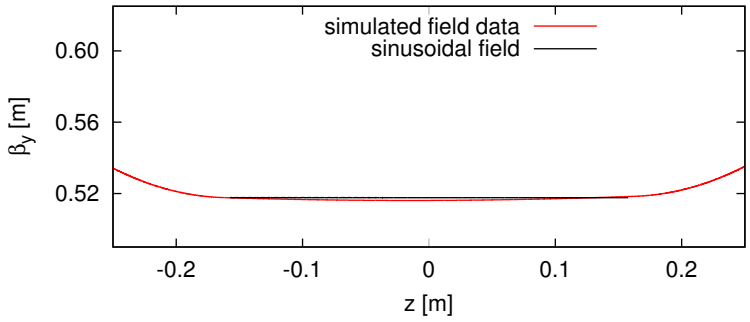

(b) Perpendicular to Deflection Plane

Figure 4.7.: (a) β_x and (b) β_y for 120 MeV along a TGU with 30 periods calculated with the simulated field data and for a pure sinusoidal field (analytical). The calculation starts 0.1 m before the entrance of the TGU for the field data with the end fields to include the fringe fields and for the sinusoidal field at the entrance of the TGU.

In the deflection plane x-z β_x is oscillating for both cases. There is no significant difference in the values of β_x. Comparing both graphs one notices that the period length of the oscillation in the simulated field slightly differs from the one of the sinusoidal field, which is one effect of the end fields. However, here it is of minor interest as it does not influence the averaged beam shape. Note that β_x is not completely symmetric because the start parameters were calculated assuming a drift space. As shown in the previous section there is a small deviation of β-function along a drift space to the β-function in the TGU with the weak focusing of the gradient.

For the y-z-plane the initial values for the constant β_y for the central energy 120 MeV are chosen. With the matching periods β_y shows basically no deviation from β_y calculated with the sinusoidal field.

These calculations show that the matching periods of the TGU have a very small influence on the β-functions in both transverse planes. Therefore the matching periods

	tracking		analytical	
	$\beta_{x,\text{start}}$	$\beta_{x,\text{end}}$	$\beta_{x,\text{start}}$	$\beta_{x,\text{end}}$
108 MeV	1.0259 m	1.0395 m	1.0395 m	0.9671 m
120 MeV	1.0259 m	1.0455 m	1.0395 m	0.9669 m
132 MeV	1.0491 m	1.0388 m	1.0395 m	0.9866 m
drift space			1.0395 m	1.0403 m
	tracking		analytical	
	$\beta_{y,t,\text{start}}$	$\beta_{y,t,\text{end}}$	$\beta_{y,a,\text{start}}$	$\beta_{y,a,\text{end}}$
108 MeV	0.6154 m	0.6332 m	0.60 m	0.7586 m
120 MeV	0.5963 m	0.4804 m	0.60 m	0.4766 m
132 MeV	0.6219 m	0.4476 m	0.60 m	0.4597 m

Table 4.5.: Comparison of the Twiss parameters calculated in tracking studies using OPERA and with the analytical model assuming a sinusoidal field.

are not relevant for defining the end parameters.

Tracking Studies Tracking particles through the tree-dimensional field of the TGU takes the gradient in x into account, but also the magnetic field components in x and z and the coupling between the two transverse planes.

The tracking was done in OPERA [OPERA, 2014] by M. Morcrette using a three-dimensional field map of the TGU without end field effects and matching periods [Morcrette, 2012]. As initial parameters for the electron bunch a Gaussian distribution of the position and momentum in one transverse plane was generated according to the initial values from the analytic estimation. In the second plane the initial position and momentum was set to zero. The distribution was tracked through 99 undulator periods. In Tab. 4.5 the values of β at the starting point of the simulation and after 99 periods are listed for both transverse planes. For comparison the values calculated with transfer matrices for a pure sinusoidal field are given.

For the x-z-plane the values determined with the analytical calculation are smaller than β_x determined in the tracking studies. That means that the alternating focusing and defocusing has a smaller effect on the beam size than expected from the linear estimation. The end value of β_x determined in the tracking studies is closer to the end value of the drift space, though the deviation of 8.1 % or less from the end value of the analytical calculations is only slightly larger than the statistical fluctuation of the initial $\beta_{x,\text{start}}$ up to 2.5 % of the tracking. However, the simulated beams inside the TGU are larger than estimated, what might have a negative influence on the spectra. For the calculation in this thesis the previous assumption of a drift space in the x-z plane seems

not only to be the upper limit for β_x, but also to match the shape of β_x along the TGU well for the case considered here.

In the y-z-plane the difference of the end values between the analytical calculation and the tracking studies for 120 MeV and 132 MeV is in the range of the statistical fluctuations of the start values. For 108 MeV, in contrast, β_y shows a different behaviour, which cannot be explained without a detailed study of the trajectories. However, a small deviation in the field strength has a larger influence on the lowest electron energies, because the deflection in the magnetic field is stronger. That could be responsible for the observed difference. Moreover it is the beamlet with the largest distance to the center, i.e. the influence of the bent field lines might be stronger than for the other beamlets. A detailed study was beyond the scope of the referenced thesis [Morcrette, 2012].

This comparison shows that the analytical model can be applied for an estimation of the end values for the beamlets with energies of 120 MeV or higher. For the beamlets with lower energies the values attained in the tracking studies are smaller than the ones from the analytical model. Still the analytical estimations can be used to determine an upper limit for β_y.

Simulation of the Radiation Spectra of the TGU The simulations of the electron beams presented up to this point are just a description of the effects of the TGU fields on the beam. The crucial criteria for the optimum beam size along the TGU, however, are the spectra of the undulator radiation. To determine the optimum beam parameters at the entrance of the TGU, it is necessary to vary the parameters found in the last sections to prove the validity of the above findings. The criteria to examine are the peak intensity and the width of the emitted radiation spectra.

A detailed study on the radiation spectra was done [Braun, 2013, Braun, 2014] with *wave* [Scheer, 2012]. Several parameters such as the starting position of the particles as a function of their energy and the correction field of the TGU were optimized. Some of the results such as the optimum starting position, but also the spectral acceptance[e] of the TGU with respect to the spectral width of the emitted spectra are important for this thesis. The spectral acceptance of the TGU was determined by scanning the initial phase space coordinates of single electrons in both transverse planes and analyzing the emitted radiation spectra. The phase space volume, in which the central wavelength of the emitted spectrum and the spectral width are in the required range, was defined as

[e]The spectral acceptance is the phase space volume, of which the radiation spectra emitted by the electrons contained in it fulfill certain requirements with respect to the central wavelength and the spectral width.

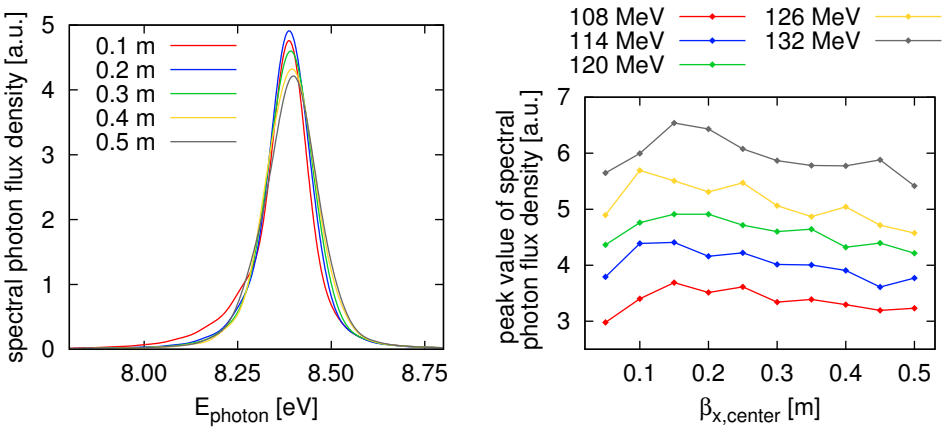

(a) Spectra

(b) Peak Values

Figure 4.8.: (a) Radiation spectra for different $\beta_{x,\text{center}}$ for an electron energy of 120 MeV. (b) Peak value of the spectra for beams of different energies and values of $\beta_{x,\text{center}}$ at the beam waist.

the spectral acceptance of the TGU [Bernhard et al., 2016].

The calculations confirmed the general validity of the analytical description of the beam shape along the TGU [Braun, 2013]. In the y-z-plane a nearly constant beam size can be achieved with the parameters given in the previous sections. The analysis of the spectra showed that a variation of the initial β_y does not have a strong influence on the emitted spectra as the focusing fields along the TGU collimate the beam in this plane. The accepted phase space volume in y is therefore quite large. Still, as end parameters $\beta_y = 0.6\,\text{m}$ and $\alpha_y = 0$ are chosen.

In the x-z-plane in contrast the size of the beam has a strong influence on the emitted spectrum. I performed a scan with a variation of $\beta_{x,\text{center}}$. To limit the number of spectra to be analyzed I restricted the scan to the cases with a beam waist at the center of the TGU.

In the simulation the transverse emittance of the beam is 10 nm rad, the initial Twiss parameters are $\beta_{y_0} = 0.6\,\text{m}$ and $\alpha_{y_0} = 0$. $\beta_{x,\text{center}}$ at the center of the TGU is varied in steps of 0.05 m in the range of 0.05 m to 0.5 m. The start parameters in x at the entrance of the TGU are calculated again under the assumption of a drift space. The magnet model used for the calculation is a 200-period TGU with pure cylindrical coils. 500 electrons are tracked through the central 100 periods. A description of the parameters for the simulation is given in appendix C.4. In Fig. 4.8a the resulting spectra are shown.

The spectrum with the highest peak value and the smallest width is the one with

$\beta_{x,\text{center}} = 0.2\,\text{m}$. This result was not expected: the optimum beam size at the center is not the value for the smallest β-function in x along the TGU.

To include more energies in the range accepted by the TGU the study was extended to bunches with a varying central energy. The starting position in x is set to the optimum position for the according energy, which was determine in [Braun, 2013]. In Fig. 4.8b the peak values of the simulated spectra are shown. The lines show a jitter[f], but for all energies the curves have a maximum in the range of 0.1 m to 0.2 m. The spectral width scales anti-proportional to the peak value having a spectrum with one peak. Therefore the narrowest spectra are expected in the range of the maximum peak values.

These simulations show that the optimum value for $\beta_{x,\text{center}}$ is 0.2 m. The optimum parameter for the design of the beam transport system was therefore set to this value. That corresponds to the end parameters at the entrance of the TGU of $\beta_x = 1.59\,\text{m}$ and $\alpha_x = 2.64$. The curves in Fig. 4.8b have a broad maximum, thus a slight mismatch of the beam size at the center seems to be acceptable.

Note that the emittance has an influence on the emitted spectra. In these simulations the geometrical emittance was 10 nm rad according to the initial parameters for the transport system. Reducing the emittance e.g. to 1 nmrad results in narrower spectra.

4.2.3. End Parameters Used for the Simulations

With the analytical description of the course of the β-functions along the undulator the beam shape along the TGU can be described for known initial parameters. Analysing the spectra the optimum end parameters at the entrance of the TGU listed in Tab. 4.6 were determined.

D	$-20\,\text{mm}$
D'	0
β_{x_0}	1.59 m
α_{x_0}	2.64
β_{y_0}	0.6 m
α_{y_0}	0

Table 4.6.: End values at the entrance of the TGU.

The simulation of the spectra shows that the range of the end parameters is larger

[f] An increase of the number of tracked particles does not reduce this jitter. Therefore it might be caused by the step width of the calculations of the electron trajectories or the mesh of the magnetic field. Choosing a better resolution for these parameters would lead to an increase in the calculation time, which makes such a scan unfeasible.

than expected. A variation of β_x of about 10 % might broaden the spectrum slightly, but the spectral width is still in the acceptable range. The TGU therefore shows positive properties concerning the beam paths inside and the emitted spectra, given that the correction field is adjusted properly. In [Bernhard et al., 2016] the acceptance of the TGU, the optimization of the correction field and further effects influencing the emitted spectra are described in more detail.

5. Layout of the Beam Transport System

In this section the design and the simulations for the layout of the beam transport system are presented. The aim is to design a compact beam transport system from the LWFA to the TGU with the initial and end parameters deduced in chapter 4 and with an accepted relative energy bandwidth in the range of a few percent. For the aimed energy acceptance it is necessary to implement a correction for the chromatic error. To keep the system compact, combined quadrupole-sextupole magnets are foreseen.

The sextupoles for the chromatic correction have to be placed in a dispersive region in a transport line where the particle orbits for different energies are locally separated and a focusing field varying with the transverse position can be applied. Nevertheless the system also requires quadrupoles in sections where the dispersion is zero. Otherwise the dispersion and the β-function of the beam are coupled as the quadrupoles act on both of them. Thus it is impossible to match both, the dispersion and the Twiss parameters [Haerer, 2013]. That has to be considered for the layout.

In the first part of the chapter the optimization of the linear layout for the transport system is summarized. I started from a very simple symmetric system, which was modified step by step to match all the end parameters to the required parameter of the TGU. The total length of the system was set to 5 m. For the linear dispersive system found as solution a brief estimation for the evolution of the longitudinal phase space and the influence of coherent synchrotron radiation is presented at the end of section 5.1.

The implementation of the chromatic correction is described in section 5.2. The possible positions for the sextupoles are compared and the sextupole strength is optimized. With the optimized sextupole strength the radiation spectra of the TGU are simulated.

In the last part of this chapter a modified linear beam transport system with a more compact layout and a reduced number of quadrupoles for the first stage of the experimental tests is presented.

5.1. Layout of the Linear Beam Transport System

With the end parameters at the TGU and the initial parameters of the LWFA estimated in chapter 4 the layout of the linear beam transport optics can be optimized. The number of magnets required for the beam transport is too large for an optimization routine including all strengths of the magnets and the lengths of all drift spaces. Therefore I started with a simple layout with less free parameters and modified this system to include all required end parameters and boundary conditions step by step. In this way one can learn more about the crucial optimization parameters of the system and to find parameters that can be kept fixed during the optimization.

The optimization of the layout of the optics is done in several steps: First a symmetric achromatic system was studied, i.e. a system with zero dispersion at the exit, which means the end position does not depend on the electron energy. Next, the strength of some quadrupoles and the length of some drift spaces was changed to match the Twiss parameters required by the TGU. Last the achromatic section was modified to match the end parameter for the dispersion at the exit of the beam transport system.

5.1.1. Collimation of the Beams from the LWFA

Directly after the LWFA and before the dispersive section of the transport system the beams have to be collimated. Several options for magnet configurations are possible for that: a quadrupole doublet or triplet or a solenoid. In all cases the divergence of the source has to be compensated such that the beam enters the first dipole slightly focused in both transverse planes.

Solenoids focus the beam in both planes in contrast to a quadrupole. Unfortunately the focusing gets inefficient for relativistic particle energies, thus the magnetic field required for the focusing is strong. To achieve a focal length of 1.0 m for an electron energy of 120 MeV with a solenoid of length 0.3 m according to equation 2.23 in the thin lens approximation a longitudinal field strength of around 1.5 T is needed. This field strength can be achieved in normal-conducting electromagnets with some effort. However, for a compact setup an even shorter solenoid is required with a larger field strength. To avoid such strong magnets in the setup for my studies I chose a collimation consisting of quadrupoles.

For the calculations a minimum distance of 0.3 m to the exit of the LWFA is assumed.[a]

[a] This distance is defined by the required space for the mounting, control and gas supply of the plasma target and the mounting and coils of the quadrupole. With a more compact plasma target the distance can be shortened in the setup, which would have a positive effect on the beam transport system. Dam-

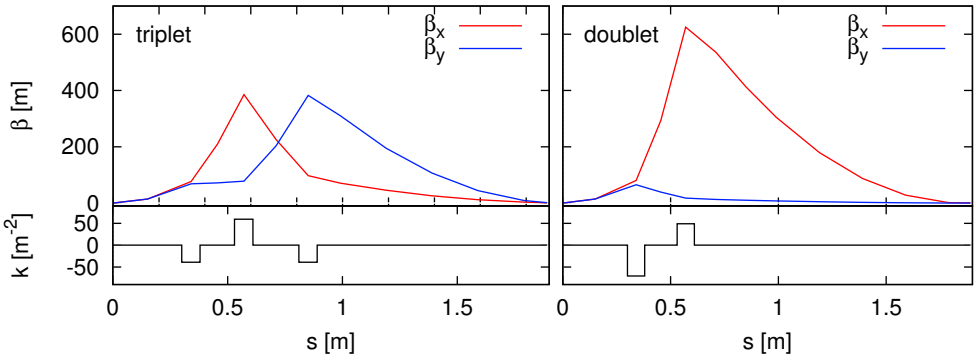

Figure 5.1.: Comparison of the collimation of the beam from the LWFA with a triplet (left) and a doublet (right). In the upper plots β_x and β_y are shown, in the lower plots the quadrupole strength k is displayed. The initial parameters for both planes are $\alpha_0 = 0$ and $\beta_0 = 1.6\,\text{mm}$.

The first quadrupole is moved as close as possible to the source to keep the β-functions small. The focusing strength of this quadrupole should be moderate as it focuses in the first, but defocuses in the second plane. That means the stronger the first quadrupole is, the more defocused is the beam in the defocusing plane. For keeping the beam small in the second plane the second quadrupole is placed as close as possible to the first quadrupole. Using a triplet the third quadrupole completes the focusing of the beam in the first plane.

In Fig. 5.1 the comparison of the collimation with a triplet and a doublet is shown. For a triplet β has a moderate value in both planes while with the doublet β is quite large in one plane and small in the second. It is clear that in the case of the triplet the focusing of the beams is more homogeneous. Therefore a triplet is chosen for the collimation. I set the strength of the first quadrupole such that the maxima of β_x and β_y reach approximately the same value.

5.1.2. Configuration of the Magnets

The layout for the beam transport system I started with is completely symmetric as shown in Fig. 5.2a. The beam from the LWFA is collimated in triplet 1, then a dispersive section with two dipoles and three quadrupoles follows and before the TGU another triplet is used to match the end parameters at the exit of the transport system.

The calculation of the linear beam functions of the beam transport system were done

ages of the magnets caused by the laser pulse are not an issue here as the laser beam diameter is still small enough that the laser passes the gap of the magnets.

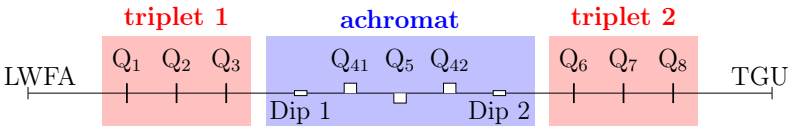

(a) Basic Layout

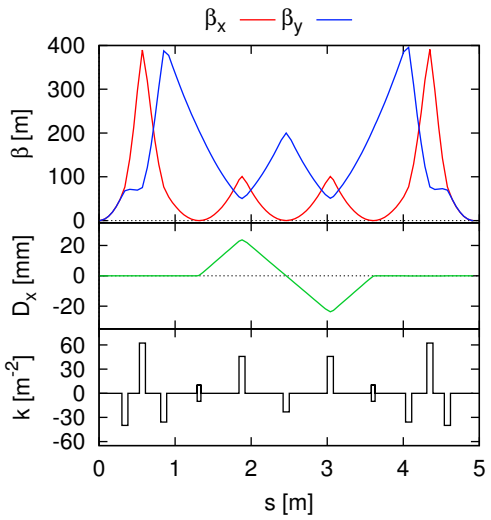

(b) Symmetric Functions

Figure 5.2.: (a) Basic layout of the beam transport system with nine quadrupoles Q_i and two dipoles Dip 1 and Dip 2. (b) β and the dispersion D for a completely symmetric setup with a deflection angle of the dipoles of ± 43.5 mrad for 120 MeV.

with the Twiss Module of MAD-X [MAD-X, 2002]. The MAD-X elements and their parameters used for the calculation are listed in appendix C.1.1. For each magnet a minimum distance to the yoke has to be kept, the space for the coils. For the quadrupoles this distance is 80 mm on each side, for the dipoles 100 mm. The initial parameters for the calculation are $\beta_0 = 1.6$ mm and $\alpha_0 = 0$. The same parameters are used for both planes.

An explicit configuration for symmetric beam functions is shown in Fig. 5.2b. For this layout the end parameters at the exit are equal to the initial parameters of the LWFA and the distances and magnet strengths are symmetric to Q_5 except the dipoles, which deflect in opposite directions.

The β-functions were chosen such that they fulfill different conditions: Triplet 1 was used to generate a beam waist in x in the first dipole and in y in Q_{41}. The defocusing of a quadrupole was minimized at a beam waist in the defocusing plane. As a consequence a beam waist should be chosen in the defocused plane in strong quadrupoles. At the

position of Q_{41} and Q_{42} β_y should have a minimum. At the position of Q_5 there should be a beam waist in x.

To understand the influence of the single quadrupoles on the end parameters, the matching was done by hand, not with the optimization algorithm provided by MAD-X. For achieving a symmetric shape of the β-functions and the anti-symmetric shape of the dispersion along the transport system as shown in Fig. 5.2b first triplet 1 was configured. The dispersion was controlled with Q_{41} and Q_{42}. Q_5 mainly influences β_y. The symmetric course of β_y was controlled with this quadrupole, while the shape of β_x was changed by adapting the strength of Q_2. While changing the strength of the quadrupoles between the dipoles, the β-function in the defocused plane was hardly changed. That made the matching by hand easier. The end parameters of this configuration are listed in Tab. 5.1.

	x-z-plane	y-z-plane	optimum value
β	1.59 mm	1.57 mm	1.60 mm
α	-3×10^{-4}	-1×10^{-3}	0
D	1×10^{-5} m		0 m
D'	2×10^{-4}		0

Table 5.1.: End parameters of the symmetric beam transport system with the optimum values, which are the same for both planes in this case. Note that the parameters are not perfectly matched as the optimization was done by hand.

In the next step the symmetric layout was modified such that the Twiss parameters at the end of the beam line were matched to the required end parameters. The last drift space was set to the minimum distance of 0.5 m to the TGU[b]. Therefore the distances between quadrupole Q_6 and the second dipole and the distances in triplet 2 had to be shortened to keep the total length of the transport system around 5 m.

For the matching the strengths and positions of the quadrupoles in triplet 2 and the strength of Q_5 were modified. The quadrupole strengths in triplet 1 and of the quadrupoles Q_{41} and Q_{42} were kept unchanged as the first collimation and the dispersion was controlled by them like in the symmetric layout.

To scan the available parameter range of the stength of these four quadrupoles a Monte-Carlo simulation was performed. For the quadrupoles in triplet 2 the sign of the polarity was varied with the boundary condition of an alternating polarity for these

[b]The length from the entrance of the cryostat to the center is 0.885 m. Additionally the minimum distance to the last quadrupole plus some space for the connection of the cryostat to the vacuum chambers has to be taken into account. The required end parameters are determined at the position of the entrance of the TGU 0.525 m before the center of the cryostat.

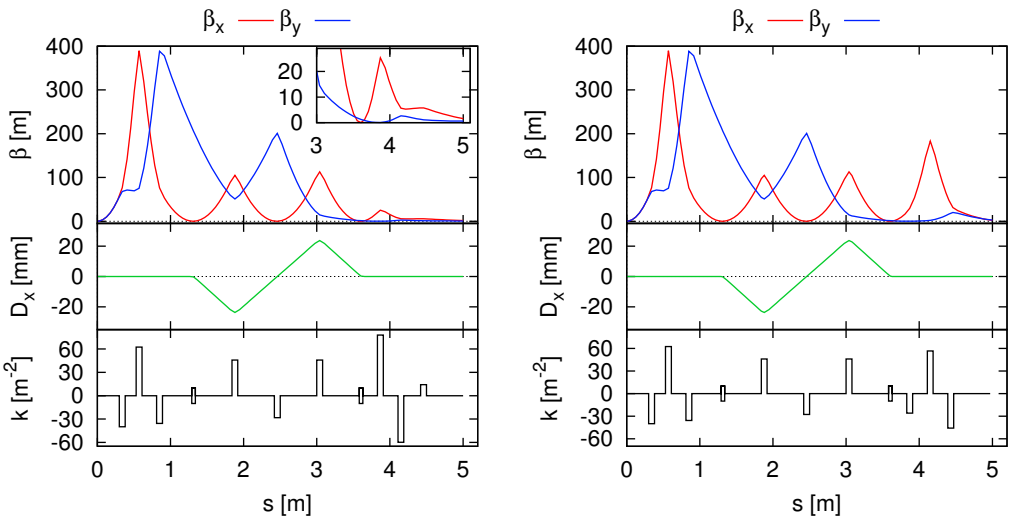

(a) Preferred Layout (b) Second Solution

Figure 5.3.: Comparison of two types of solutions from the Monte-Carlo simulation for the achromatic beam transport system. For each solution the β-function, the dispersion D and the quadrupole strengths k are shown. (a) Solution with a smooth reduction of the beam size along the transport system. The inlet shows a zoom on the β-functions. (b) Solution with the alternative polarity of triplet 2 and a strong peak in β_x after the second dipole. The deflection angle of the dipoles for both cases is ± 43.5 mrad for 120 MeV.

three quadrupoles. For the dipoles both polarities were tested. Q_5 was kept as focusing quadrupole for β_y. For finding the best solution in the parameter range scanned with the Monte-Carlo simulation the quadrupole strengths of the solutions with a small deviation of the end parameters to the required values were compared. The method is described in detail in appendix C.2.

The configurations with end parameters close to the target parameters are restricted to two small intervals in a parameter range with opposite polarities of the quadrupoles in triplet 2: focusing-defocusing-focusing and defocusing-focusing-defocusing in x. For each case one solution is plotted in Fig. 5.3. A comparison of these two cases shows that with the first combination (Fig. 5.3a) the β-functions are smoothly reduced along the beam transport system, while with the second configuration (Fig. 5.3b) β_x has a strong peak at the position of Q_7. For the following calculations the first configuration is favorable because it provides smaller values of β_x after the second dipole. That means the beam size is smaller in Q_6 to Q_8, which will be laid out as combined quadrupole-sextupole magnets for the chromatic correction. Thus the distortion of the phase space

profiles by the non-linear field is smaller for this solution.

The chosen beam transport system was optimized using the simplex routine of the matching module of MAD-X [MAD-X, 2002]. The sign of the quadrupole strengths was kept fixed during the optimization. The optimized beam transport system is shown in Fig. 5.3a. The beam parameters at the exit of the transport system are listed in Tab. 5.2.

	in x		in y	
	optimized value	required value	optimized value	required value
β	1.58 m	1.58 m	0.60 m	0.60 m
α	2.625	2.625	-2×10^{-8}	0
D	-3×10^{-6} m	0 m		
D'	-3×10^{-6}	0		

Table 5.2.: Optimized end parameters of the achromatic beam transport system compared to the required parameters of the TGU.

In the next step the achromatic setup was modified to match in addition to the Twiss parameters also the dispersion to the end parameter required by the TGU.

5.1.3. The Dispersive Beam Transport System

Starting from the achromatic layout the dispersion has to be matched to -20 mm at the end of the transport system. The dispersion can be varied with the strength of Q_{41} and Q_{42}, with a shift of Q_5 or with a change of the position of the dipoles. In all cases triplet 2 influences the dispersion. Thus the Twiss parameters cannot be matched at the TGU independently from the dispersion.

It turned out that it is helpful to keep the position of Q_5 close to the zero-crossing of the dispersion and at the beam waist of β_x to minimize influence of Q_5 on both functions. That means shifting Q_5 is not an option for the dispersion matching. A significant change of the quadrupole strength of Q_{41} and Q_{42} neither seem reasonable as this zero-crossing would be shifted and the anti-symmetric shape of the dispersion function would be lost.

Therefore the best option for changing the dispersion is a shift of the second dipole towards the end of the transport system such that the dispersion has a positive value at the position of the dipole. The quadrupole triplet 2 was used to match the dispersion function and the Twiss parameters. As Q_5 is located at the zero-crossing of the dispersion the shape of β_y could be modified without influence on the dispersion. β_x in contrast had to be varied with an adaption of Q_2 in triplet 1 as there was no quadrupole

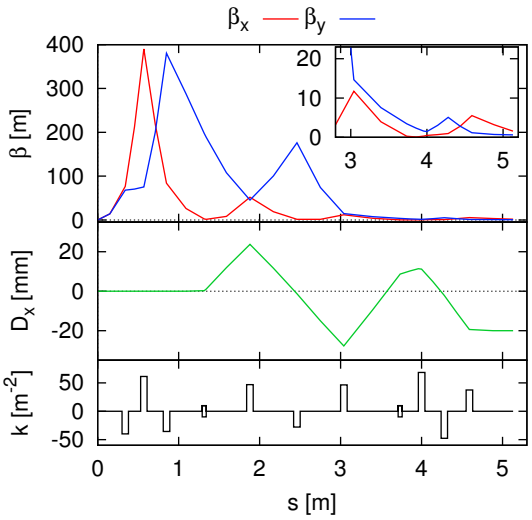

Figure 5.4.: The β-function, the dispersion D and the quadrupole strength k along the dispersive beam transport system. All beam parameters are matched to the required parameters at the TGU. The inlay shows a zoom on β. The deflection angle of the dipoles for 120 MeV is ± 43.5 mrad.

focusing in x in the dispersive section, which could be modified without an influence on the dispersion.

To achieve the required dispersion it was necessary to set the dipoles strength to the maximum value, which corresponds to a deflection angle of 43.5 mrad for 120 MeV. Furthermore the polarity of the dipoles was changed.

For the matching with help of the matching module of MAD-X quadrupoles Q_2, Q_{42}, Q_5, Q_6, Q_7 and Q_8 were varied. The result is shown in Fig. 5.4. Compared to the achromatic system the values of Q_2 and of Q_{42} are almost unchanged, while the strength of all quadrupoles in triplet 2 is decreased.

	in x		in y	
	optimized value	required value	optimized value	required value
β	1.58 m	1.58 m	0.60 m	0.60 m
α	2.625	2.625	-1×10^{-8}	0
D	-20.0 mm	-20.0 mm		
D'	-1×10^{-10}	0		

Table 5.3.: Optimized end parameters of the dispersive beam transport system matched to the required parameters of the TGU. For comparison the target parameters are listed.

The presented solution has three zero-crossings of the dispersion, which is surpris-

ing. A solution with the opposite sign of the dipole fields and only two zero-crossings would have been expected as a more stable system. However, the matching with the polarity of the dipoles used in the previous setup does not lead to reasonable results. Unfortunately the drift spaces cannot be shortend to achieve a more compact beam transport system with this dispersive configuration.

5.1.4. Evolution of the Bunch Length

Although the longitudinal shape of the bunch is not of importance for the current setup and was therefore not optimized, it is discussed shortly here.[c] For future setups, however, it might become important to preserve the short bunch length along the beam transport system, e.g. for a beam transport system at a FEL.

The 6×6 linear transfer matrix for the beam transport system was calculated with *elegant* using the matrix output for linear systems. For two systems, the achromatic beam transport system and the dispersive beam transport system, the evolution of the bunch length was analyzed. The matrix elements at the end of the beam transport system, which describe the influence on the bunch length, are listed in Tab. 5.4.

To estimate the longitudinal displacement of single electrons the matrix elements are multiplied with the according initial parameter, i.e. R_{56} is multiplied with the energy deviation δ, R_{51} with the x-position and R_{52} with the angle x' to the beam axis. An energy deviation of $\delta = 1\,\%$ of a particle leads to a longitudinal displacement of around 0.3 µm for the achromat and 3 µm for the dispersive system. Assuming an initial bunch length of 0.75 µm (rms) the bunch length is increased by 40 % in the achromatic system, but it is still in the range of 1 µm. For the setup with the matched dispersion in contrast the bunch length is increased by a factor of four for each percent of energy deviation. An additional longitudinal displacement is caused by the initial transverse position in the range of some micrometers the initial angle of few milliradian.

	achromatic system	dispersive system
R_{51}	-5.53×10^{-5}	0.113
R_{52}	$-5 \times 10^{-7}\,\mathrm{m}$	$1.77 \times 10^{-3}\,\mathrm{m}$
R_{56}	$3.15 \times 10^{-5}\,\mathrm{m}$	$-3.64 \times 10^{-4}\,\mathrm{m}$

Table 5.4.: Matrix elements of the linear transfer matrix describing the longitudinal phase space for the achromatic beam transport system shown in Fig. 5.3a and the dispersive system shown in Fig. 5.1.

[c] To demonstrate the working principle of the TGU the spectrum of the undulator radiation is analyzed and there are no diagnostics foreseen for a temporally resolved measurement.

However, the dispersive transport system presented still provides a bunch length that is considered as ultra-short. With the three zero-crossings of the dispersion along the transport system the path length difference due to an energy deviation of single electrons and therefore the matrix element R_{56} are small. For a completely isochronous beam transport system, i.e. a system that preserves the bunch length, a slight modification of the magnet positions and parameters is necessary, while the general layout of the transport system can be left unchanged.

5.1.5. Influence of Coherent Synchrotron Radiation

The synchrotron radiation emitted by the electron bunch has a very broad spectrum reaching to the far infrared and terahertz range. For short bunches the wavelength of the radiation in this spectral range can be similar to the bunch length. As a consequence the radiation is emitted coherently, the so-called coherent synchrotron radiation (CSR) [Wiedemann, 2003]. The intensity of this radiation scales with the square of the number of electrons, not linearly like for the incoherent emission, and is therefore much higher than for the incoherent synchrotron radiation. On a bent trajectory the radiation fields of the CSR can interact with the electrons and thus influence the bunch shape.

With the ultra-short bunches of the LWFA CSR might deteriorate the bunch shape along the beam transport system. To study this effect simulations with *elegant* were performed. *elegant* provides a one-dimensional calculation of the CSR-effects on the bunch. For the calculation the bending magnets are replaced by "CSR-bends".

In Fig. 5.5 the phase space profiles for varying bunch charge are shown. On the left there are the undisturbed profiles without the influence of CSR. Setting the total charge of the bunch to 10 pC the phase space profiles are almost unchanged. For a bunch charge of 50 pC a slight disturbance of the profile in the x-x' phase space can be observed. Increasing the bunch charge to 100 pC or more, the influence of the coherent synchrotron radiation is visible in the now clearly disturbed profiles.

In the experiment a bunch charge in the range of 10 pC is expected considering only the monoenergetic peak, not the background of low-energetic electrons (see section 4.1). In this range the influence of the coherent synchrotron radiation can be neglected. An increase of the bunch charge up to about 100 pC could be tolerated. For bunches of higher charge the CSR-effects have to be included in the design of the transport system. Their influence can be reduced for example by using smaller deflection angles in the bending magnets.

Unfortunately it is not clear if the one-dimensional model provides sufficient accu-

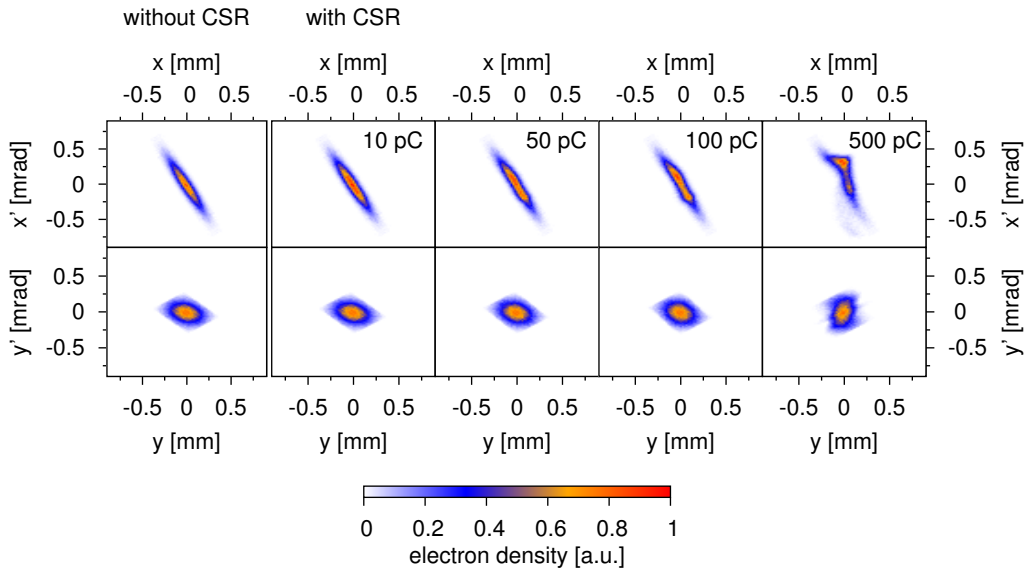

Figure 5.5.: Phase space distributions at the end of the beam transport system under the influence of space charge effects in the bending magnets. The first profile shows on the left shows the undisturbed distributions, to the right the bunch charge and therefore the influence of the CSR is increased.

racy for the estimation of the CSR effects. The Derbenev criterion, which gives a relation between the bunch size, the bunch length and the bending radius of the trajectory in the magnet [Derbenev et al., 1995], is in the range of 0.3 to 0.2. It should be much smaller than one for using the one-dimensional model. However, three-dimensional simulations of the CSR-effects in a similar setup also confirm that the effects of CSR for a bunch charge in the range of up to 20 pC only have a small influence on the bunch and can be tolerated [Maier et al., 2012].

5.2. Correction of the Chromatic Aberration

The beam transport system is supposed to work for a relatively large energy range. In this section the influence of the chromatic aberration caused by the quadrupoles is investigated and an option for the correction with sextupole magnets is discussed.

The TGU accepts electrons in the energy range of $\pm 10\,\%$ around the central energy.[d] Ideally the beam transport system should work for a comparable energy range. Such a

[d] Studies showed that the TGU does not only work for a central energy of 120 MeV. The working principle can be extended to central energies in the range of some tens to few hundred mega-electronvolt if the undulator field is adapted.

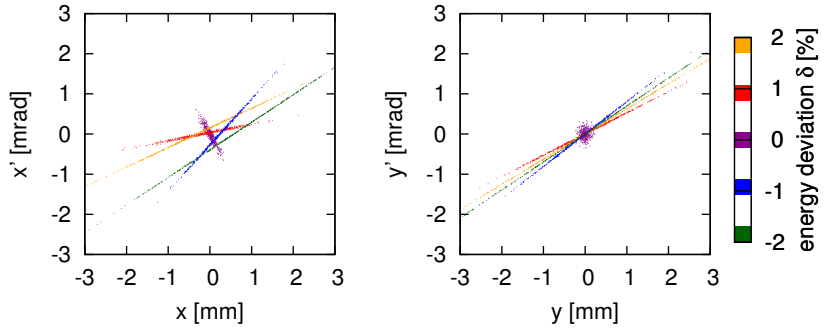

Figure 5.6.: Phase space profiles for five momoenergetic beamlets at the exit of the chromatically uncorrected beam transport system. The central energy is 120 MeV, the energy deviation from the central energy is depicted with the color code of the electrons.

large range is not achievable with the approach under investigation here. It is, on the other hand, not necessarily required. Usually the energy bandwidth of single bunches of the LWFA is in the range of few percent (FWHM). If the central energy of the bunches is stable, it is sufficient to transport such an energy bandwidth. For first calculations the energy spread is set to low values and it is increased step by step to determine the upper limit of the energy bandwidth that can be transported.

In Fig. 5.6 five monoenergetic beamlets of different energies tracked through the setup without chromatic correction are shown. The influence of the chromatic aberration is clearly visible: The ellipses of the beamlets with energy deviation in the x-x' phase space are rotated and stretched. In the y-y' phase space the beamlets with these energies do not have a focus at the entrance position of the TGU. To correct for this chromatic aberration a sextupole component is added to selected quadrupoles.[e] Ideally after the correction all monoenergetic beamlets have the shape of the beamlet with the central energy. In x-x' phase space the center of the single beamlets is shifted due to the required dispersion at the entrance of the TGU.

In this section the realization of a chromatic correction for the transport system is described.

5.2.1. Optimum Position and Strength of the Sextupoles

For the implementation of the chromatic correction it is important to chose the location of the sextupoles carefully. The requirements for this choice are described in section 2.1.5: The sextupoles must be placed in a dispersive region of the beam transport

[e] As explained in chapter 3 it was decided to use combined quadrupole-sextupole to keep the transport system as compact as possible.

system where the geometric aberration of the sextupole can couple to the chromatic aberration of the beam transport system. For the setup of the dispersive beam transport system four of the quadrupoles fulfill this requirement: Q_{41}, Q_{42}, Q_6 and Q_8. Quadrupoles Q_5 and Q_7 are located in the dispersive region but at or near a zero-crossing of the dispersion. The coupling for the chromatic correction is therefore not efficient at these positions.

To obtain the best results for the sextupole correction and to minimize the additionally introduced geometrical aberration, the sextupoles should be implemented in pairs: One sextupole in a dispersive region, a second sextupole of same strength but opposite polarity at a position where the characteristic functions $S(s)$ and $C(s)$ introduced in section 2.1 have the same values and the dispersion function is zero. Unfortunately in the presented layout the beams have to be continuously focused along the beam transport system, thus there are no positions with similar characteristic functions. With the magnets available for this setup and by keeping the compact design, a redesign taking care of this condition is not possible. On the other hand, most of the quadrupoles are located at a beam waist in the non-focusing plane, what minimizes the distortion in this plane by the sextupoles.

From the profiles shown in Fig. 5.6, it is clear that the transport system has a significant chromatic error for the energy range of 120 MeV ± 2 %. For the first calculations I reduced the energy spread to ± 0.5 % to have a less distorted beam. For the simulations a bunch consisting of seven monoenergetic distributions with 500 electrons each in the energy range of 120 MeV± 0.5 % is tracked through the model of the beam transport system using the PTC module of MAD-X [PTC, 2002]. The source size $\sigma_{x,y}$ of the LWFA is 4 µm and the source divergence $\sigma_{x',y'}$ is 2.5 mrad. For both quantities a Gaussian distribution is assumed. The geometrical emittance is therefore 10 nm rad, the product of these two quantities. The explicit commands of the tracking routine are listed in appendix C.1.1.

To find the best configuration for the sextupole components, the influence of a single sextupole component on the phase space profile applied to quadrupoles Q_2 to Q_8 was tested. Each sextupole component was increased to positive and negative values of m till a distortion of the phase space profile in x-x' was observed. The according phase space profiles are shown in the appendix in Fig. C.2. For the sextupole component of quadrupole Q_2 and Q_3 a strong distortion of the x-x' phase space even for small values of the sextupole strength is observed. A lower but still strong distortion is caused by the sextupole component of Q_{41}. The large beam size at the position of the sextupole is the reason for this strong distortion. With a sextupole at the position of Q_5 the shape of

the phase space profile is blurred in both transverse planes. A sextupole at these four positions should not be used for the chromatic correction.

Though a sextupole component for Q_6, Q_7 and Q_8 does not directly lead to a distortion of the phase space profile, the additional rotation angle observed in the uncorrected profiles cannot be corrected by a sextupole at these positions.

For the optimization the strength of several sextupoles was increased step by step trying to correct the rotation mismatch and keeping the distortion small. I tried to optimize the sextupole configuration based on a Monte-Carlo simulation using the statistical definition of the Twiss parameters given in equation 2.29 to describe the subbunches. Due to the strong distortion of the phase space profiles with the increase of the sextupole strengths these statistical parameters did not give a reasonable optimization criterion.

In Fig. 5.7 the best result achieved with the optimization by hand is shown. Q_{42}, Q_6 and Q_8 were used to correct the chromatic aberration, Q_7 to compensate the geometric aberration generated by the other sextupoles. The strength of the sextupole component m of Q_{42} is $-200\,\mathrm{m}^{-3}$, of Q_6 $500\,\mathrm{m}^{-3}$, of Q_7 $-700\,\mathrm{m}^{-3}$ and of Q_8 $200\,\mathrm{m}^{-3}$.[f] Increasing the sextupole strength induces a visible bending of the phase space ellipse, but still the rotation angle of the ellipse at the center is basically unchanged.

The average angles of the beam shown in Fig. 5.7 on the left are in the required range of $\pm 0.1\,\mathrm{mrad}$ [Morcrette, 2012], the average value in x determines the central wavelength of the emitted radiation. Compared to the uncorrected system the center of the subbunch with $\delta = 0.5\,\%$ is shifted closer to the center of the TGU, which leads to a shift of the emitted wavelength.

However, this is not a satisfying solution, as the target parameters at the TGU are not achieved for the two beamlets having an energy deviation.

5.2.2. Chromatic Correction with Improved Source Parameters

The strong distortion of the phase space profile is caused by a large beam size at the position of the sextupoles: The variation of the nonlinear field of the sextupoles over the diameter of the beam is large for strong sextupoles. The phase space profile is bent. For smaller beams this effect is reduced. The size of the electron beam depends on the β-function and the transverse emittance. The β-function is determined by the configuration of the beam transport system, the emittance for the beams considered here is the product of the source size and divergence. The initial values of those quantities are estimated quite conservatively for the calculations. Using capillaries as target, lower

[f] The strength of the quadrupoles is not changed.

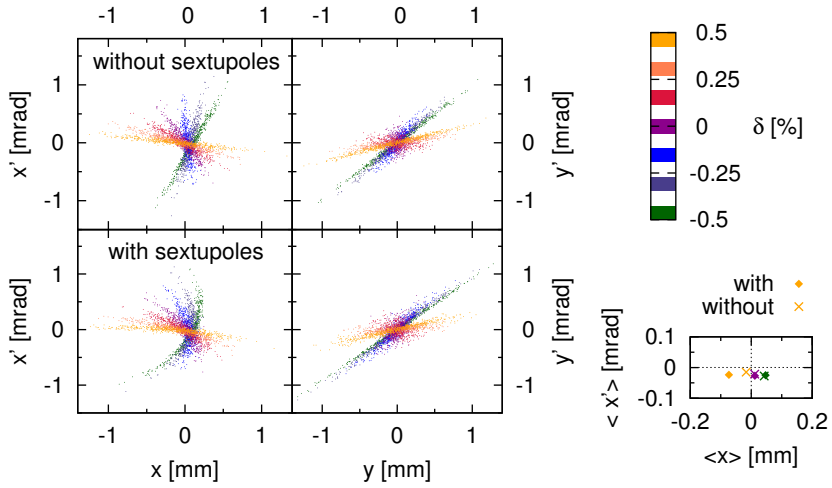

Figure 5.7.: Phase space distribution at the exit of the beam transport system of seven monoenergetic beamlets with an energy deviation δ indicated by the color code. The distributions shown in the upper plots are simulated with the quadrupole system, in the lower plots the sextupole correction is introduced. On the right the average value of the position and angle in x are shown for the corrected system 'with' and the uncorrected 'without'.

values can be achieved in measurements [Weingartner et al., 2012], which should lead to less distortion of the phase space profiles by the sextupoles.

Therefore the initial parameters for the simulations are improved in the accessible parameter range of LWFAs to study their influence on the chromatic correction: The source size is decreased from 4.0 µm to $\sigma_{x,y} = 1.0$ µm and the source divergence is set from 2.5 mrad to $\sigma_{x',y'} = 1.0$ mrad. In Fig. 5.8 the simulated phase space profiles are shown for a reduced source size, a reduced source divergence and for a reduction of both quantities.

The profiles in Fig. 5.8 indicate that a reduction of the source size by a factor of four leads to sharper boundaries of the phase space distribution. That means the distribution in the local coordinates x and y are narrower, while the shape and extension of the distribution is almost unchanged. A reduction of the initial source divergence in contrast leads to a smaller size of the distributions in both the local and the angular coordinates. With this reduction the beam size along the beam transport system and inside the TGU is decreased. That leads to improved conditions for the chromatic correction and as a consequence of the smaller beam size along the TGU a reduction of the radiation bandwidth.

At the bottom of Fig. 5.8 the average angle and position of the distributions are

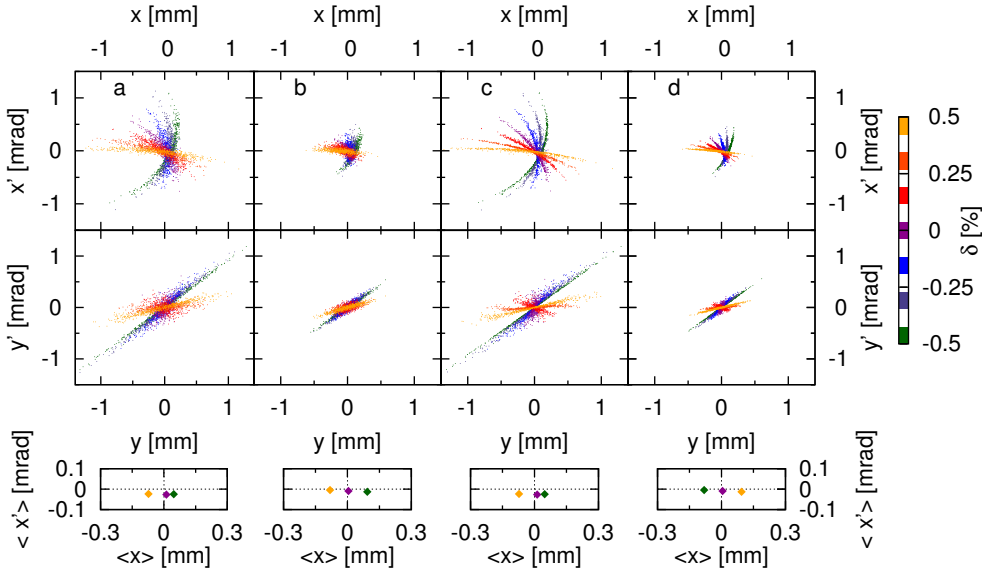

Figure 5.8.: Phase space profiles for a variation of the source parameters of the LWFA for the same configuration of the magnets as in Fig. 5.7: (a) the source parameters assumed for the previous calculations $\sigma_{x,y} = 4\,\mu\text{m}$ and $\sigma_{x',y'} = 2.5\,\text{mrad}$, (b) a reduced source divergence of $\sigma_{x',y'} = 1\,\text{mrad}$, (c) a reduced source size of $\sigma_{x,y} = 1\,\mu\text{m}$ and (d) a reduction of both quantities. At the bottom the average values for x and x' are plotted.

shown. For case b and d with a reduced source divergence the average angle at the exit of the beam transport system is reduced and a equally spaced position in x is achieved. Both quantities are important for the quality of the radiation spectra.

The acceptance of the TGU in the x-x' phase space is more critical as in the y-y' phase space as a mismatch in x directly leads to a broadening of the radiation spectra [Braun, 2014]. Therefore I focus on the x-x' plane for the optimization.

With the modified source parameters the chromatic correction by the sextupoles is again optimized. The sextupole components of Q_{41}, Q_{42}, Q_6 and Q_8 are used for correcting the rotation of the ellipses in the x-x' phase space. The sextupole component of Q_2 is used to compensate for the deformation of the ellipses. The resulting phase space distributions are shown in Fig. 5.9a, the according values of the sextupole strengths are listed in Tab. 5.5.

The mismatch of the rotation of the phase space ellipses icon be corrected up to a certain degree with this configuration. The strength of the sextupoles is increased compared to the configuration shown in Fig. 5.7, but the distortion of the profile is kept small due to the reduced emittance and beam size along the beam transport system. A further reduction of the source size and especially the divergence would lead to a

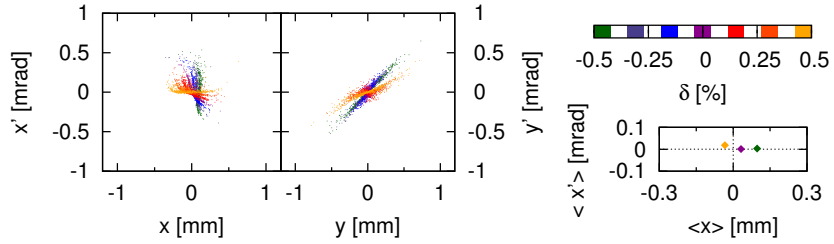

(a) Energy Spread $\delta = \pm 0.5\,\%$

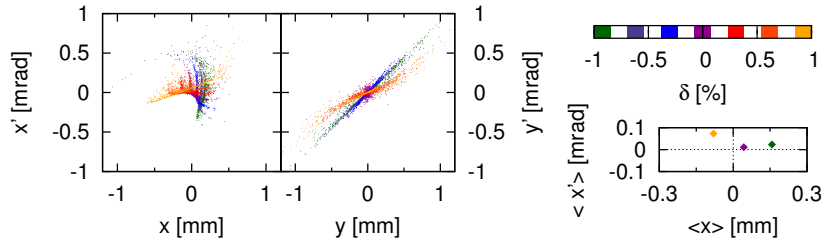

(b) Energy Spread $\delta = \pm 1.0\,\%$

Figure 5.9.: Phase space distribution with a reduced source size and divergence and optimized sextupole strengths for an energy spread (a) $\delta = \pm 0.5\,\%$ and (b) $\delta = \pm 1.0\,\%$.

position	sextupole strength m
Q_2	$20\,\mathrm{m}^{-3}$
Q_{41}	$30\,\mathrm{m}^{-3}$
Q_{42}	$-800\,\mathrm{m}^{-3}$
Q_6	$2000\,\mathrm{m}^{-3}$
Q_8	$1800\,\mathrm{m}^{-3}$

Table 5.5.: Optimized sextupole strengths.

further improved chromatic correction. However, with the recent experimental results a further reduction does not seem reasonable.

As the chromatic correction improves the phase space profile in the case discussed the energy spread is increased. In Fig. 5.9b the phase space profile for an energy spread of $\pm 1.0\,\%$ with adapted sextupole strength is shown. In this case the phase space profiles are again bent and smeared out. For the condition of these simulations the chromatic aberration for an energy spread of $\pm 1.0\,\%$ cannot be corrected.

5.2.3. Simulated Radiation Spectra of the TGU

Up to this point in the chapter the layout of the beam transport system and the configuration of the magnets optimized to match the target parameters estimated in chapter 4

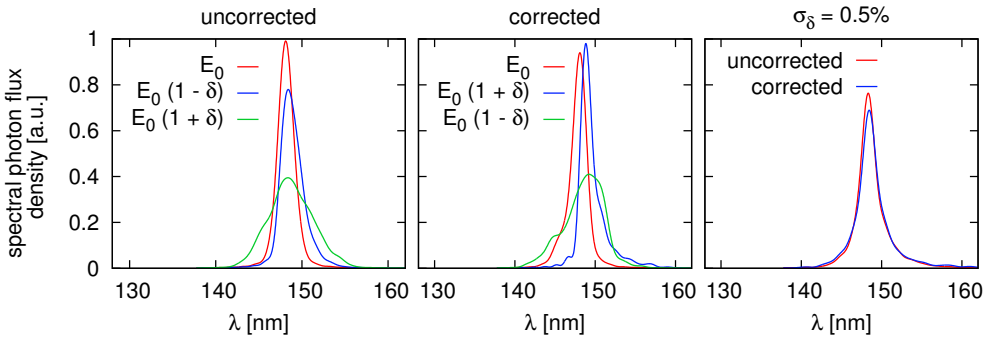

(a) Spectra for $\delta = 0.5\,\%$

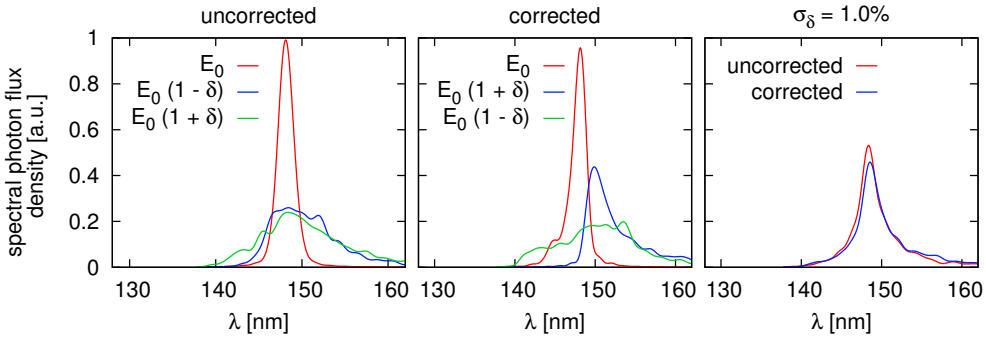

(b) Spectra for $\delta = 1.0\,\%$

Figure 5.10.: Radiation spectra emitted by subbunches with the energy deviations δ tracked through the dispersive beam transport system for the uncorrected system on the left and the system with the sextupole correction in the middle. In the plot on the right the spectrum emitted by a bunch with a Gaussian energy distribution with the relative energy spread δ is shown. In (a) the relative energy spread δ is 0.5 %, in (b) it is 1.0 %. The according phase space distributions are shown in Fig. 5.9. All spectra are normalized to the maximum of the uncorrected configuration.

were presented. However, the crucial criteria for the bunch shape at the exit of the beam transport system are the radiation spectra of the TGU. Therefore the emitted spectra for two of the optimized configurations are simulated with *wave* [Scheer, 2012]: The dispersive beam transport system with chromatic correction for bunches with an energy spread of $\delta = 0.5\,\%$ and $\delta = 1.0\,\%$.[g] In Fig 5.10 the spectra of the according systems with and without the chromatic correction are compared. In the plot on the left and in the middle the spectra emitted by three monoenergetic subbunches, one with the central energy and one for each energy with $E_0(1 \pm \delta)$ are shown. Each subbunch consists of

[g]Note that the values for the energy spread given in publications usually is the full width at half maximum (FWHM) of the energy distribution. The values given for the LWFA in Jena in section 4.1 also correspond to the FWHM.

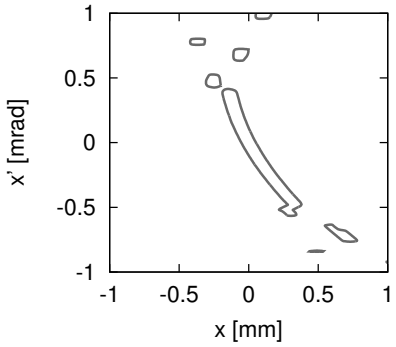

Figure 5.11.: Spectral acceptance of the TGU for 120 MeV in the x-x' phase space. The line shown is the contour line for the accepted phase space volume with the condition of a bandwidth of the emitted spectra of 0.5 %. (Data from [Bernhard et al., 2016]).

500 electrons. Comparing these two plots for $\delta = 0.5\,\%$ in Fig. 5.10a the spectrum of the central energy is almost unchanged: The maximum decreases for 7 % and the spectral width increases slightly. For the higher energy $E_0(1+\delta)$ the spectrum of the uncorrected and the corrected case have a large spectral width, which is hardly changed by the sextupoles. In contrast the spectrum of the lower energy is improved by the chromatic correction.

To explain the differences in the correction for the minimum and the maximum energy the spectral acceptance of the TGU has to be considered (see appendix C.4 for details). In Fig. 5.11 the spectral acceptance for a spectrum with a radiation bandwidth of 0.5 % or less is shown. The phase space profile of the subbunches with the lower energy shows a large overlap with the spectral acceptance of the TGU, while the higher energy only has a small overlap. For the latter the chromatic correction was not efficient. As a consequence the spectrum emitted by the subbunch with the higher energy has a large width and a low peak value.

For an energy spread of $\delta = 1.0\,\%$ the spectra are shown in Fig. 5.10b. They have a broad distribution for the uncorrected configuration and do not show a clear peak. Apart from that the results are similar to the previously discussed case of $\delta = 0.5\,\%$: The spectrum of the lower energies is partly corrected by the sextupoles, while the spectrum of the subbunch with the higher energy is almost unchanged. Again the better chromatic correction for the fraction of the bunch with the energies below the central energy is the reason for that.

In the third plot for the both cases in Fig. 5.10 a comparison of a bunch with Gaussian energy distribution with the width $\sigma_\delta = \delta$ is shown. The spectral width $\Delta\lambda/\lambda$ is 1.5 % for the uncorrected and 1.6 % for the corrected case in Fig. 5.10a and 1.7 % for the uncor-

rected and 1.9 % for the corrected case in Fig. 5.10b. For both cases the spectral width of the uncorrected spectrum is slightly smaller and the peak is slightly higher. It was expected from the calculation of the single spectra that the chromatic correction leads to a narrower spectrum. The spectra of one of monoenergetic subbunch was significantly improved, while the spectrum the second was unchanged. Therefore an improvement of the total spectrum was expected.

It might have two reasons that there is no improvement of the spectra with the chromatic correction: First, the peaks of the single spectra do not have the same central wavelength, because their entrance position at the TGU was not optimized. The average position and angle of the beam shown in Fig. 5.9 already indicate that the center of the beam is shifted by the distortion of the beam profile due to the chromatic aberration of the quadrupoles and the geometric aberration caused by the sextupoles. That leads to a broadening of the total spectrum.

A second reason is that with the Gaussian shape of the energy distribution the central energies contribute most to the spectrum, while the parts of the bunch around the energy $-\delta$, which are improved by the chromatic correction, only have a small contribution to the total spectrum. Therefore the slight deterioration will lead to a slight drop of the peak value of the total spectrum.

The simulations show, that the chromatic correction might improve the radiation properties for parts of the energy range of the bunch. However, the lack of a good criterion for the optimization of the chromatic correction is evident from the results. The spectral acceptance of the TGU seems to be an option for such a criterion: With the acceptance it is not necessary any more to determine the Twiss parameters from the electron distribution and compare them to the bunch parameters of an idealized Gaussian distribution. For the optimization simply the number of electrons in the accepted phase space volume can be determined and maximized with an adaption of the sextupole components. Such an optimization can lead to an improved chromatic correction and therefore narrower spectra.

5.3. Linear Beam Transport System with Reduced Length

For the first experimental test at the LWFA in Jena the beam transport system needs to be adapted to the condition in the laboratory. The resulting modified transport system is shortened to a length of 3.5 m and the central energy is shifted to 80 MeV[h]. The

[h] The central energy is shifted from 120 MeV to 80 MeV. That is necessary to shift the central wavelength of the undulator radiation to the spectral range of the spectrometer used for the radiation diagnostics.

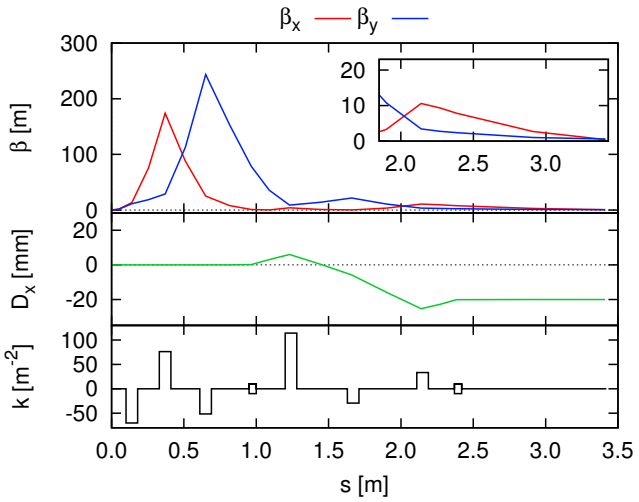

Figure 5.12.: Linear layout of the beam transport system for the first experimental test at the LWFA in Jena: The system is shortened to a total length of 3.5 m. The central electron energy is set to 80 MeV. The β-functions, the dispersion function and the k-values of the quadrupoles are plotted. The deflection angle of the dipoles is 24.4 mrad.

setup of the beam transport system is installed inside four vacuum boxes. The magnet positions are changes slightly ensuring that the magnets are not placed near a connection between these boxes. For the first test a linear system is chosen. That means no sextupoles or combined function magnets are employed.

For shortening the layout triplet 2 was removed. The dispersion function is matched by changing the polarity of the dipoles and adapting the dipole strength. The resulting deflection angle is -35.0 mrad. The beam functions and the layout of the quadrupoles are shown in Fig. 5.12.

Compared to the setup presented in the last sections the degrees of freedom in the system are reduced with the reduced number of quadrupoles, but it is still possible to match the target parameters at the entrance of the TGU. In the shortened configuration the strength of some quadrupoles is increased to values for k larger than 100 m^{-2}, which is larger than the upper limit of the strength. In this particular case that is not a problem. With the reduction of the central energy the available range for k is increased from $k_{max} = \pm 80\,\mathrm{m}^{-2}$ for central energy of 120 MeV to $k_{max} = \pm 120\,\mathrm{m}^{-2}$ for the central energy of 80 MeV.

The resulting configuration of the linear beam transport system is shown in Fig. 5.12. It is used for first experiments at the LWFA in Jena.

5.4. Conclusion

The beam transport system presented in this chapter matches the required linear parameters at the TGU. It consists of a triplet which collimates the bunches from the LWFA and a dispersive section which is required for the implementation of the chromatic correction. Estimations show that the linear layout keeps the bunch length ultra-short. Furthermore CSR effects have a minor influence on the bunches for the bunch charge expected in the experiments.

With the integration of sextupoles the chromatic error of the beam transport system cannot be corrected with the source parameters of the LWFA taken as initial parameters for the beam transport system. Moreover the geometric aberration of the sextupoles causes a strong distortion of the phase space profiles. It was shown that the chromatic correction is more effective with a slight variation of the initial parameters. Therefore the divergence and the source size were reduced to values that are in the available parameter range of LWFAs. With these source parameters the chromatic error can be corrected to obtain reasonable radiation spectra of the TGU up to an energy bandwidth of $\delta = 0.5\,\%$, which corresponds to $\Delta E / E_0 = 1.1\,\%$ (FWMH).

The optimization of the chromatic correction was limited for two reasons: First, it was not possible to define a good criterion in terms of the Twiss parameters, which were statistically determined from the phase space distributions. Second, it was not possible to correct the spectral part of the bunch with energies higher than the central electron energy.

Both problems could be solved for future optimization: For the optimization the acceptance of the TGU, which was determined recently [Bernhard et al., 2016], can be considered. For the optimization therefore the number of particles in this phase space volume accepted by the TGU can be maximized as clear criterion. To be able to correct also the part of the bunch with electron energies higher than the central energy, it might be necessary to start with a phase space distribution for the central energy, which is rotated towards the direction that can be corrected.

An aspect that is neglected in these studies is the real longitudinal shape of the magnetic field. The simulations were performed with idealized rectangular fields for the quadrupoles and sextupoles neglecting the fringe fields and field errors. However, this fact has a minor influence on the beam dynamics. With a good field quality of the magnets the offset caused by the fringe field can be corrected with an adaption of the magnet strengths.

6. First Experimental Tests of the Beam Transport System

In the first experiment it is to be demonstrated that the beams generated by the LWFA can be guided and match the beam parameters at the exit of the beam transport system e.g. to the parameters required by the TGU. Therefore several components designed and built for the setup such as the in-vacuum quadrupoles including the control of their power supplies, the temperature control and the mounting and eventually a procedure for aligning the magnets were tested.

We decided to start with a linear system, i.e. with a system that consists only of dipoles for deflection and quadrupoles for focusing. That gives the opportunity to perform various tests without the influence of a nonlinear component in the beam optics: aligning the quadrupoles with the beam, finding the limits of the diagnostics and shaping the beam with different magnet configurations.

As one consequence of the choice of a linear system the setup does not include any chromatic correction, thus only the electrons in a small energy range can be guided. Hence, the working principle of the TGU could not be demonstrated in such a way that the electrons in the energy range of 120 MeV $\pm$ 10 % are sent through the TGU and radiate at the same wavelength. Still, there is the possibility to demonstrate the working principle with a linear setup by scanning the energy range, i.e. using the chicane without chromatic correction as an energy filter and focusing different central electron energies to the TGU with the required parameters. With this technique the limited chromatic acceptance of the beam transport system and the limitations of the performance of the TGU are decoupled.

Unfortunately during the experiments the energy of the electrons was limited to the range of 20 MeV to 70 MeV due to a damaged component in the laser system and, as a consequence, a slightly deteriorated laser beam profile. For the tests of the beam transport system that is of minor interest. In contrast it allows a wide, more flexible range of the quadrupoles strength k during operation[a]. Due to a damaged current lead

[a] The quadrupole strength k scales anti-proportional to the electron energy.

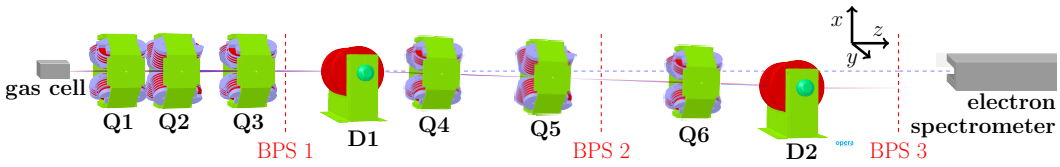

Figure 6.1.: Sketch of the experimental setup: The gas cell of the LWFA with the beam transport system and the electron spectrometer. The beam transport system consists of a triplet and a dispersive section with two oppositely poled dipoles and a second triplet. The pictures of the magnets are generated with OPERA (courtesy A. Bernhard).

of the cryostat the TGU was not available for this measurement campaign. That means there was no adaption of the magnetic field of the TGU and the radiation diagnostics to the electron energy necessary.

6.1. Parameters of the Experimental Setup

The experimental setup consisted of the LWFA with a gas cell as target, the beam transport system with two dipoles and six quadrupoles, a scintillating screen for measuring the beam profile and an electron spectrometer. The conceptual design of the single components is summarized in chapter 3. A sketch of the experimental setup is shown in Fig. 6.1. For the layout of the magnet configuration the simple system with the possibility of chromatic correction as described in section 5.3 was chosen. In the following paragraphs the parameters that were achieved for the components of the setup during the measurement campaign are summarized.

6.1.1. The Laser System and the LWFA

The laser pulse had a pulse length of 28 fs and a pulse energy of 1.0 J to 1.2 J before compression. It was focused by a $f/12$ off-axis parabola to a spot size of 120 µm^2 (FWHM). That results in a peak intensity of $I_L = 9.1 \times 10^{18}\,\mathrm{W/cm^2}$.

As plasma target a gas cell of 3.0 mm length was used filled with a gas mixture of 95 % helium and 5 % nitrogen. The gas volume was confined by two cylinders with an aperture of a diameter of 1.0 mm at the entrance and 0.8 mm at the exit. A picture of the gas cell is shown in Fig. 6.2a.

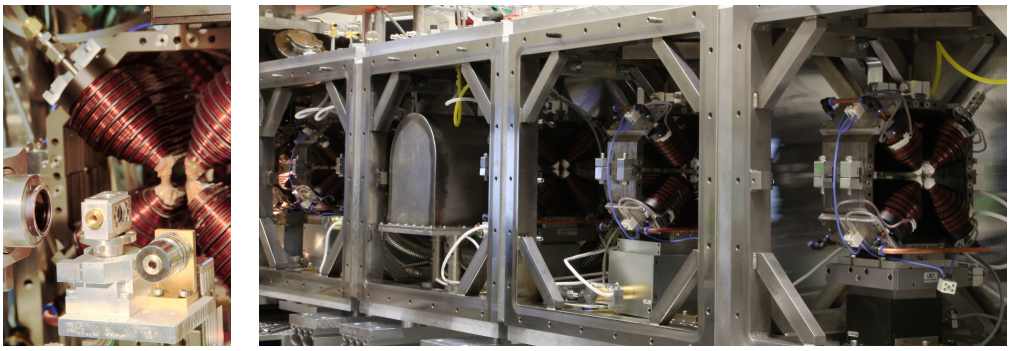

(a) Gas Cell (b) Magnets in the Vacuum Chamber

Figure 6.2.: (a) Gas cell (center) with the objective lens to observe the focus (right) in front of the first quadrupole (courtesy Jens Polz); (b) quadrupoles and dipole in the vacuum chamber.

6.1.2. Mounting and Operation of the Magnets

The beam transport system was set up inside a vacuum chamber consisting of four connected vacuum boxes as shown in Fig. 6.2b. The pressure inside the vacuum chamber was in the range of 1×10^{-4} mbar to 5×10^{-3} mbar during the operation of the LWFA. The magnets were installed in these vacuum boxes except the first quadrupole, which was placed as close as possible to the target inside the target chamber of the LWFA.

As the electron energy during the experiments was far below the design value of 120 MeV and thus the magnets were not operated at the maximum current, the distribution of the strong and weak quadrupole types I and II was not of importance. The quadrupoles type I with a slightly larger frame were used as Q2 and Q5. All quadrupoles were mounted on motorized linear translation stages with a travel length of 20 mm for alignment in the vertical direction x.[b] Q1, Q3, Q4 and Q6 had an additional translation stage with a travel length of 40 mm for alignment in the horizontal direction y. The center of Q2 and Q5 would have been located above the beam axis with the additional translation stage. That means the horizontal translation stage could not be installed for these two quadrupoles.

The dipoles inside their air chamber are mounted at a fixed height, thus only the horizontal position can be aligned by moving them on the boards.

Sketches with the positions of all magnets for different configurations during the experiments are given in appendix D.1.

[b] Note again that the deflection plane is the vertical plane in this setup.

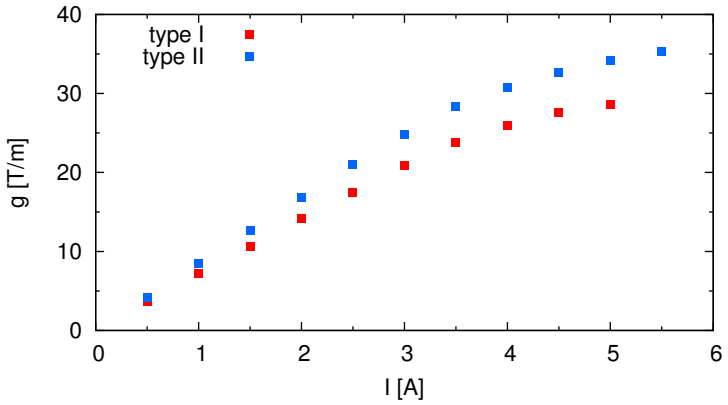

Figure 6.3.: Measured gradient at the center of the two quadrupole types for different currents. The field to determine the gradient is measured on the vertical axis at the center of the magnet.

Calibration Curve for the Field Strength For all quadrupoles the field on the vertical axis at the longitudinal center of the magnet was measured with a hall probe attached to a linear translation stage. The relative position of the measured points was determined with the micrometer head of the stage. The gradient for different currents is calculated from the measured field curve. In Fig. 6.3 the current dependent gradient for one exemplary quadrupole of each type is shown. The measured values correspond to the maximum field at the center.

For the control of the focusing strength of the quadrupoles during the experiment it was necessary to adapt the assumption of a rectangular field for the simulations of the beam transport system in MAD-X and *elegant* to the real field data with fringe fields. As no measured data was available for the gradient along the longitudinal axis, the maximum gradient of the simulated model at the center of the magnet was rescaled to the measured value.

To set the integral of the rescaled simulated field along the magnet equal to the integral of the rectangular field, the gradient along the longitudinal axis of the field model was determined with OPERA. From the comparison of the two integrals, the one of the rectangular field and the one of the rescaled simulated field, a scaling factor was determined, which was used in the control system to set the focusing strength to the required value. That means the quadrupole strength k that was chosen in the control system corresponded the maximum value of the rectangular field and the current necessary to achieve the same integrated gradient was set on the power supply. An example for this rescaling is given in appendix D.2.

The field data of the dipoles, which was necessary to determine the deflection angle, was taken from previously performed measurements [Koppenhoefer, 2013]. To determine the scaling factor for these magnets the same procedure used for the quadrupoles with the simulated data from the OPERA model was applied. The pole length of the dipoles, hence, the length of the effective field is 50 mm.

A list of the parameters of the magnets, a curve of the gradient measured at the center for all quadrupoles and a comparison of the simulated field along the longitudinal axis to the rectangular field assumed for the measurements is in appendix D.2.

Temperature During Operation During operation the temperature of the quadrupoles stayed far below the temperature limits implemented to prevent heat damages. A long term test of a sextupole, i.e. a magnet with the same coils used in the small quadrupoles, already showed that the temperature does not reach these high values predicted by the simulations. The maximum temperature measured was 30 °C while operating the sextupole in vacuum for almost two hours at 5.0 A (see appendix D.2 for the data), whereas the simulations predicted 64 °C [Werner, 2013].[c] The discrepancy is caused by the conservative values assumed in the simulation for the heat transport inside the wire bundle, along the wires and to the iron yoke.

Based on the data of the temperature test, the magnets can safely be operated in vacuum.

6.1.3. Diagnostics for Measuring the Bunch Parameters

It was decided to use the diagnostics available at in the LWFA laboratory as they could be easily integrated into in the setup of the beam transport system.

For measuring the beam profile of the electron bunches the beam profile screen (BPS) described in section 3.2.1 was placed into the beam path at three different positions along the beam transport system: close to the third quadrupole 0.7 m from the gas cell, after the fifth quadrupole at 1.8 m and at the end of the vacuum boxes, where the cryostat of the TGU would have be placed, at 2.9 m from the gas cell. The positions are marked in Fig. 6.1. The pixel size, which also limited the resolution of the screen, was 55.99 µm for the first screen position, 55.76 µm for the second and 46.86 µm for the last screen position. The camera is a 14-bit CCD-camera, i.e. it had a large dynamical range appropriate for the measurement of the bunch profile.

[c] For the simulation the temperature of the cooling water was set to 20 °C, during the measurements it was 16 °C. However, this fact alone cannot explain the discrepancy.

The position of the beam axis was marked on the screen[d]. Therefore the direction of propagation of the electrons could be overlapped with it. Unfortunately only one scintillating screen was available during the measurements. Hence, the transverse position of the electron bunch could be determined, but not the propagation angle of the bunch with respect to the design beam axis.

The second diagnostic tool for the electron bunches, the high resolution electron spectrometer for measuring the energetic distribution of the electrons, was installed at a distance of about 3.3 m from the gas cell as shown in Fig. 6.1. During this measurement campaign the energy range up to 150 MeV was captured with two CCD-cameras to be able to adjust the energy to the aimed values around 80 MeV. Unfortunately this range was not reached.

The slit aperture at the entrance of the spectrometer was completely opened. The entrance aperture was 20 mm in y and 10 mm in x. Due to the large distance from the source to the spectrometer the acceptance angle was in the range of one milliradian.

6.2. Parameters of the Unfocused Beam

The parameters of the unfocused electron beam are determined by analysing about 200 beam profiles of single bunches captured on the beam profile screen at the first position 0.706 m from the gas cell (see Fig. 6.1). The beam profiles of the single bunches were not stable. The shape of the profile changed from bunch to bunch and the position of the center of the profile showed large fluctuations caused by the problems with the laser system. In contrast the averaged beam profile from a number of single profiles was reproducible and stable, but the averaged divergence was larger than the divergence of the single bunches.

The evaluation of the initial beam parameters was done by A. Saevert [Saevert, 2015]. An ellipse was fitted to each profile and the position of the center of the ellipse and its diameter considering the full width at half maximum (FWHM) were determined. It turned out that on about 20 of the pictures there was not enough charge or the charge had a diffuse distribution. These bunches were not considered for the evaluation.

In Fig. 6.4a the averaged beam profile with a projection on each axis is shown. The shadow on the left and the right is caused by the second quadrupole that was already installed in the vacuum chamber. The divergence calculated from the averaged image and the distance to the source is 9.5 mrad (FWHM) in horizontal and 10.6 mrad

[d] The beam axis was defined along the vacuum boxes such that it passes the boxes in horizontal direction in the center and in vertical direction at the height of the gas cell.

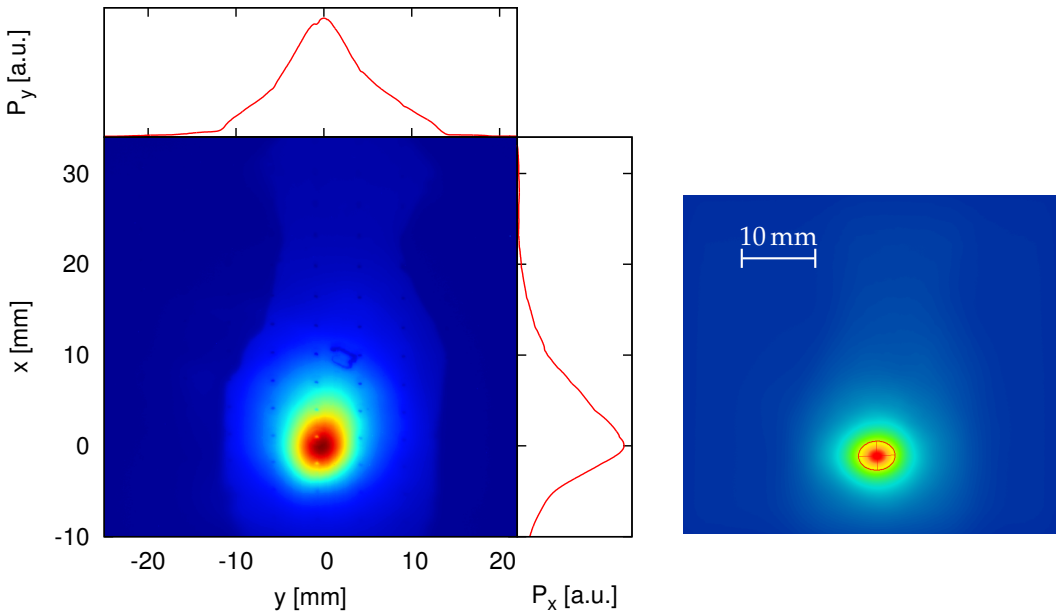

(a) Averaged Beam Profile (b) Profiles with Overlapped Center

Figure 6.4.: (a) Averaged beam profile of about 180 single bunches on the beam profile screen at the first position; (b) averaged beam profiles with the center of the bunches shifted on top of each other [Saevert, 2015] (coutesy A. Saevert).

(FWHM) in vertical direction.

As shown by A. Saevert the large values were caused by the instability of the pointing of the bunches, i.e. the propagation direction of each single bunch. The center of the bunches was spread over 2.4 mrad (rms) in horizontal and 4.2 mrad (rms) in vertical direction. The pointing stability in the vertical direction was worse than in the horizontal direction and causes the ellipticity of the averaged beam profile in the vertical direction. In Fig. 6.4b the averaged beam profile is shown with the bunch centers shifted on top of each other. This profile has the typical elliptical shape with a larger divergence along the laser polarization, i.e. in horizontal direction. The significant difference between the two beam profiles points out the large influence of the instable pointing.

The value of the divergence of the bunches during the measurements was larger than the values assumed for the simulations. For the linear quadrupole system, such a divergence might be tolerable. In contrast the sextupole correction would not work efficiently with a source divergence of some milliradians. The test of the alignment and the focusing with the system could be performed with the available beam parameters using the stable averaged beam profiles for the analysis. However, for future measurements

a more stable beam is required. With the replacement of the damaged laser component improved source parameters can be expected.

6.3. Alignment of the Magnets

For the mechanical alignment two pinholes were attached to each quadrupole, one at the entrance and one at the exit. The quadrupole was shifted and rotated such that the alignment laser, which marked the beam axis, overlapped with the pinholes. For the inclined quadrupoles the offset of the pinholes to the alignment laser was determined and the magnets were aligned to this offset. After the magnet was fixed on its stage, the longitudinal position along the beam axis was determined[e] and the quadrupole was aligned with the beam as described in the following paragraphs.

The dipoles were aligned with the air boxes they were mounted in. The height of the first dipole is given by the height of the beam in the target chamber, the height of the second corresponds to the beam axis along the TGU. In x direction the alignment tolerance is quite large with some millimeters as the pole width of the dipoles and the plateau of the field is in the order of some ten millimeters. The accuracy of installing the dipoles on posts with fix height was sufficient. In horizontal direction the slit for the beam in the air chamber was centered with respect to the alignment laser. The strength of the dipole was set by measuring the deflection angle of the beam with one of the BPSs.

6.3.1. Beam Based Alignment of the Quadrupoles

For the beam based alignment of the quadrupoles in vacuum the electron bunches were focused in one plane by the quadrupole to be aligned. The quadrupoles strength was chosen such that a line focus could be observed on the BPS. In several iterations the quadrupole was moved with the motorized stage until the position of the line focus matched the beam axis. Due to the instable bunch parameters averaged beam profiles were used for this procedure.

In Fig. 6.5 a series of averaged beam profiles of the alignment of the first quadrupole Q1 in the vertical direction is shown. The beam axis is located at the origin of the coordinate system. In the first iteration a line below the beam axis on the screen is observed. That means the center of the quadrupole is below the beam axis. The bunches

[e] As several optics were tested for different electron energies the longitudinal position could be adapted in the calculation in contrast to the usual procedure of having a distinct longitudinal position.

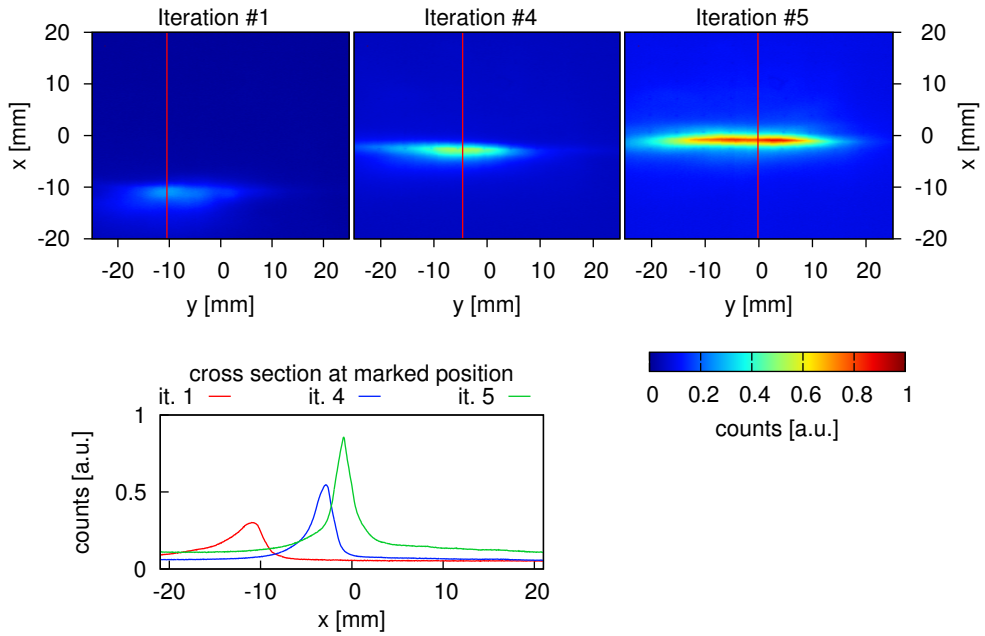

Figure 6.5.: Averaged profiles of the alignment of Q1 in vertical direction: The quadrupole focuses the bunch in the vertical plan. In several iteration the quadrupole is aligned till the beam position matches the beam axis, which is located at the origin of the coordinate system. At the bottom the counts along a vertical line in the averages images are shown.

pass a field higher than in a quadrupole aligned to the beam axis and are deflected too strong downwards. The quadrupole was moved upwards. After the fourth iteration (second beam profile) the line focus almost matches the position of the beam axis. The intensity of the beam profile increases, but the profile is still asymmetric. After five iteration the line focus seems to be symmetric and matched to the beam axis in the image. The alignment was stopped at this point and this alignment procedure was repeated for the second transverse plane.

The analysis of the cross section shows that the profile is not completely symmetric and still slightly too low, which could have been corrected with further iterations. The analysis of the averaged beam profiles during the measurements should be improved for the next experiment.

The second quadrupole was aligned with the same alignment procedure. For all further quadrupoles the beam diameter of unfocused beam of the LWFA would have been too large at their entrance and only a small fraction of the beam could have been used for alignment. Hence, the beams were focused by the first doublet or triplet and the alignment procedure was performed with the focused beam. As a consequence

the alignment errors of the first triplet were partly compensated with the following quadrupoles. Note that for Q_2 and Q_5 there was no possibility for an alignment in the horizontal direction due to the lack of the second motorized stage.

We could show that the quadrupoles can be aligned with the electron bunches despite the fluctuations of the profiles from bunch to bunch. Using the stable averaged beam profiles the line focus could be matched to the beam axis for each quadrupole. However, Fig. 6.5 shows that a careful analysis of the profiles is required to overlap the peak position with the position of the beam axis and to get a symmetric cross section. In the next subsection the resolution limit for this alignment procedure will be estimated.

One drawback of the alignment procedure used during this measurement campaign is the lack of a second screen. With one screen only the transverse position of the line focus, but not the angle of incidence can be measured. It is therefore not clear if the beam just strikes the screen at the correct position or if it is aligned properly to the axis.

A second problem during the measurement was the determination of the position of the beam axis on the BPS. The calibration had to be done at air by removing the back of the screening of the BPS, while the alignment was performed in vacuum. Thus there might have been an offset.

For future measurements some aspects should be considered: An alignment in both transverse directions should be foreseen for all quadrupoles. A second BPS should be implemented, which can be placed easily in the beam path to determine the incidence angle of the bunches. A real time analysis of the beam profiles including the analysis of the cross section with respect to the mean value, the width and the skewness of the profile for a precise adjustment of each quadrupole should be added to the control system. Furthermore one should think of alternative methods to mark the beam axis, e.g. by using structures causing a shadow in the electron beam profile for the alignment.

6.3.2. Estimation of the Limits for the Alignment

In the example shown in Fig. 6.5 the transverse offset of the peak of the profile to the beam axis is around 1 mm. The distance from the BPS to the quadrupole is 0.48 m. Thus the beam leaves the quadrupole with an angle mismatch of around 2 mrad, which is quite large. The analysis of the profiles shows that with the available diagnostics a better alignment can be achieved.

The minimum transverse offset of a quadrupole that can be resolved with the diagnostics for the alignment is determined by the deflection angle α_d of the beam to the beam axis caused by the misalignment. This propagation angle α_d has to be compared

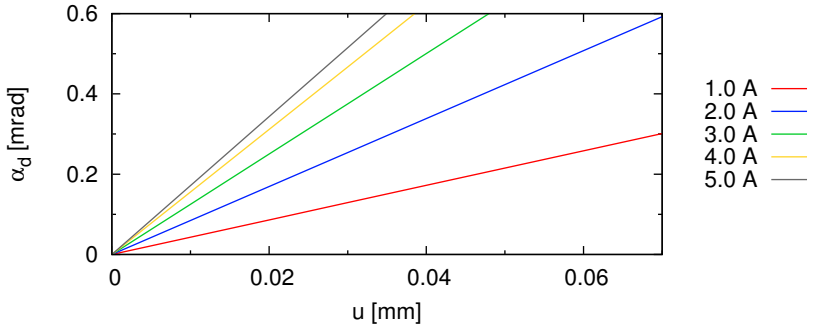

Figure 6.6.: Absolute value of the deflection angle α_d for an electron ($E_0 = 40\,\text{MeV}$) passing a quadrupole of length 80 mm at the transverse position u. α_d is calculated with equation 2.36 for the measured gradient of quadrupole QK3 for different operation currents.

to the minimum angle φ that can be resolved with the BPS.

The transverse offset of the quadrupole causes a deflection of the beam by the angle α_d dependent on the transverse position the beam passes the quadrupole. For a quadrupole of length l and with gradient g the deflection angle α_d for an electron passing the magnet at the transverse position u[f] is given by

$$\alpha_d = -\frac{eg}{E_0} l u. \tag{6.1}$$

The negative sign just indicates that the particle is deflected towards the beam axis, i.e. only the case of a focusing quadrupole as used for the alignment is considered here. Figure 6.6 shows the absolute value of the deflection angle α_d for one quadrupole of type II[g] at different operation currents.

The minimum deflection angle φ that can be resolved with the BPS can be determined from the resolution of the BPS and the distance of the quadrupole to the BPS with a simple triangular relation. The resolution of the scintillation screen is limited by the pixels of the camera. The pixel size during the measurements was 0.055 mm. The measured profiles near the optimum of the alignment have a sharp peak. With the peak position, a minimization of the width and the skewness of the profile the accuracy of the position on the screen is assumed to be two pixels in each direction.

In Tab. 6.1 the distance to the three beam profile screens for each quadrupole and the according minimum angle φ, which can be resolved with an accuracy of two pixels on the BPS, are listed. As expected the limit of the resolution is higher for larger distances

[f] u stands here again for one the transverse directions x or y.
[g] The measured data of QK3 was used.

	BPS 1		BPS 2		BPS 3	
	d in mm	φ in mrad	d in mm	φ in mrad	d in mm	φ in mrad
Q1	488	0.246	1611	0.068	2681	0.041
Q2	291	0.378	1414	0.078	2484	0.044
Q3	-	-	1128	0.098	2198	0.050
Q4	-	-	483	0.228	1553	0.071
Q5	-	-	-	-	1179	0.093
Q6	-	-	-	-	710	0.155

Table 6.1.: Distance d for each quadrupole to the three positions of the beam profile screen (BPS) according to Fig. 6.1 with the resulting angular limit φ for the alignment. As accuracy for the alignment on the screen two pixels is assumed. If no values are given, the quadrupole is placed after the according BPS.

from the magnet to the screen. On BPS 3 for almost all magnets an angular resolution better than 0.1 mrad can be achieved with the configuration used in the measurements.

Comparing the values of φ from Tab. 6.1 to the curves in Fig. 6.6 gives the limit for alignment of each quadrupole. Assuming an angular resolution of 0.1 mrad the accuracy of the positioning is in the range of 0.005 mm to 0.012 mm except for weak focusing at a current of 1 A.

The resolution depends on the configuration of the magnets, i.e. the focusing strength of each quadrupole necessary to have a line focus on the BPS used for the alignment. Therefore no general resolution limit can be given. However, from the estimations one can conclude that the accuracy of the alignment procedure applied during the measurements is sufficient. The motorized stages provide a small step width, which is far below the step width that is necessary for a proper alignment.[h] For a smooth alignment in future measurements one could think of first aligning the beam with a screen close to the magnet. In a second step one can use a screen at larger distance and with a better resolution for the final alignment and for checking if there is an angular mismatch with the beam axis.

6.4. Profiles and Spectra of the Focused Beam

For several magnet configurations beam profiles and the spectral distribution of the electron bunches were measured. The positions of the beam profile screens (BPS) and the spectrometer are shown in Fig. 6.1. Again, the averaged images are analysed here.

[h] Around 30 000 steps are necessary to move the stage for 1 mm.

6.4.1. Measuring the Energy Distribution

For measuring the energy distribution of the electron bunches, it was necessary to focus the beams into the spectrometer. The distance from the source to the spectrometer was too large to get a signal with unfocused beams[i]. We used three different configurations of the first quadrupole triplet to focus energy bands to the spectrometer screen. The quadrupole strengths k were adapted to each energy and the slightly changed travel length inside the spectrometer. $\beta_{x,y}$ and the magnet strength for the three different configurations are given in appendix D.3. The spectra are averaged over a set of at least 50 single bunches.

The data of the spectrometer were evaluated by M. Leier [Leier, 2015]. In Fig. 6.7a the results are shown. The maxima of the measured spectra are at 35.6 MeV for the first curve, 54.2 MeV for the second and 73.6 MeV for the third curve if the small peak of the latter is considered as a signal.

These values differ from the energies E_0 the optics are optimized for, i.e. 26 MeV, 40 MeV and 60 MeV. In Fig. 6.7b the value of $\beta_{x,y}$ on the screen for the three optics configuration is given. The gradient of the quadrupoles is kept constant, which means that the focusing changes with the energy. The resulting values for $\beta_{x,y}$ are calculated in steps of 1 MeV for several electron energies. The curves in x show a broad and a narrow minimum, the curve in y has only a narrow minimum at the energy E_0. As a consequence the signal measured for a certain energy band in the spectrometer should drop fast for all energies the optics are not optimized for. That can be observed in the measured curves. Even if the maximum of the energy distribution of the bunches is not equal to the central energy E_0 of the optics, one would expect the maximum of the measured curve in the range of E_0.

There are two possible reasons for this offset in the measured energy: First, the calibration of the spectrometer might not be correct. For the setup the direction of the deflection and therefore the position of the magnet had to be changed. There might be an error in the new calibration of the spectrometer. Second, the calibration factor of the magnets could be wrong. I assumed that the shape of the fields of the quadrupoles is the same as in the simulations. If that is not the case, a constant ratio of the real field integral and the values used in the experiment would also lead to an energy shift in the optics. The optics would still focus the beam to the screen but for a different central energy. A field measurement of the quadrupoles and optics simulations with the real fields are planned. The results of these calculations will show what causes the offset.

[i] Usually the spectrometer is installed about 2 m from the source.

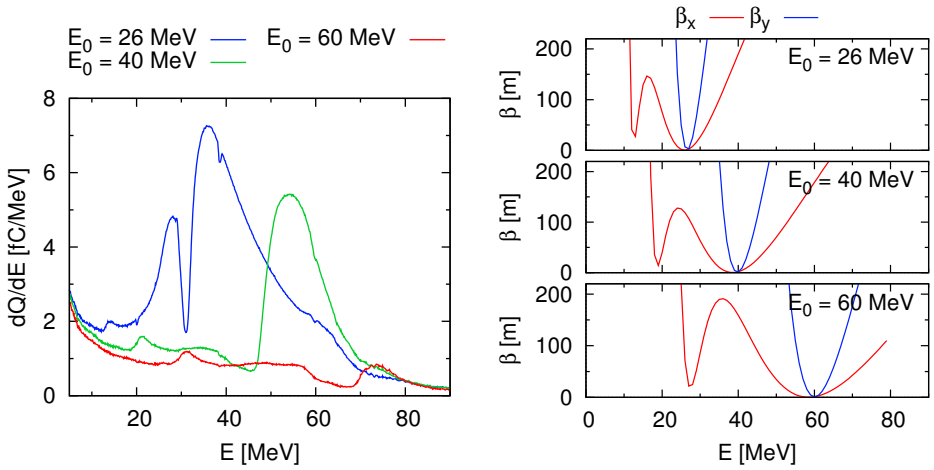

(a) Measured Spectra (b) $\beta_{x,y}$ of E

Figure 6.7.: (a) Measured spectra for three different configurations of the optics: 26 MeV, 40 MeV and 60 MeV were focused to the screen of the spectrometer. (b) $\beta_{x,y}$ evaluated at the position of the spectrometer screen for different energies with a fixed optic optimized for the energy E_0. For the curves the values are determined in intervals of 1 MeV.

The second point to mention is the dip at 30 MeV, which is observed in the spectrum optimized for 26 MeV and cannot be explained. It might be caused by some object in the beam path inside the spectrometer, where the beams are energetically dispersed.

The measured curves show that most of the electrons are in the energy range of 20 MeV to 50 MeV taking the energy values the optics were optimized for. This means, the electron energies do not reach the range of 80 MeV or above, for which it was planned to test the beam transport system. However, around 40 MeV there was enough charge for the test of different magnet configurations.

6.4.2. Focusing of the Electrons

In Fig. 6.8 the averaged beam profiles for two different magnet configurations are shown: In Fig. 6.8a the beam is focused with the triplet for a central energy of 60 MeV on BPS 2. On the right $\beta_{x,y}$ for this configuration is plotted with the position and the magnet strength of the quadrupoles. The initial values for the calculation of the beta functions with MAD-X are $\beta_{x_0,y_0} = 0.01$ m and $\alpha_{x_0,y_0} = 0$. In Fig. 6.8b the beam is deflected by the two oppositely poled dipoles with a deflection angle of 24.5 mrad. The optics focus a central energy of 40 MeV onto BPS 3. For each beam profile the projection P on both

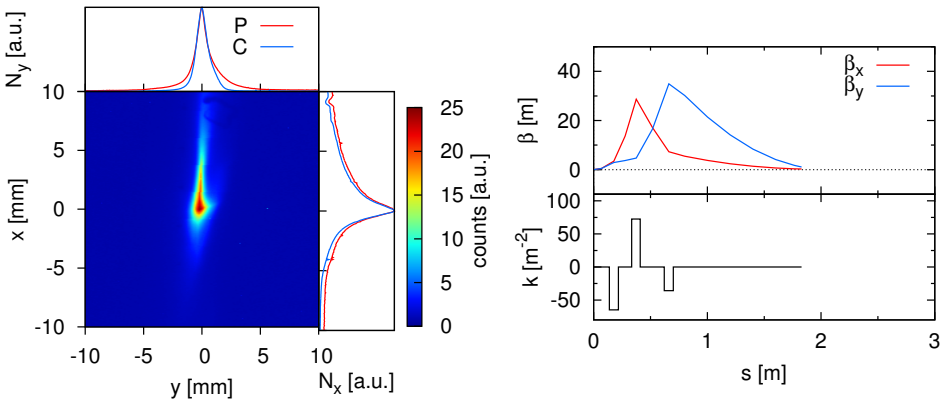

(a) Focus on BPS 2

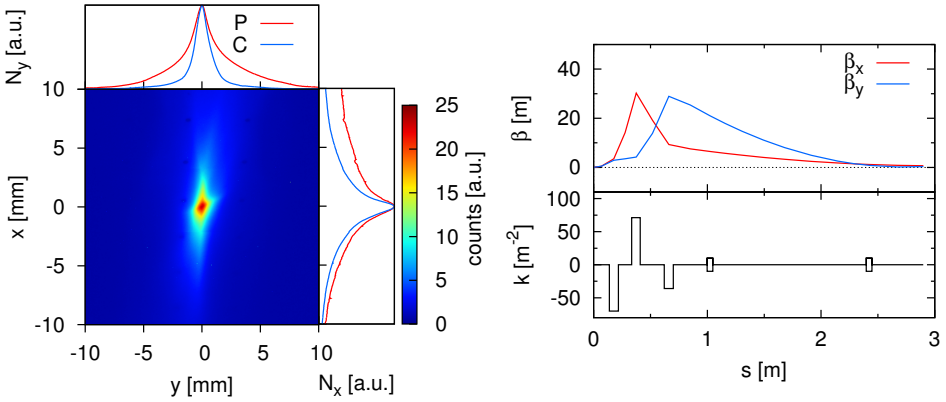

(b) Focus on BPS 3

Figure 6.8.: Measured beam profiles with the projection P on each axis and a cut C through the center. The quadrupole strength k, the position of the dipoles and $\beta_{x,y}$ are depicted for each setup with $\beta_{x_0,y_0} = 0.01$ m and $\alpha_{x_0,y_0} = 0$. (a) Focus of 60 MeV on BPS 2; (b) focus of 40 MeV on BPS 3 with a deflection angle of the dipoles of 24.5 mrad. The same color code is applied to both profiles.

axes and a cut C through the maximum is plotted. The beam size of the center along the horizontal axis is 1.11 mm (FWHM) and along the vertical axis 2.84 mm (FWHM) for the profile in 6.8a. For the profile in 6.8b the values are 1.41 mm (FWHM) and 3.09 mm (FWHM), respectively. Here the full width at half maximum is considered to minimize the influence of the background on the screen. The width along the vertical axis is larger due to the smeared profiles along this axis and the dispersion in the second plot.

The position of the screen does not exactly match the focus position.[j] For the case shown in Fig. 6.8a the beam size in the y-z-plane is still large at the position of the

[j] One of the distances was not adapted correctly in the simulations to determine the optics configuration.

screen with $\beta_y = 2.41$ m and $\alpha_y = 8.94$, which leads to a larger beam size in y. In Fig. 6.8b the screen is behind the focal position but $\beta_{x,y}$ is small in both planes with $\beta_x = 0.71$ m and $\beta_y = 0.35$ m. In both cases the measured profile does not have the circular or oval form one would expect, even if the screen was not placed exactly in the focus. The first measured profile has a clear vertical and a slight horizontal line. The second profile has a diamond-shaped center and is more symmetric.

Possible reasons for this deformation might be the energy spread of the bunches, the divergence of the source, which is significantly larger than the values used for the design of the transport system, or a misalignment of the magnets. To analyze the profiles, tracking simulations with a variation of the bunch parameters and the alignment errors of the magnets were performed with *elegant* [Borland, 2000].

Comparison with Simulated Beam Profiles For the simulation an electron bunch of 50 000 particles with a Gaussian distribution of the transverse and longitudinal particle position in the bunch and the energy distribution is generated. I adapted the values of the simulation to those of the experiments. For some parameters, i.e. the divergence and the energy spread, the values were measured, other parameters such as the source size or the alignment error have to be estimated taking into account the conditions during the experiments.

In the calculations for the layout of the beam transport system the divergence was assumed to be 1.0 mrad. The measured values were $\sigma_{x'} = 3.8$ mrad and $\sigma_{y'} = 3.4$ mrad. [k] The divergence was set from the design values to the measured values. I decided to keep the source size constant, not the emittance. Keeping the emittance constant with an increased dispersion would result in a decrease of the source size. That is not a reasonable choice as the large divergence is mainly caused by fluctuations of the propagation direction of the bunches. As a consequence one would also expect fluctuations in the movement of the electrons inside the plasma or of the plasma wave, which would result rather in an increase of the averaged source size than in a decrease. However, in this first step the possible increase of the source size is neglected. The influence of the source size on the beam profiles is considered in one of the following steps.

Figure 6.9 shows the simulated profiles for the same magnet configuration as in the measured profiles of Fig. 6.8. The bunch in the first profile has the initial parameters assumed for the calculation of the layout, i.e. $\sigma_{x',y'} = 1$ mrad, for the second profile the divergence was set to the measured values. For the third profile the energy spread is set from 0 % to 3 % with 1 mrad divergence, the fourth profile is with 3 % energy

[k] A Gaussian distribution was assumed to transform the FWHM values into σ.

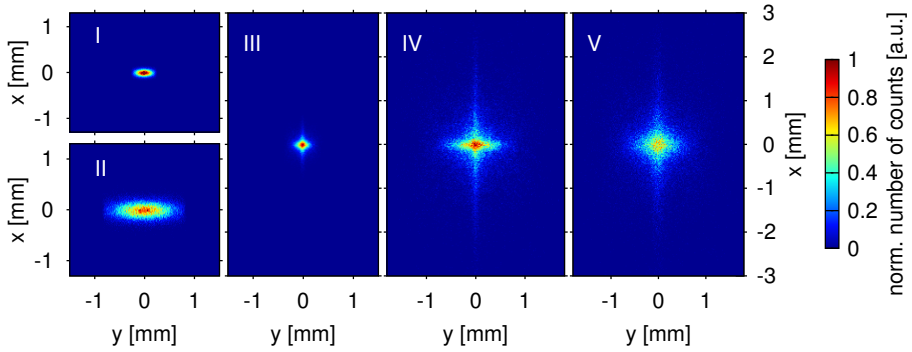

(a) Simulated Profiles: Focus on BPS 2

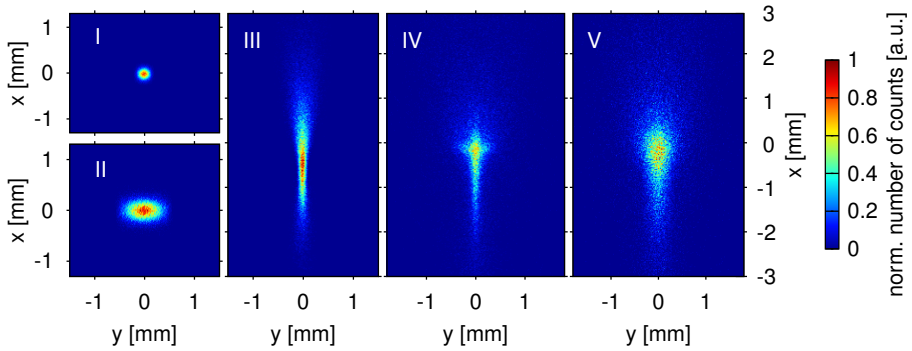

(b) Simulated Profiles: Focus on BPS 3

Figure 6.9.: Simulated beam profiles of a Gaussian electron distribution at the position of (a) BPS 2 and (b) BPS 3 for the optics shown in Fig. 6.8. For both cases (I) is the beam profile with ideal source parameters and a monoenergetic distribution, (II) with the measured divergence and a monoenergetic distribution, (III) the ideal divergence and $\sigma_\delta = 3\,\%$, (IV) the measured divergence and $\sigma_\delta = 3\,\%$ and (V) additionally a source size increased to 30 µm. The color code is scaled to each profile.

spread and the measured divergence. For the fifth profile the source size is increased from $\sigma_{x,y} = 10\,\mu\text{m}$ to 30 µm, the same ratio as the increase of the divergence from the design values to the measured ones. In Tab. 6.2 the bunch parameters for these different cases are summarized. In the simulation the energy spread could not be increased to values larger than 3 %, because the profiles almost vanish for larger energy spreads. In appendix D.4 a sequence for the increase of the energy spread and the source size is shown.

For both profiles the increase of the divergence leads to a significant increase of the beam size, as one would expect with an increased emittance and a constant $\beta_{x,y}$. In Fig. 6.9a the profile has the diamond-shaped center that is observed in the measurements. With an increase of the source size the profile is blurred and looses the substruc-

	I	II	III	IV	V
energy spread σ_δ	0 %	0 %	3 %	3 %	3 %
divergence $\sigma_{x'}$	1.0 mrad	3.8 mrad	1.0 mrad	3.8 mrad	3.8 mrad
divergence $\sigma_{y'}$	1.0 mrad	3.4 mrad	1.0 mrad	3.4 mrad	3.4 mrad
source size σ_x, σ_y	10 µm	10 µm	10 µm	10 µm	30 µm
geo. emittance ε_x	10 nmrad	38 nmrad	10 nmrad	38 nmrad	114 nmrad
geo. emittance ε_y	10 nmrad	34 nmrad	10 nmrad	34 nmrad	102 nmrad
β_x	10 mm	2.6 mm	10 mm	2.6 mm	78 mm
β_y	10 mm	2.9 mm	10 mm	2.9 mm	78 mm
α_x, α_y			0		
long. bunch size σ_s			1 µm		

Table 6.2.: List of the parameters for the initial particle distribution: The distribution is generated with the SDDSbeam-function in *elegant* and is tracked through the same magnet configuration as the one of the measurements shown in Fig. 6.9 and Fig. 6.11b.

ture. In the profiles in Fig. 6.9b additionally the energies are spread up along the x axis by the dipoles, which changes the shape of the profile, but the observations are similar to the first case. Note that the color code is scaled to the minimum and maximum of each profile. In both cases some particles are lost as they are not on the detector area of ± 3 mm around the beam axis. To simulate the finite aperture of the magnets, so-called scrapers were added directly after the magnets[1]. However, this constraint did not lead to any additional particle loss.

Comparing the simulated profiles with the measured ones the same characteristics can be found: The relatively large beam size of the profiles in horizontal direction is caused by the divergence of the source. The measured values are even in the range of the simulated ones. The vertical line is caused by the energy spread. And the increased source size smears out the profile mainly in the vertical direction. Considering also that for the simulated profiles a Gaussian bunch was used as input while the measured profile is not symmetric, even the stronger smearing to the top appears reasonable.

Case III of the simulations shows that the electron bunch could have been focused with small beam profiles without chromatic correction despite the large energy spread. With the profile in Fig. 6.9b III the emittance could have been determined using the method of the quadrupole scan [Weingartner et al., 2012]. Unfortunately the large source divergence due to the pointing instability deteriorated the beam profiles and made it impossible to determine explicit values for the emittance.

[1] *elegant* provides scrapers that can be placed from each side into the beam path to limit the aperture. Here four scrapers were used to limited the aperture to a square with the side length equal to the diameter of the magnet aperture (2 mm $\times$ 11 mm for the quadrupoles and 20 mm for the dipoles)

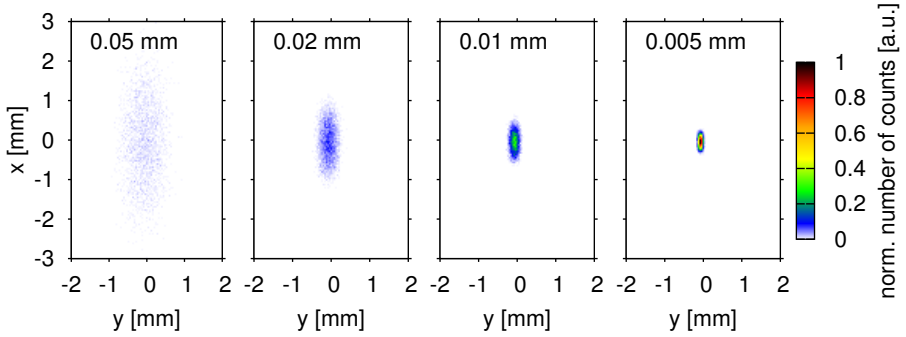

(a) Center of the Bunch

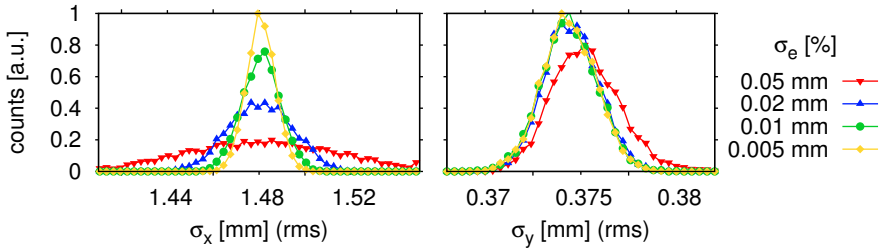

(b) rms Width of the Bunch

Figure 6.10.: Influence of alignment errors for the setup shown in Fig. 6.8b: A random error is assigned to the x and the y position of each quadrupole. The values given in the graphs are the σ_e of the Gaussian error distribution, which has a cutoff at $2\sigma_e$. (a) shows the position of the center of the bunch, (a) the rms value of the distribution along x and y.

Influence of the Alignment Errors A randomly generated error was assigned to the x and y position of each quadrupole.[m] The errors had a Gaussian distribution of width σ_e and a cutoff at $2\sigma_e$. The bunch parameters were set to the measured divergence and an energy spread of 3 % (equivalent to case IV in Tab. 6.2). 6000 runs of *elegant* were performed and the mean and the rms value of the spatial distribution in x and y were determined. In Fig. 6.10a the position of the center of the beam, which is defined here as the mean value of the distribution in x and y, is shown for different σ_e. The variation of the center is quite large though in this setup only a quadrupole triplet is used to focus the beam. Even in the case of $\sigma_e = 0.01$ mm the variation is in the range of the beam size.

In Fig. 6.10b a histogram of the rms beam size is shown for the different errors. Along y the beam size does not vary with increasing alignment errors up to a value of $\sigma_e = 0.02$ mm. For the larges error of $\sigma_e = 0.05$ mm the bunch size is slightly increased. In x the beam is dispersed at the position of BPS 3. Thus the beam size is larger along

[m] The error was generated with the "error-element" provided by *elegant*.

this direction. With increasing alignment errors the beam size varies in a large range of almost 0.1 mm towards smaller and larger beam sizes.

During the measurements the alignment errors were probably in the range of 0.5 mm to 1.0 mm, i.e. more than a factor of ten larger than the errors considered here. Therefore a strong influence of these errors on the measured bunch profiles is expected, causing an additional deformation. However, one should not forget that for measured profiles of one configuration the errors are fixed and up to a certain degree the errors of previous magnets are corrected with the alignment of the following magnet. Thus reasonable beam profiles could be achieved despite the large alignment errors.

Nevertheless for future measurements it is necessary to keep the alignment errors in the range of some hundredth of a millimeter, which can be achieved with the available diagnostics. The influence of additional error such as the tilt and the positioning error in z should also be considered and the according degrees of freedom should be implemented in the mounting.

Matching to the Parameters at the Entrance of the TGU After focusing the electron bunches with triplets and generating the required dispersion with the dipoles we tried to matched the bunches to the optimum end parameters for the TGU. Therefore three quadrupoles were added in the dispersive section.

In Fig. 6.11a the beam profile for these optics optimized for an electron energy of 40 MeV is shown. Unfortunately most of the electrons were lost before the third BPS and there was no clear profile observed on this screen.

Again, simulations were performed with the conditions of the experiment simulating the profile shown in Fig. 6.11b. The results are similar to those in the previous section: The divergence of the bunches increases the beam size (case II). For this setup with the energy spread of 3 % (case IV) and an increased source size (case V) even in the simulations there is no clear beam profile visible. Thus it is not surprising that the signal in the measurements was poor.

Adding scrapers in the simulations, which limit the aperture to a square of ± 11 mm with the beam axis in the center, 34 % of the electrons are lost for an energy spread of 5 %. Adding alignment errors in the range of $\sigma_e = 0.5$ mm to the transverse positions of the quadrupoles only in 30 % of the tracking runs in *elegant* any particles at all do pass the transport system.

Considering now these points for the interpretation of the profile, it was not very likely to have observed a good beam profile with these optics. For the setup of the complete beam transport system in future measurements the divergence of the source

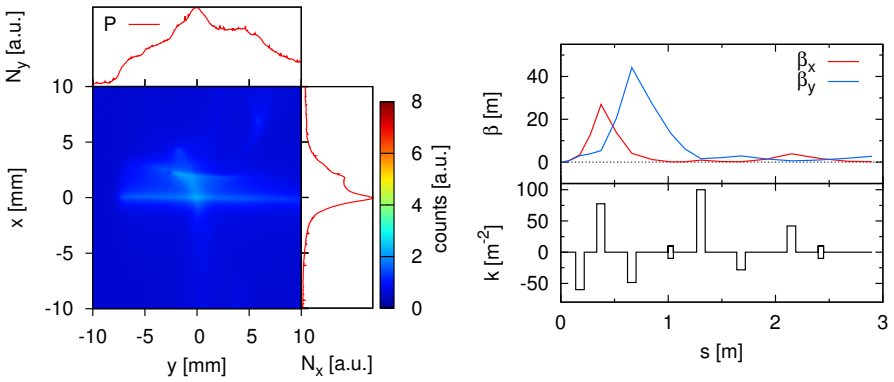

(a) Measured Profile on BPS 3

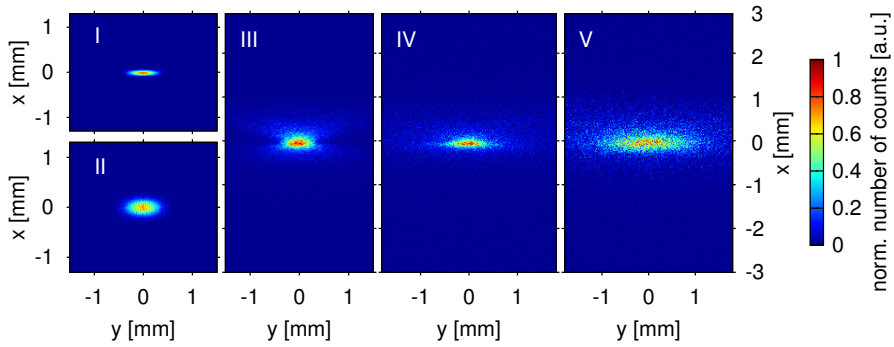

(b) Simulated Profiles on BPS 3

Figure 6.11.: (a) Measured beam profile with the projection P on each axis. The quadrupole strength k, the position of the dipoles and $\beta_{x,y}$ are depicted on the right. (b) Simulated beam profiles, where (I) is the beam profile with ideal source parameters and a monoenergetic distribution, (II) with the measured divergence and a monoenergetic distribution, (III) the ideal divergence and $\sigma_\delta = 3\,\%$, (IV) the measured divergence and $\sigma_\delta = 3\,\%$ and (V) additionally a source size increased to 30 µm. The color code is scaled to each profile.

has to be smaller and the alignment of the quadrupoles has to be done more carefully to obtain reasonable results with a beam transport system consisting of more than three quadrupoles.

6.5. Conclusion

The measurements showed that the electron beam of the LWFA can be transported and shaped with a beam transport system consisting of quadrupoles and dipoles. The alignment of the transverse quadrupole position was successfully done by focusing

the electron beam and using the motorized stages for correction. Reasonable foci were measured at different positions along the transport system. The first quadrupole triplet was used to stabilize the beam and send it to the electron spectrometer.

However, the divergence of some milliradians and the significant energy spread observed during these measurements deteriorated the measured profiles considerably. The beam profiles were further disturbed by the large alignment errors. Simulations showed that the source divergence should be reduced to 1 mrad to obtain better results with the beam transport system. The energy spread in the range of a few percent changes the shape of the beam profile, but could be tolerated for first tests of the TGU as the size of the foci stays small. Still with the linear system the accepted energy range of the TGU would have to be scanned. For future setups in which the dispersed electron bunch will be sent through the TGU emitting radiation at the same wavelength in the complete energy range the transport system has to be be chromatically corrected.

Another important aspect demonstrated in the measurements is the beam based alignment of the quadrupoles despite a poor beam quality from the LWFA. We used the fact, that the averaged beam profile was stable despite the fluctuations in the propagation direction of the single bunches. Based on these experiences the alignment possibilities can be improved in the setup and the necessary infrastructure and diagnostics can be provided for the next measurement campaign.

During the measurements we observed that the acceptance angle of the first quadrupole triplet is quite large. Therefore it stabilized the electron beam in such a way that it focused all bunches, which are in a certain angular cone considering their divergence and propagation angle, to a point on the beam axis. This fact was used e.g. to measure the spectra of the electrons. That means the triplet can be used for other experiments to offer a better signal or even to use the electrons directly for scattering.

7. Summary and Outlook

A beam transport system from a laser wakefield accelerator (LWFA) to a transverse gradient undulator (TGU) has been developed in order to realize a compact undulator radiation source. Such a radiation source might be extended to a FEL driven by the bunches of a LWFA. LWFAs provide very high accelerating gradients but the electron bunches suffer from a relative energy spread of few percent and a source divergence of some milliradian. In contrast to other approaches this work assumes these non-ideal bunch parameters of the LWFA as intrinsic. It follows the strategy of using a fraction as large as possible of the accelerated electrons in spite of their large energy spread and divergence.

To achieve that the beam transport system has to collect and collimate the bunches of the LWFA and match the required dispersion and beam parameters at the TGU for the energy range of the bunches. The dispersion and the beam parameters are adapted to the TGU to obtain the best properties of the undulator radiation, i.e. a narrow spectrum with one central wavelength for all electron energies.

An analytical description of the beam dynamics under the influence of the fields of the TGU was developed taking the transverse field gradient into account. Based on this description the optimum end parameters for the beam transport system were determined. Subsequent studies could be performed including tracking studies of the bunches in the TGU [Morcrette, 2012] and the simulation of the emitted radiation fields [Braun, 2013, Bernhard et al., 2016]. For an application of the TGU as radiation source and a possible extension of the concept to FELs such studies are essential.

A linear beam transport system was designed fulfilling the required conditions in terms of the dispersion and the Twiss parameters for the central beam energy. The divergence of the source is compensated with a quadrupole triplet and the beam functions are smoothly matched to the optimum end parameters at the TGU. It was shown that the influence of CSR effects can be neglected for the expected bunch charge despite the intrinsically ultra-short bunch length delivered by the LWFA. The configuration of the transport system with several zero-crossings of the dispersion function preserves the bunch length in the ultra-short range.

With the implementation of a correction of the chromatic error with combined quadrupole-sextupole magnets the accepted energy bandwidth of the transport system could be extended to $\Delta E/E_0 \approx 1\,\%$ (FWHM), which is already in the range of the relative energy spread of the bunches. The studies showed that a source divergence no larger than 1 mrad is required to obtain an effective correction of the system. With this chromatic correction the radiation bandwidth of the undulator radiation was reduced for the low-energetic parts of the bunch compared to an uncorrected system.

As a first step towards the realization of the transport system at the LWFA in Jena an experimental setup with a simplified linear transport system was tested. It was successfully shown that the bunches of the LWFA can be transported and shaped with the installed quadrupole system. The quadrupoles were set up subsequently and aligned with the beam of the LWFA with good accuracy despite the poor beam quality during the experiments. An improvement of the mounting base of the magnets for future measurements enabling more degrees of freedom for the alignment and the employment of a second scintillating screen for measuring the beam profile will offer a sufficient precision for the alignment.

The calculations and measurements done for this thesis were focused on the basic design and feasibility studies for the beam transport system. Further steps to include more realistic parameters are necessary: For the magnets the real shape of the fields including the fringe fields and field errors should be implemented in the simulation. For future optimizations of the sextupole correction the recently determined spectral acceptance of the TGU [Bernhard et al., 2016] can be taken as a clear criterion.

A modification of the beam transport system will be necessary for a more compact design and an application to higher electron energies. For that the triplet for the collimation could be replaced with a more compact magnetic section, e.g. with permanent magnets as proposed for the final focusing of Thomson scattered electrons at ELBE [Kraemer et al., 2014]. A different approach for the chromatic correction may be chosen, e.g. based on the concept of fixed field alternating gradient (FFAG) lattices [Machida and Fenning, 2010]. However, the general layout presented in this thesis can be kept as it provides an almost isochronous beam transport.

The setup with the TGU and the dispersive beam transport system compensates not only for the relative energy spread, but also for the jitter in the central energy of the bunches of the LWFA. It stabilizes the parameters of the emitted radiation despite fluctuations in some parameters of the LWFA and in that way provides stable conditions for the application of the radiation.

With an adaption of the end parameters of the transport system e.g. to an achro-

matic system, the advantages of the design can be transferred to different experimental applications. The realization of a stable beam transport system is an essential step towards the application of LWFAs in any field, making them a reliable tool for science and processing and taking benefit from the intrinsic properties of LWFAs such as the ultra-short bunch length and high accelerating gradients.

Appendices

A. Electron Beams in Undulators

A.1. Qualitative Treatment of Undulator Radiation

In this section two models qualitatively describing the generation of undulator radiation are given following the description in [Hofmann, 2004] and [Turner, 1998]: the interference model and the description in the reference system co-moving with the electron. These models can explain in a descriptive way some of the properties of undulator radiation.

A.1.1. The Interference Model

The interference model for the undulator radiation is one of the most intuitive models. As described before in a weak undulator an electron moves approximately with the velocity $\beta_e c$, while the emitted photons are moving with the speed of light c. It takes an electron the time $t_e = \lambda_u/\beta_e c$ to travel one period, a photon the time $t_\gamma = \lambda_u/c$. The time delay caused by the velocity difference is $\Delta t = t_\gamma - t_e$ for each undulator period.

The photons emitted by a single electron interfere constructively for the frequency that corresponds to the path difference resulting from the time delay Δt and all integer multiples of it. For an observer on the propagation axis, i.e. with the angle $\theta = 0$ to the axis, the relation for the fundamental wavelength is

$$\lambda_1(\theta = 0) = \lambda_{10} = c\Delta t = \frac{\lambda_u}{\beta_e}(1 - \beta_e) \quad \text{or} \quad \omega_{10} = \frac{2\pi c}{\lambda_u}\frac{\beta_e}{1 - \beta_e}. \tag{A.1}$$

Observing the radiation at an angle $\theta \neq 0$ the projection of the undulator period length and the projection of the electron velocity have to be considered, i.e. $\lambda_u \to \lambda_u \cos\theta$ and $\beta_e c \to \beta_e c \cos\theta$. For the observation of the radiation under the angle θ the condition for constructive interference is therefore given by

$$\lambda_m(\theta) = \frac{c\Delta t}{m} = \frac{\lambda_u}{m\beta_e}(1 - \beta_e \cos\theta) \quad \text{or} \quad m\omega_1(\theta) = \frac{2\pi c}{\lambda_u}\frac{\beta_e}{1 - \beta_e \cos\theta}, \tag{A.2}$$

where m is the number of the higher harmonics.

For an ultra-relativistic electron with $\beta_e \approx 1$ and $\gamma_e \gg 1$ equation A.2 can be rewritten as

$$\omega_1 = m\frac{2\pi c}{\lambda_u}\frac{2\gamma_e^2}{1+\gamma_e^2\theta^2} = m\frac{\omega_{10}}{1+\gamma_e^2\theta^2}. \tag{A.3}$$

In the case of a weak undulator the emitted frequency depends on the period length λ_u and the relativistic parameter γ_e of the electrons. As the excursion is neglected, the magnetic field amplitude of the undulator has no influence, which is different in the case of a strong undulator.

In the measured undulator spectrum only the odd multiplies of the fundamental frequency are observed as for the even multiples the emitted waves interfere destructively from one half period to the next.

A.1.2. Transformation from the Co-Moving Frame

Observing the motion of a electron in the undulator in the frame co-moving with the electron emphasises the influence of the relativistic electron motion on the emitted radiation.

In a weak undulator the frame of reference moves along with the electron's velocity $\beta_e c$. The undulator and its field pass the electron with the electron's velocity in the laboratory frame. The electron itself performs a pure transverse oscillation with the frequency $\Omega_u = k_u \beta_e c$ and emits the classic dipole radiation of a Hertz dipole. The frequency of the oscillation is increased by a factor of γ_e as the period length $\lambda^* = \lambda_u/\gamma_e$ is Lorentz contracted due to the motion of the undulator. Transforming the radiation back to the laboratory system, the radiation is confined in a small cone of opening angle $1/\gamma_e$. The spectrum is Doppler shifted, thus the emitted frequency depends on the observation angle θ. For an ultra-relativistic motion the emitted frequency can be approximated by

$$\omega_1 = \frac{\Omega_u}{1-\beta_e\cos\theta} \approx \frac{2\gamma_e^2\Omega_u}{1+\gamma_e^2\theta^2}. \tag{A.4}$$

The emitted radiation contains one frequency, which depends on the observation angle.

In a strong undulator the electron performs a figure-of-eight motion in a frame co-moving with the average electron velocity $\beta_e^* c$ according to the trajectory given in equation 2.43. The motion can be split in two separate directions, an oscillation along the transverse direction x with frequency $\gamma_e^*\Omega_u$ and a longitudinal oscillation in z with frequency $2\gamma_e^*\Omega_u$, again with the relativistic contraction of the undulator period length. As the motion of the electron is not linear any more, also higher harmonics of $\gamma_e^*\Omega_u$ are present. Transforming back to the laboratory frame, the frequencies can be approx-

imated by

$$\omega_m = m\frac{\Omega_u}{1-\beta_e^*\cos\theta} \approx m\frac{2\gamma_e^{*2}\Omega_u}{1+\gamma_e^{*2}\theta^2}. \tag{A.5}$$

The spectrum consists of a number of lines. In measurements on the propagation axis only odd harmonics of $\gamma_e^*\Omega_u$ are observed, what cannot be described in this model.

A.2. Equation for the Focusing in a Planar Undulator

In this section the derivation of the strength of the focusing effects in a planar undulator are described. The derivation of the equations follows the description in [Walker, 1983] and [Clarke, 2004].

The equations of motion in the transverse planes are

$$\ddot{x} = \frac{e}{\gamma m_0}\left(\dot{z}B_y - \dot{y}B_z\right) \quad \text{and} \tag{A.6}$$

$$\ddot{y} = \frac{e}{\gamma m_0}\left(\dot{x}B_z - \dot{z}B_x\right), \tag{A.7}$$

where the particle is deflected horizontally in x by the field component B_y in vertical direction. As the magnetic field is assumed to be infinite in x (no fringe fields due to an finite transverse pole width), there are no field components in this direction, i.e. $B_x = 0$. Furthermore it is assumed that the electron moves close to the mid plane of the undulator. Thus the motion in vertical direction is small and $\dot{y} \approx 0$. With that, equation A.6 can be integrated:

$$\dot{x} = \frac{e}{\gamma m_0}\int B_y dz$$

Near the propagation axis the magnetic field can be approximated linearly. Using the relation $\nabla \times \vec{B} = 0$ gives

$$B_z \simeq \frac{dB_z}{dy}y = \frac{dB_y}{dz}y.$$

Inserting all in equation A.7 and using $\frac{d^2}{dt^2} = c^2\frac{d^2}{ds^2}$ leads to a differential equation similar to Hill's equation

$$y'' - \left(\frac{e}{\gamma m_0 c}\right)^2 \int B_y dz \cdot \frac{dB_y}{dz}y = y'' + K_y(z)y = 0$$

with the focusing strength

$$K_y(z) = -\left(\frac{e}{\gamma m_0 c}\right)^2 \int B_y dz \cdot \frac{dB_y}{dz}.$$

This relation can be evaluated directly knowing the field of the insertion device. When the focal length is large compared to the period length of the undulator, which is usually the case, the averaged focusing of each period can be calculated:

$$\begin{aligned}\bar{K}_u = \frac{1}{\lambda_u}\int_0^{\lambda_u} K_y(z)dz &= -\frac{1}{\lambda_u}\int_0^{\lambda_u}\left(\frac{e}{\gamma m_0 c}\right)^2 \int B_y dz \cdot \frac{dB_y}{dz} \\ &= -\frac{1}{\lambda_u}\left(\frac{e}{\gamma m_0 c}\right)^2 \left(\left[\int B_y dz \cdot B_y\right]_0^{\lambda_u} - \int_0^{\lambda_u} B_y^2 dz\right) \\ &= \frac{1}{\lambda_u}\left(\frac{e}{\gamma m_0 c}\right)^2 \int_0^{\lambda_u} B_y^2 dz\end{aligned} \tag{A.8}$$

The condition $\int_0^{\lambda_u} B_y dz = 0$ is required for a vanishing first field integral.

For a pure sinusoidal field, the focusing parameter $\bar{K}_u$ can be determined as

$$\bar{K}_{y,s} = \frac{1}{\lambda_u}\left(\frac{eB_0}{\gamma m_0 c}\right)^2 \cdot \frac{1}{2} = \frac{1}{2\rho_0^2}. \tag{A.9}$$

A.3. Calculation of a Constant β along the Undulator

To achieve a constant β along the undulator the focusing of the undulator has to compensate the divergence of the beam.

For the plane perpendicular to the deflection plane In this plane the average focusing parameter $\bar{K}$ for a planar undulator and also the TGU - neglecting in first order the x-component of the magnetic field - is given by equation 2.49 or 2.50 for a sinusoidal field. With this parameter the focusing can be determined with the equation for a focusing quadrupole:

$$\begin{pmatrix}\beta_{\text{end}} \\ \alpha_{\text{end}} \\ \gamma_{\text{end}}\end{pmatrix} = \begin{pmatrix}\cos^2\vartheta & -\frac{2}{\sqrt{\bar{K}}}\cos\vartheta\sin\vartheta & \frac{1}{\bar{K}}\sin^2\vartheta \\ \dots & & \\ \dots & & \end{pmatrix}\begin{pmatrix}\beta_0 \\ \alpha_0 \\ \gamma_0\end{pmatrix}$$

with $\vartheta = \sqrt{\bar{K}}L$.

The conditions for a constant β along the undulator are $\beta_{\text{end}} = \beta_0$ and $\alpha_{\text{end}} = \alpha_0 = 0$. That leads to the quadratic equation

$$\beta_0 = \beta_0 \cos^2 \vartheta + \frac{1}{\bar{K}\beta_0} \sin^2 \vartheta$$

Solving this equation for β_0 leads to

$$\beta_0 = \sqrt{\frac{\sin^2 \vartheta}{\bar{K}(1 - \cos^2 \vartheta)}} = \sqrt{\frac{1}{\bar{K}}}.$$

That means for a constant focusing parameter $\bar{K}$ a constant β along the undulator is achieved for the initial conditions

$$\beta_0 = \sqrt{\frac{1}{\bar{K}}}\,, \quad \alpha_0 = 0 \quad \text{and} \quad \gamma_0 = \frac{1 + \alpha_0^2}{\beta_0} = \sqrt{\bar{K}} \tag{A.10}$$

Focusing in the Deflection Plane of the TGU The equation of motion in an undulator for the x-z-plane is given by

$$\frac{d^2x}{ds^2} = x'' = \frac{eB_y(z)}{\gamma_e m_0 c} \tag{A.11}$$

with $\dot{z} \approx c$. In the region of the excursion of a beamlet along the undulator the field with the gradient $\frac{d\tilde{B}_y}{dx}$ is approximated linearly around the position for the reference trajectory x_E and the displacement $\Delta x = x - x_E$ with

$$B_y(\Delta x, z) \approx \left(\tilde{B}_y(x_E) + \left.\frac{d\tilde{B}_y}{dx}\right|_{x_E} \Delta x \right) \sin(k_u z)\,. \tag{A.12}$$

Inserting this equation into the equation of motion, one gets

$$x'' = \frac{e}{\gamma m_0 c} \left(\tilde{B}_y(x_E) + \left.\frac{d\tilde{B}_y}{dx}\right|_{x_E} \Delta x \right) . \sin(k_u z) \tag{A.13}$$

For the focusing only the change of the shape of the β_x is interesting, not the oscillation of the particles in the undulator. Therefore equation A.11 for a pure sinusoidal field is subtracted from A.13, i.e. $x_E'' = \frac{e\tilde{B}_y(x_E)}{\gamma_e m_0 c} \sin(k_u z)$. That results in a differential

equation similar to Hill's equation for the displacement Δx

$$(\Delta x)'' - \frac{e}{\gamma m_0 c} \left.\frac{d\tilde{B}_y}{dx}\right|_{x_E} \sin(k_u z)\, \Delta x = (\Delta x)'' + K_x(x_E)\Delta x = 0. \tag{A.14}$$

With the focusing K_x the transfer matrix M_u of the undulator can be calculated by multiplying focusing and defocusing matrices of subspaces of the undulator. To determine the condition for a β_x oscillating around a constant value β_{x_E} the condition $\beta_{x_0} = \beta_{x_{\text{end}}}$ and $\alpha_{x_0} = 0$ have to be fulfilled. That results in the condition

$$\beta_{x_0} = M_u^{(1,1)} \beta_{x_0} + \frac{M_u^{(1,3)}}{\beta_{x_0}} \tag{A.15}$$

or solving this equation for β_{x_0}

$$\beta_{x_0} = \sqrt{\frac{M_u^{(1,3)}}{1 - M_u^{(1,1)}}}. \tag{A.16}$$

B. Calculations for the Initial Parameters

B.1. Equation for the Normalized Emittance

M. Migliorati et al. describe the intrinsic constant growth of the normalized emittance in the beams of a LWFA [Migliorati et al., 2013]. Here a short summary of the derivation of the according equation is given.

The definition for the normalized emittance

$$\varepsilon_n^2 =< x^2 >< \beta_e^2\gamma_e^2 x'^2 > - < x\beta_e\gamma_e x' >^2 \tag{B.1}$$

with the averaged relativistic factor $< \gamma_e >$ can be simplified assuming that there is no correlation between energy and transverse position of the particles to

$$\varepsilon_n^2 =< \beta_e^2\gamma_e^2 >< x^2 >< x'^2 > - < \beta_e\gamma_e >^2 < xx' >^2 . \tag{B.2}$$

Replacing $< \beta_e^2\gamma_e^2 >$ in equation B.2 with the relative energy spread σ_δ[a] defined by

$$\sigma_\delta^2 = \frac{< \beta_e^2\gamma_e^2 - < \beta_e\gamma_e >^2}{< \gamma_e >^2} \tag{B.3}$$

gives under the assumption of ultra-relativistic particles with $\beta_e \approx 1$

$$\varepsilon_{n_{x,y}}^2 =< \gamma_e >^2 \left(\sigma_\delta^2\sigma_{x,y}^2\sigma_{x',y'}^2 + \varepsilon_{x,y}^2\right). \tag{B.4}$$

That means the normalized emittance grows along a drift space for a diverging beam as $\sigma_x = \sigma_{x'}s$ is increasing with the longitudinal coordinate s.

In conventional accelerators the approximation $\varepsilon_n =< \beta_e\gamma_e\varepsilon_{x,y} >$ is usually valid as the additional term can be neglected compared to the geometrical emittance. For the beams of the LWFA, where the energy spread is in the range of some percent and the divergence in range of 1 mrad or slightly above, that is not the case according to M.

[a] In [Migliorati et al., 2013] the variable for the relative energy spread is σ_E, but for consistence with the declaration in this thesis I replaced it with σ_δ.

Migliorati.

B.2. Simulations of Space Charge Effects with ASTRA

For calculating space charge effects with ASTRA I used a cylindrical geometry for the bunch. The bunch was divided in ten slices longitudinally and 10 rings in transverse direction. ASTRA calculates with macro-particles, which represent a number of single particle with the according charge, mass etc. The number of macro-particles, the bunch was consisted of, was increased till the beam parameters in the simulation converged. For the bunches with 10 pC I used 1×10^5 macro-particles, for the low-energetic background of 1 nC I used 0.9×10^6 macro-particles.

The bunches were generated with a perl-script, to be able to realize an arbitrary energy distribution. If no other distribution is given a Gaussian distribution is assumed for the variables. The values given in Tab. 4.1 correspond to σ.

For the calculation of the bunches with energies of 110 MeV and 460 MeV the 0.15 m drift space were divided in 20 steps for the calculation. The particle distribution of five steps was written to the hard disk and analyzed, i.e. the distribution of every 4th step is analyzed.

For the calculation with the low-energetic background the step size for the calculation had to be reduced significantly to obtain reasonable results: The length of the drift space was reduced to 1 mm and was divided into 2000 subspaces of which the distribution of 20 steps was written to the hard disk and analyzed.

For the statistical analysis of the bunch parameters was done using a perl-script.

C. Simulations of the Transport System

C.1. Parameters and Functions used for the Simulations

For the simulation of the beam transport system the programs MAD-X [PTC, 2002] and *elegant* [Borland, 2000] for the linear calculation of the beam parameters and the tracking studies are used. In this section the settings and parameters used for the calculation are listed. An explanation of the commands is given in the according manual.

The magnets are implemented as elements with finite length and a strength parameter of the magnetic field. The equations for calculating these parameters are given in section 2.1. In the following all lengths are given in meters, the angles in radians and particle energies in GeV in MAD-X and MeV in *elegant*.

C.1.1. Calculation of the Transport System with MAD-X

Drift Space The only parameters of the drift space is its length. The according element in MAD-X is defined with

```
DRIFT, L=<length>;
```

For the beam transport system the magnets are separated by drift spaces. In this way the drift spaces could be varied during some optimizations.

Dipoles The GMW dipoles have a rectangular pole shape with the beam entering the first dipole and leaving the second dipole perpendicular to the pole face. This has to be considered for the implementation of the dipoles. In MAD-X the RBEND with rectangular poles is used and pole faces, with are symmetrically oriented with respect to the beam path, have to be rotated. The deflection angle is $\theta = L/\rho$ with the Larmor radius ρ (equ. 2.2).

```
Dipole1:  RBEND, L=0.05, ANGLE=<angle>, E1=-<angle>/2,
      E2=<angle>/2, HGAP=0.01;
Dipole2:  RBEND, L=0.05, ANGLE=<angle>, E1=<angle>/2,
      E2=-<angle>/2, HGAP=0.01;
```

h_{gap} is half of the gap hight or width. The angles E_1 and E_2 change the sign with the sign of the deflection angle.

Quadrupoles The quadrupoles are implemented as thick quadrupoles with the quadrupole strength given in equation 2.17:

```
QUADRUPOLE, L=0.08, K1= <quadrupole strength>;
```

For the simulation of the combined quadrupole-sextupole magnets an additional parameter for multipoles in the quadrupole `knl={0,0,sX}` is added to the quadrupole element.

Linear Calculation The elements were combined to the transport system using

```
line=(<element1>,<element2>,...);
```

For calculating the Twiss parameters the twiss command was used with the following options:

```
twiss,betx=<value>,alfx=<value>,bety=<value>,alfy=<value>,...
     ...save,centre,file=<filename>;
```

For all elements the output is set to one value at the center. To calculate the shape of the beam functions along long drift spaces, those were split in a number of smaller drift spaces with the length 0.05 m.

Matching of End Parameters MAD-X provides a function to match e.g. the end parameters of the beam transport line to the target values by varying certain parameters. I usually left the drift spaces fixed and varied the strength of some quadrupoles for the matching. Here one example is given:

```
match, sequence=<name>, BETX=<initial value>, ALFX=<init.  value>,...;
constraint,sequence=<name>,range=#e,BETX=<target value>,...;
vary,name=<quadrupole strength>,step=1.0e-6;
...
simplex,calls=80000,tolerance=1.e-15;
endmatch;
```

As usual the initial quadrupole strengths influences the result of the simplex optimization, thus a variation of the initial parameters is recommended for the minimization.

Particle Tracking The particle tracking was done with the PTC Tracking Module. The PTC-tracking environment is started and a number of particles with a Gaussian distribution of the initial coordinates (x, y, x', y', δ) are generated. The particles are tracked

through the transport line. The particle distribution is written to a file at all elements marked with the PTC-observe function.

```
ptc_create_universe;
ptc_create_layout, model=2, method=6, nst=10, exact;
n=0;
while(n < <number particles>){n=n+1;
ptc_start, x=<sigma x>*gauss(), y=<sigma y>*gauss(),
      px=<sigma angle x>*gauss(), py=<sigma angle y>*gauss(),
      pt = <sigma energy spread>*gauss();}
ptc_observe, place = <element>;
ptc_track, icase=5, closed_orbit=false, element_by_element=true,
turns=1, dump, onetable=true;
ptc_track_end;
ptc_end;
```

C.1.2. Calculations of the Transport System with *elegant*

The definitions for the magnet elements in *elegant* are similar those in MAD-X. The beam transport systems simulated in *elegant* for this thesis are all linear systems. The simulations for the measurements were done in *elegant*, the calculation of the linear transfer matrix for the estimation of the longitudinal evolution of the bunch and the estimation of the influence of the CSR on the bunch with a one-dimensional model for the radiation fields.

The elements used are therefore only drift spaces, dipoles and quadrupoles:

```
DRIFT, L=<length>
RBEN, L=0.05, ANGLE=<deflection angle>, E1=<angle>, E2=<angle>
QUAD, L=0.08, K1=<quadrupole strength>
```

In the following paragraphs the parameters and functions used for the calculation are listed. I restricted the lists to the commands differing from the default options and did not list the options for generating output files that were not used for the evaluation.

Calculation of the Twiss Parameters The following script provides the calculation of the Twiss parameters:

```
  &run_setup
      lattice = <file>,
```

```
      default_order = 3,
      use_beamline = <name>,
      final = %s.fin
      p_central_mev = <central energy>,
      always_change_p0 = 0,
&end

&run_control
      n_steps = 1
      reset_rf_for_each_step = 0
&end

&twiss_output
      filename="%s.twi"
      matched = 0,
      final_values_only = 0,
      statistics = 0,
      beta_x=<initial value>, alpha_x=<initial value>
      beta_y=<initial value>, alpha_y=<initial value>
&end
```

For the output of the magnetic lattice the following option can be included into the 'run setup' command:

```
magnets = "%s.mag"
```

The complete linear transfer matrix of the six-dimensional phase space is printed to a file using the following commands after the calculation of the Twiss parameters:

```
&matrix_output
      printout = %s.mpr,
      printout_order = 1,
      full_matrix_only = 1
&end
```

Tracking of Particles For the particle tracking a bunch is generated with the command 'bunched beam'. This bunch is tracked through the layout of the according transport system. Note that it is necessary to include the 'run setup', the 'run control' commands and the calculation of the Twiss parameters before the tracking.

```
&bunched_beam
      n_particles_per_bunch = <number>,
```

```
      one_random_bunch=0,
      emit_x = <value emittance>,
      emit_y = <value emittance>,
      beta_x = <value>, alpha_x = 0,
      beta_y = <value>, alpha_y = 0,
      sigma_dp = <value relative energy spread>,
      sigma_s = <bunch length>,
      distribution_type[0] = "gaussian",
      distribution_cutoff[0] = 3,
      symmetrize = 1,
      enforce_rms_values[0] = 1,1,1,
&end

&track &end
```

For the calculation of the transverse alignment errors of the quadrupoles the following commands were added to the input file before the tracking command:

```
&error_control
      clear_error_settings = 1,
      error_log = "%s.erl"
&end

&error_element name="Q*", item="dy", amplitude=1.0e-3, type = "gaussian",
      cutoff=2.0, bind=0, fractional=0 &end
&error_element name="Q*", item="dx", amplitude=1.0e-3, type = "gaussian",
      cutoff=2.0, bind=0, fractional=0 &end

&error_control summarize_error_settings=1 &end
```

The influence of the coherent synchrotron radiation is included by replacing the dipoles by the bending magnet 'crscsben'. Note that this magnet is a sector magnet, i.e. the entrance and exit angle have to be adapted. In the example the first and the second value corresponds to the value of the according dipole.

```
CSRCSBEN,L= 0.05,
      ANGLE= <deflection angle>,
      E1=0/<deflection angle>,E2=<deflection angle>/0,
      SG_HALFWIDTH=0,SG_ORDER=1,STEADY_STATE=0,BINS=600,
      N_KICKS=10,INTEGRATION_ORDER=4,
      ISR=0,CSR=1,
      OUTPUT_LAST_WAKE_ONLY=1,OUTPUT_INTERVAL=5,
```

```
DERBENEV_CRITERION_MODE = evaluate
```

C.2. Monte-Carlo-Simulations for the Linear System

To scan the possible parameter range, i.e. the quadrupole strength that can be achieved with the available magnets and the lengths for the drift spaces such that the total length of the system is around 5 m, a Monte-Carlo-Simulation was performed. The results were analyzed by sorting the results with respect to the deviation of the optimum end values. Limiting the solutions to a certain range of deviations and looking at the correlation different types of solution can be found and analyzed.

To limit the dimensions of the parameter space as many parameters as possible are kept constant. The distances of the quadruples are varied in concrete steps, while the strength of the magnets is varied as a random number in a certain interval. First optimizations showed that it is necessary to keep the quadrupole strengths in the first triplet, the distances of the magnets and Q_4 constant.

For each combination of parameters the transfer matrices of the transport system are calculated using the simple matrix formalism implemented in a Perl-script[a]. The deviation Δ from the optimum end parameters is determined with the following equation:

$$\Delta = (5(\beta_x - \beta_{x,t}))^4 + (5(\beta_y - \beta_{y,t}))^4 + (5(\alpha_x - \alpha_{x,t}))^4 + (4(\alpha_y - \alpha_{y,t}))^4$$

The equation was chosen such that a minimum in the accepted range around the optimum end values is given.

An example for the correlations determined for an achromatic transport system with matched Twiss parameters is given in Fig. C.1. The varied quadruple strengths are the one from the last triplet and the solutions are limited to the two combinations “defocusing - focusing - defocusing” and the opposite polarization of the quadrupoles. For the quadrupoles of the triplet there are two different regions with solutions found. For both regions solutions were analyzed to make a choice on the configuration used for further simulations.

A similar analysis was done for several parameters and magnet configurations. The simulation shown here is just one example of such an analysis.

[a] The results of the Perl-script were benchmarked with the output of the MAD-X Twiss module.

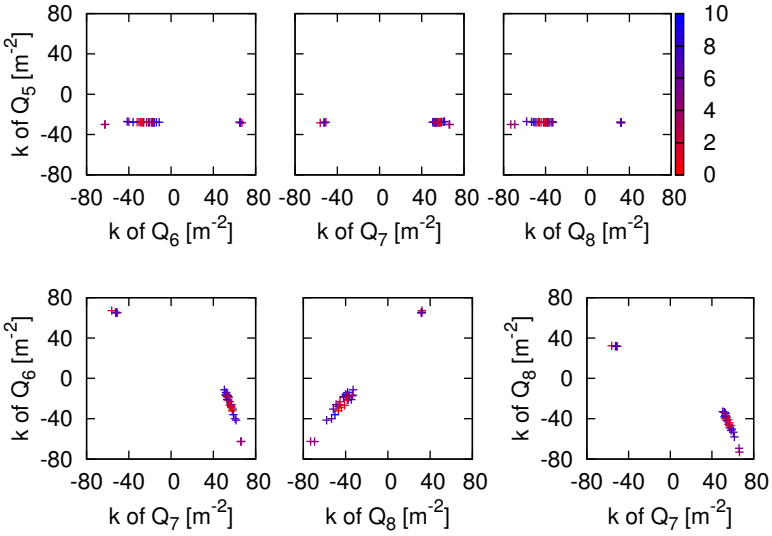

Figure C.1.: Correlation of the strength of different quadrupoles for solutions with a deviation Δ of 10 or smaller.

C.3. Implementation of the Chromatic Correction

For visualizing the influence of single sextupoles on the beam transport system. In the following graphs a sextupole component was added to single quadrupoles. Five cases are shown: The strength of the sextupole component is set to $\pm m_{\max}$. The maximum strength applied at the different locations depends was adapted such that a certain influence is visible, but the distortion of the profile is not too strong.

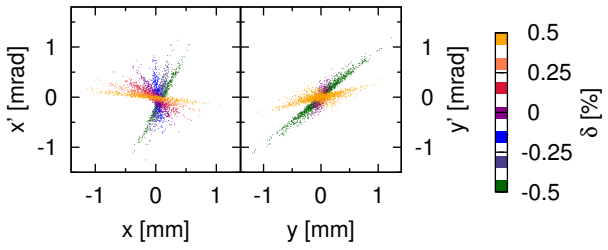

(a) Without Sextupoles

Figure C.2.: Phase space profiles with an additional sextupole component in quadrupoles Q_2 to Q_8. The maximum sextupole strength $m_{\max}$ is given in each plot. The same color code is used for all plots. (Continued on next page.)

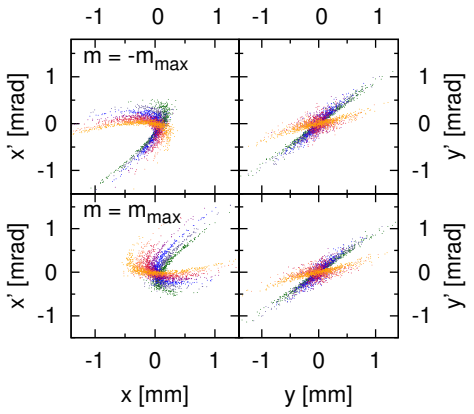

(b) S_2 with $m_{max} = 10\,\mathrm{m}^{-2}$

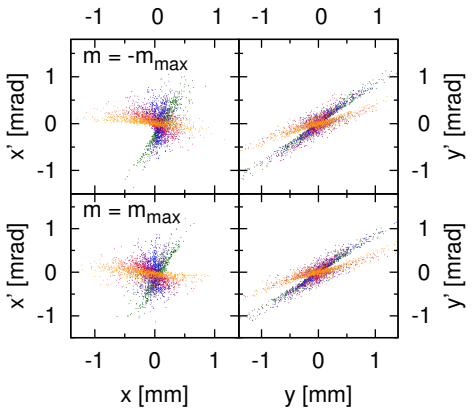

(c) S_3 with $m_{max} = 10\,\mathrm{m}^{-2}$

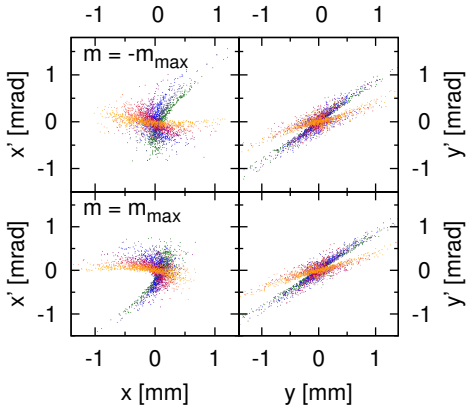

(d) S_{41} with $m_{max} = 100\,\mathrm{m}^{-2}$

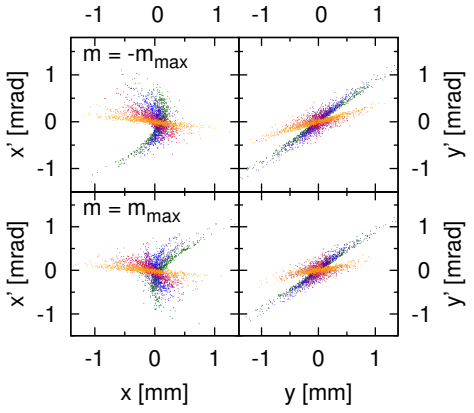

(e) S_{42} with $m_{max} = 400\,\mathrm{m}^{-2}$

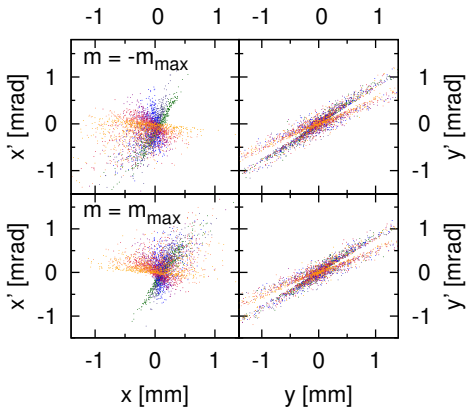

(f) S_5 with $m_{max} = 400\,\mathrm{m}^{-2}$

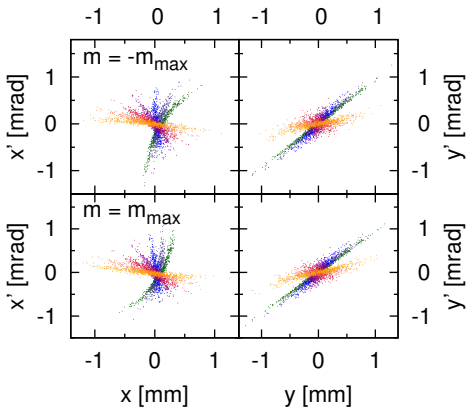

(g) S_6 with $m_{max} = 1000\,\mathrm{m}^{-2}$

Figure C.2.: Phase space profiles with an additional sextupole component in quadrupoles Q_2 to Q_8. The maximum sextupole strength m_{max} is given in each plot. (Continued on next page.)

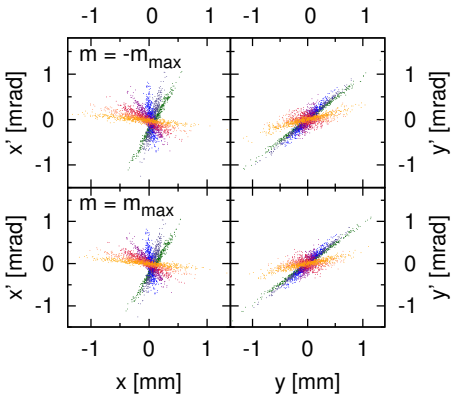

(h) S_7 with $m_{max} = 600\,\mathrm{m}^{-2}$

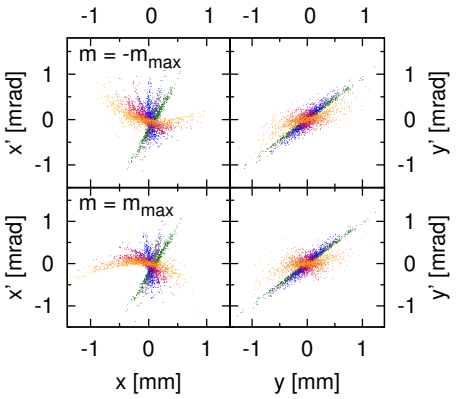

(i) S_8 with $m_{max} = 1000\,\mathrm{m}^{-2}$

Figure C.2.: Phase space profiles with an additional sextupole component in quadrupoles Q_2 to Q_8. The maximum sextupole strength m_{max} is given in each plot.

C.4. Simulation of the Radiation Spectra

All simulations of the radiation spectra in this thesis are done with *wave* [Scheer, 2012]. In wave the trajectory of each particle in the magnetic field of the undulator is calculated and the radiation fields are determined from this trajectory. The magnetic fields of the TGU used for the tracking are exported from OPERA (see e.g. [Braun, 2014] for details). The model of the TGU consist of two cylindrical coils with 200 periods each. The particles are tracked through the 100 periods in the center to avoid influences of the fringe fields. The observation point for the spectra is set to 100 m, thus the near-field effects are neglected.

Simulations for Finding the Optimum Beam Size along the TGU In Fig. 4.8 the spectra emitted by beam with varying initial parameters passing the TGU are shown. The bunches in the simulation consisted of 1000 electrons. In y the initial parameters for a constant β-function along the TGU were assumed, i.e. $\beta_{y_0} = 0.6\,\mathrm{m}$ and $\alpha_{y_0} = 0$. In x the waist of the electron beam was at the center of the TGU. For a variation of the value $\beta_{x,\mathrm{center}}$ at the center the initial parameters were calculated with $\beta_{x_0} = \beta_{x,\mathrm{center}} + (L/2)^2/\beta_{x,\mathrm{center}}$ with the length L of the TGU and $\alpha_{x_0} = (L/2)/\beta_{x,\mathrm{center}}$, i.e. a drift space with beam waist at the center is assumed. The starting position for each energy is the optimized position in x and $y_0 = 0\,\mathrm{m}$ according to the Bachelor's thesis of N. Braun [Braun, 2013].

Simulations with Beam Tracked through the Transport System For the simulations presented in section 5.2.3 subbunches of 500 electrons each and a bunch with a Gaussian energy distribution with 1500 electrons each were tracked through the TGU. The initial distribution is taken from the MAD-X output file and transfered to the coordinate system of *wave*. The position of the reference trajectory is set to the optimum transverse entrance position for 120 MeV, i.e. the entrance angle and the entrance position of the bunches and subbunches from the beam transport system are not shifted.

Spectral Acceptance of the TGU To determine the acceptance of the TGU with respect to the properties of the spectra single electrons were tracked through the TGU. The maximum value and the width of the emitted spectrum is analyzed for each spectrum [Bernhard et al., 2016]. The acceptance is defined as the phase space volume in which the maximum value of the spectrum and the spectral width are in the required range. In Fig. C.3 the accepted phase space volume for different criteria is shown.

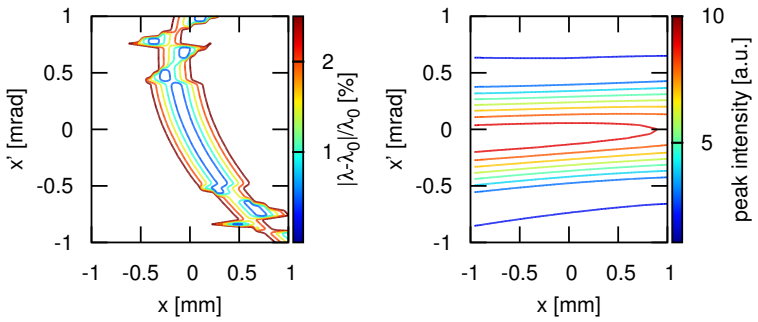

Figure C.3.: Acceptance of the TGU for 120 MeV in the x-x' phase space. On the left contour lines for the acceptable phase space volume with respect to the bandwidth, on the right the phase space acceptance with respect to the peak intensity of the emitted spectrum is shown (data from [Bernhard et al., 2016]).

D. Detailed Description of the Experimental Setup

D.1. Position and Mounting of the Magnets

The complete beam transport system that was set up at the LWFA in Jena consisted of two dipoles and six quadrupoles. The positions of the magnets along the reference orbit of the beam are shown in Fig. D.1. Two of the quadrupoles are of type I with quadrupole coils, four of them are of type II and have sextupole coils. All magnets except the first quadrupole were installed in a system of four vacuum boxes (each 495 mm (height) x 554 mm (length) x 355 mm (width)), which are connected with frames. The first quadrupole is placed inside the target chamber, where the mirrors and the parabola for guiding and focusing of the laser pulse and the gas cell were located.

As the dipoles deflect the electron beam downwards with an angle of 17.8 mrad quadrupole Q4 to Q6 were mounted on a inclined base such that the longitudinal axis of the quadrupoles matches the inclined reference orbit of the beam.

During the experiments three different magnet configurations were used, one for each position of the scintillating screen. Note that the positions of single magnets is not changed from one configuration to the other, there are just magnets added to the configuration and the beam profile screen was moved. In the first two configurations the beam profile screen can be removed to send the electrons to the spectrometer. In the last configuration the dipoles cause a shift in the vertical position of the reference orbit, thus the entrance of the spectrometer is not aligned to the beam axis. Furthermore the connection of the vacuum boxes to the spectrometer is replaced by the vacuum chamber of the scintillating screen. Therefore the spectrometer cannot be used in the third configuration.

All quadrupoles were mounted on a vertical linear translation stage of Newport with a translation length of 20 mm[a]. Quadrupole Q1, Q3, Q4 and Q6 had an additional linear

[a] Newport Precision Ball Bearing Vertical Linear Stage M-MVN120

stage for alignment in y with a translation length of 40 mm[b]. All stages are motorized with a step motor of Faulhaber. The magnets can therefore be aligned remote in vacuum. The control boxes and the conversion from the motor to the screw of the linear stage are in-house built at the University of Jena. The step size of the motors is not calibrated. It is in the range of 30 000 steps/mm. For the alignment of the quadrupoles usually some 1000 steps per iteration were used.

The quadrupoles with the linear stages are only fixed with blocks on the base plate of the boxes to avoid slipping, they are not clamped. That is possible as the magnets are heavy enough that they do not move in vertical direction and as there is no significant vibration of the vacuum boxes.

To identify the quadrupoles, the quadrupole of type I are numbered with QG1 and QG2, of type II with QK1 to QK4. The distribution in the setup was the following:

magnet in experiment	quadrupole
Q1	QK4
Q2	QG1
Q3	QK1
Q4	QK2
Q5	QG1
Q6	QK3

Table D.1.: List of the quadrupoles and their position in the experiment.

[b] Newport Single-Row Ball Bearing Linear Stage M-UMR12.40

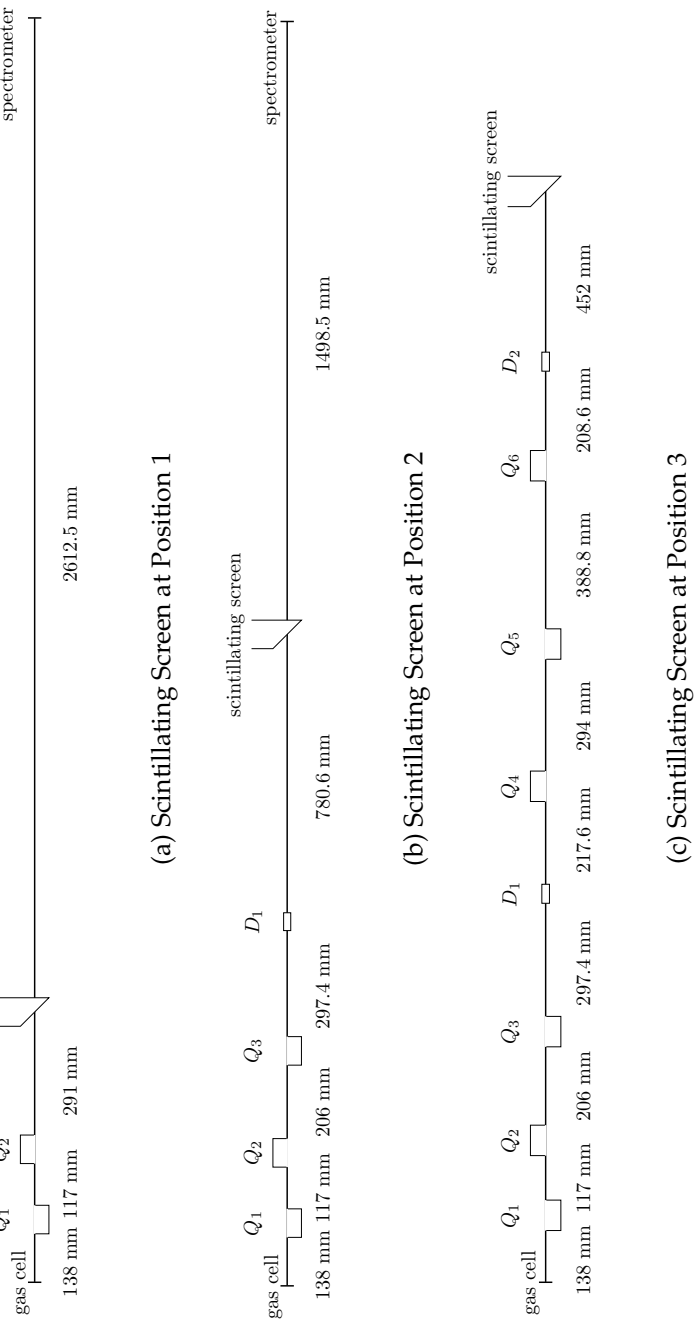

Figure D.1.: Position of the magnets for the three different configurations i.e. different positions of the beam profile screens (BPS). The numbers correspond to the length of the drift spaces, the pole length of the quadrupoles is 80 mm, of the dipoles 50 mm.

D.2. Parameters of the Magnets

In the following table the data for the dipoles and the two different quadrupole types are listed:

	dipole	quadrupole type I	quadrupole type II
length x width x height	189 x 377 x 218 mm	163 x 250 x 250 mm	163 x 258 x 258 mm
yoke length	50 mm	80 mm	80 mm
magnetic gap radius	10 mm	11 mm	11 mm
weight	27 kg	25 kg	22 kg
number of turns/coil		465	412
maximum current	5 A	5.5 A	5 A
field at max. current	460 mT	-	-
gradient at max. current	-	35 T/m	29 T/m

Table D.2.: Data of the magnets: The data of the dipoles is given in the data sheet of the supplier, the data for the quadrupoles is determined by simulations or measurements.

In Fig. D.2 on the left the gradient that was determined by measuring the field along a vertical line with a hall probe at the center of the magnet is shown for different currents. As there were no measurements of the field or the gradient along the longitudinal axis performed, the simulated field curves were taken with the values at the center rescaled to the measured values. That is necessary as the current in the simulation program is given via a current density while in the experiment an absolute current is given by the power supply. A direct comparison is therefore not possible.

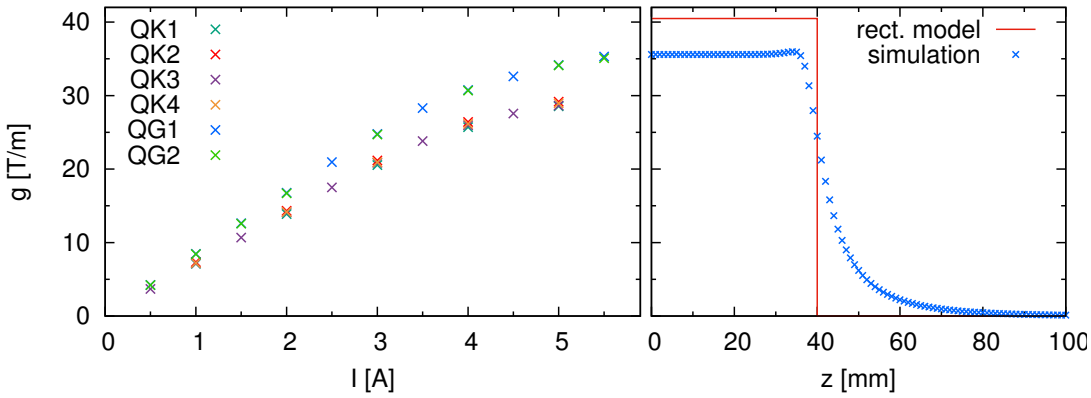

Figure D.2.: *left:* Gradient measured at the center of the quadrupole for different currents. *right:* Gradient along the quadrupole simulated for the maximum current compared to the rectangular field assumed for the measurements. The center of the magnet is at $z = 0$. The field value at the center is rescaled to the measured value.

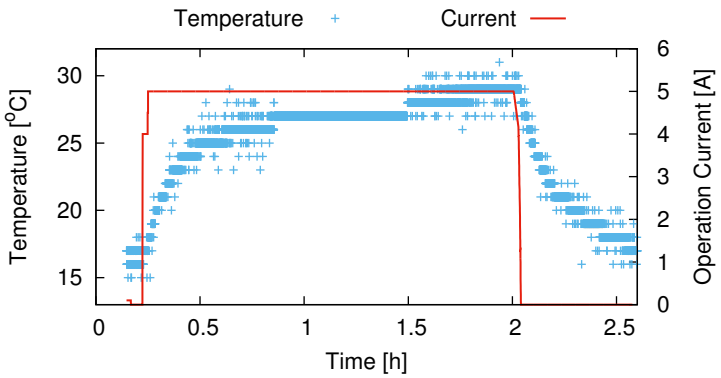

Figure D.3.: Temperature curve of a sextupole magnet at maximum operation current of 5 A in vacuum.

For the simulation of the beam transport system a rectangular field model as shown in Fig. D.2 on the right is applied. For the deflection in the quadrupole the total strength along the axis is relevant, not only the maximum value in the center. To implement the total strength in the control system the simulated field values are integrated and the maximum value of the rectangular field is chosen such that both field integrals are equal. In Fig. D.2 the comparison of the rectangular field with a maximum value of 40.48 T and the simulated field rescaled to the measured value of 35.98 T at 5.5 A are shown.[c]

Cooling System of the Magnets All magnets are water cooled. The cooling water in the laboratory in Jena has a temperature of 16 °C. The copper cooling pipe for the quadrupoles is glued to the cooling channels in the winding bodies of the coils. The inner diameter is 5 mm, though it is narrower where it was bent. The nominal flow is 1 l/min. The coils of one magnet are connected in series. The cooling water supply is connected with pipes of synthetic material. All magnets are connected in parallel.

A temperature test was performed for a sextupole magnet, a magnet with six poles and the coils also used for the small quadrupoles, at the maximum current of 5 A. The sextupole was installed in vacuum with the same infrastructure used for the quadrupoles during the experiment. The measured temperature curve is shown in Fig. D.3. The temperature rises to a maximum of 30 °C during almost two hours of operation. This maximum is well below the operation temperature in the simulations, which was

[c] During the tests of a quadrupole of type I it was shown that the temperature was still far below the temperature limits for 5 A. An additional measurement point at 5.5 A was added. In general the magnets can be operated even at higher currents.

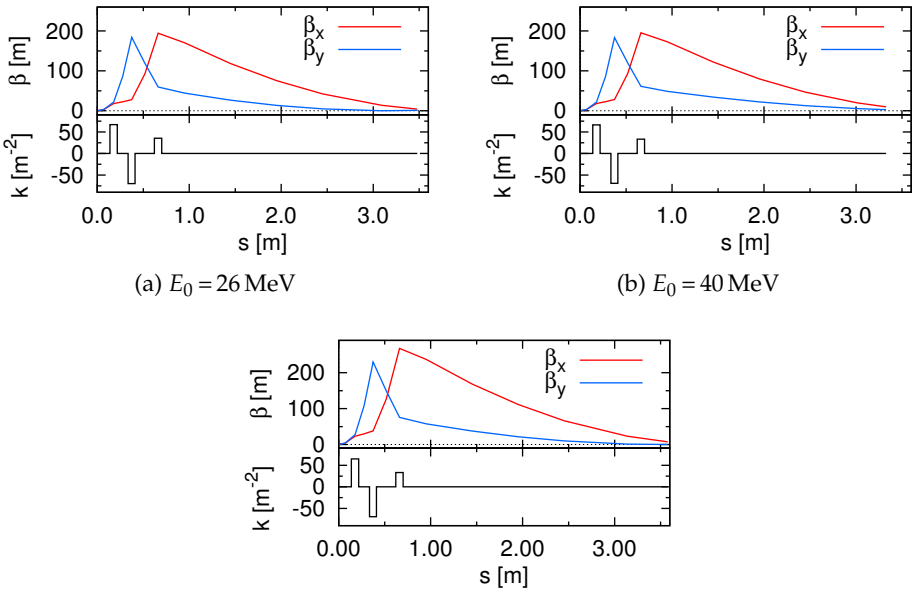

(a) $E_0 = 26\,\mathrm{MeV}$ (b) $E_0 = 40\,\mathrm{MeV}$

(c) $E_0 = 60\,\mathrm{MeV}$

Figure D.4.: Configurations for focusing the electron bunches to the screen of the spectrometer.

64 °C. This discrepancy is caused by a very conservative model for the heat transport in the coils. As the measured value is far below the damage threshold of the coils a stable long time operation of the magnets during the experiments is possible.

D.3. Configurations for Measuring the Spectra

For measuring the spectra the optics were configured such that certain energies are focused to the screen of the spectrometer. The optic configurations are shown in Fig. D.4. Note that the travel length inside the spectrometer is different for each energy. The length given during the measurements was slightly corrected during the evaluation of the spectra [Leier, 2015].

D.4. Simulation of the Beam Profiles

For the simulation of the beam profiles a bunch of 50 000 particles was tracked through the magnetic lattice using the tracking module of *elegant*. The bunches are generated with the SDDSbeam command.

In Fig. 6.9 and Fig. 6.11b only one example for each case is shown. These examples

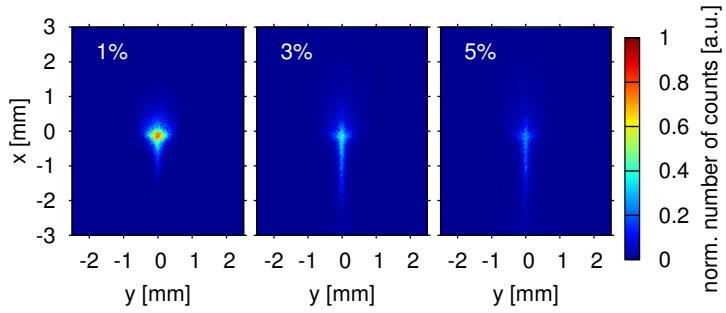

(a) Variation of the Energy Spread

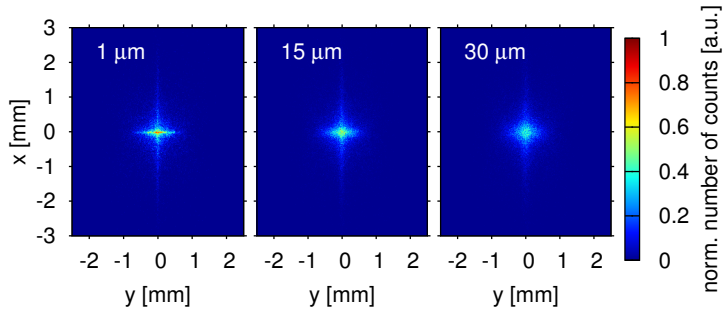

(b) Variation of the Source Size

Figure D.5.: Comparison of different cases with a variation of (a) the energy spread of the bunch for the setup shown in Fig. 6.8b with parameters corresponding to case IV in Table 6.2 and (b) the source sizes for the setup shown in Fig. 6.8a and with parameters corresponding to case V of Table 6.2. For the three plots the same color code is applied.

are chosen such that the influence of the parameter can be observed clearly. For the relative energy spread the value was set to 3 % though in the experiment it is much higher as most of the particles do not reach the detector area of 3 mm x 3 mm, which is evaluated for the plots. In Fig. D.5a the profile for three different values of the energy spread are shown. For 5 % energy spread 18 % of the particles are not on the screen, for 3 % energy spread 6 % are lost. If an aperture similar to the gap of the magnets is introduced into the simulation the number of lost particles is unchanged. The finite aperture of the magnets does not lead to particle loss.

For the simulation of different source sizes the divergence was set to the measured values. Therefore the increase of the source size leads to an additional increase of the emittance. The value of 1 µm is actually smaller than the source size of 10 µm usually set as initial value. The profile has sharper lines in this case. The case of 10 µm is shown in the second profile in Fig. D.5a. The increase of the source size does not lead to any additional particle loss. It only smears the shape.

Acknowledgements

The time of the PhD is an exciting and challenging period in life with a lots of surprises. I wonder if I learned more about physics or about myself during this time. I'm grateful that I had a many people around me that supported me during this time with advice, encouragement and patience. Here, I just want to mention some of them.

First of all I want to thank Prof. Anke-Susanne Müller for the support, for good discussions and for her encouragement. She always gave me the possibility to pursue my ideas and had confidence in what I did, but also had suggestions for improvements of my work. I'd like to thank Prof. Marc Weber for his advice and feedback for my dissertation and the preparation of the defense. And I want to thank Prof. Tilo Baumbach for accepting me as a PhD student at the beginning of my work in the project.

Special thanks also go to all members of the LAS at Campus South. Life at LAS is diverse and full of surprises every time you open a new door or drawer. Usually it is silent there far away from Campus North and the physics building, but one can also have evenings with barbecue on one of the roof terraces. My colleagues in the group at the LAS made this a place with pleasant and constructive atmosphere, where I enjoyed working even during hard times with few or poor results. Thanks to my colleagues Veronica Afonso Rodriguez, Deniz Birli, Sandra Ehlers, Michael Fischer, Julian Gethmann, Steffen Hillenbrand, Alexander Keilmann, Peter Peiffer, Walter Werner, Robert Rossmanith and, representatively for all the students, Nils Braun, Bastian Härer, Stefan Letzelter and Andreas Will, who contributed to the results of this thesis. And last but not least I'd like to thank Axel Bernhard, who leads this group, for the supervision of my work, a lot of patience, constructive critics and advice, encouragement and support during all the time.

I also want to thank Klaus Eichhorn, who taught me many things concerning organization, time management and structuring work and helped me with these tools to find my way through the PhD, and Prof. Hans Wondratschek, for sharing his experience in academic life and for his humor.

I'd like to thank also all the current and former members of the THz-group at ANKA for support, feedback and help in the special THz-manner whenever I needed it, es-

pecially Nicole Hiller, Michael Nasse, Vitali Judin, Markus Schwarz, Benjamin Kehrer and Edmund Blomley and Anne Stößer from the ANKA administration.

The planning of the experiments at the LWFA in Jena and the measurements could only be done with the support of the scientists, engineers and technicians at the institutes there. Many thanks to Prof. Malte Kaluza for helpful discussions, for providing a lots of data and information and for the possibility of realizing the experiments, to Maria Leier for endless hours in the lab and the control room during the experiments and many emails and phone calls, to Alexander Sävert for the support during the whole time of the project and to Matthew Schwab, Oliver Jäckel, Maria Reuter, Thorsten Rinck and Stephan Kuschel for the help during the measurements. The technical construction of the experimental setup was mainly done by Wolfgang Ziegler. Many thanks to him representatively for all who contributed to the planning and realization of the setup and all of its components. And thanks a lot to Falk Ronneberger and Burgard Beleites for the operation of the JETI laser system during the measurement times.

I'd like to thank Michael Scheer for the help with *wave* and Godehard Wüstefeld for helpful discussions concerning the beam dynamics in undulators.

And finally I want to thank my husband, my family and all my friends who supported me during the last years and had a lot of patience with me, encouraged me during the difficult times and celebrated with me in successful moments.

My work was partly funded by the German Federal Ministry for Education and Research under contract no. 05K10VK2 and 05K10SJ2 and partly by the Helmholtz Association on the framework of the ARD program.

Soli Deo Gloria.

Bibliography

[Aad et al., 2012] Aad, G., Abajyan, T., Abbott, B., Abdallah, J., Khalek, S. A., and ATLAS Col. (2012). Observation of a new particle in the search for the Standard Model Higgs boson with the ATLAS detector at the LHC . *Physics Letters B*, 716(1):1–29.

[Afonso Rodriguez, 2015] Afonso Rodriguez, V. (2015). *Electromagnetic Design, Implementation and Test of a Superconducting Undulator with a Transverse Gradient Field Amplitude*. PhD thesis, Karlsuhe Institute of Technology (KIT).

[Afonso Rodriguez et al., 2011] Afonso Rodriguez, V., Baumbach, T., Bernhard, A., Keilmann, A., Rossmanith, R., Peiffer, P., Widmann, C., Nicolai, M., Kaluza, M., and Fuchert, G. (2011). Design Optimization for a non-planar Undulator for the JETI-Laser-Wakefield-Accelerator in Jena. In *Proceedings of the IPAC'11*, page TUPO005.

[Afonso Rodriguez et al., 2014] Afonso Rodriguez, V., Bernhard, A., Grau, A., Peiffer, P., Rossmanith, R., Weber, M., Widmann, C., Will, A., Kaluza, M. C., Nicolai, M., Saevert, A., and Reuter, M. (2014). Construction and First Magnetic Field Test of a Superconducting Transverse Gradient Undulator for the Laser Wakefield Accelerator in Jena. In *Proceedings of the IPAC 2014*, page WEPRO036.

[Afonso Rodriguez et al., 2013] Afonso Rodriguez, V., Bernhard, A., Keilmann, A., Peiffer, P., Rossmanith, R., Widmann, C., Baumbach, T., Nicolai, M., and Kaluza, M. (2013). Development of a Superconducting Transverse-Gradient Undulator for Laser-Wakefield Accelerators. *IEEE Transactions on Applied Superconductivity*, 23(3):4101505–4101505.

[ANKA Homepage, 2016] ANKA Homepage (2016). Homepage of the Synchrotron Facility ANKA.

[Bahrdt and Ivanyushenkov, 2013] Bahrdt, J. and Ivanyushenkov, Y. (2013). Short Period Undulators for Storage Rings and Free Electron Lasers. *Journal of Physics: Conference Series*, 425(3):032001.

[Bernhard, 2011] Bernhard, A. (2011). Beschleunigerphysik II - Synchrotronstrahlungsquellen. Lecture Notes.

[Bernhard et al., 2015] Bernhard, A., Afonso Rodriguez, V., Senger, J., Werner, W., Widmann, C., Mueller, A.-S., et al. (2015). Compact In-Vacuum Quadrupoles for a Beam Transport System at a Laser Wakefield Accelerator. In *Proceedings of the IPAC 2015*, page WEPMA038.

[Bernhard et al., 2016] Bernhard, A., Braun, N., Afonso Rodriguez, V., Peiffer, P., Rossmanith, R., Widmann, C., and Scheer, M. (2016). Radiation Emitted by Transverse-Gradient Undulators. *PRAB*. submitted.

[Borland, 2000] Borland, M. (2000). elegant: A Flexible SDDS-Compliant Code for Accelerator Simulation. *Advanced Photon Source LS-287*.

[Braun, 2013] Braun, N. (2013). Simulation der Strahlung von Elektronen in einem zylindrischen Undulator. Bachelor's Thesis.

[Braun, 2014] Braun, N. (2014). Zusammenfassung der HiWi-Tätigkeit. Internal Report.

[Brunetti et al., 2010] Brunetti, E., Shanks, R. P., Manahan, G. G., Islam, M. R., Ersfeld, B., Anania, M. P., Cipiccia, S., Issac, R. C., Raj, G., Vieux, G., Welsh, G. H., Wiggins, S. M., and Jaroszynski, D. A. (2010). Low Emittance, High Brilliance Relativistic Electron Beams from a Laser-Plasma Accelerator. *Phys. Rev. Lett.*, 105(21):215007.

[Buck et al., 2011] Buck, A., Nicolai, M., Schmid, K., Sears, C. M. S., Savert, A., Mikhailova, J. M., Krausz, F., Kaluza, M. C., and Veisz, L. (2011). Real-time observation of laser-driven electron acceleration. *Nat Phys*, 7(7):543–548.

[Bulanov et al., 1998] Bulanov, S., Naumova, N., Pegoraro, F., and Sakai, J. (1998). Particle injection into the wave acceleration phase due to nonlinear wake wave breaking. *Physical Review E*, 58(5):R5257.

[Carey, 1986a] Carey, D. (1986a). *The Optics of Charged Particle Beams*. Accelerators and Storage Rings vol. 6. Harwood Academic Publishers.

[Carey, 1986b] Carey, D. (1986b). *The Optics of Charged Particle Beams*, chapter 7, page 123ff. Accelerators and Storage Rings vol. 6. Harwood Academic Publishers.

[Casalbuoni et al., 2015] Casalbuoni, S., Cecilia, A., Gerstl, S., Glamann, N., Grau, A., Holubek, T., Meuter, C., de Jauregui, D. S., Voutta, R., Boffo, C., Gerhard, T., Turenne, M., and Walter, W. (2015). Recent Development on Superconducting Undualtors at ANKA. In *Proceedings of the IPAC 2015*, page WEBD3.

[Chatrchyan et al., 2012] Chatrchyan, S., Khachatryan, V., Sirunyan, A., Tumasyan, A., Adam, W., and CMS Col. (2012). Observation of a new boson at a mass of 125 GeV with the CMS experiment at the LHC . *Physics Letters B*, 716(1):30–61.

[Clarke, 2004] Clarke, J. A. (2004). *The Science and Technology of Undulators and Wigglers*. Number 4 in Oxford Series on Synchrotron Radiation. Oxford University Press.

[CryoVac, 2014] CryoVac (2014). CryoVac GmbH & Co. KG.

[Derbenev et al., 1995] Derbenev, Y., Rossbach, J., Saladin, E., and Shiltsev, V. (1995). Microbunch Radiative Tail-Head Interaction. DESY Report No. TESLA-FEL 95-05.

[Elder et al., 1947] Elder, F. R., Gurewitsch, A. M., Langmuir, R. V., and Pollock, H. C. (1947). Radiation from Electrons in a Synchrotron. *Phys. Rev.*, 71:829–830.

[Emma et al., 2015] Emma, P. et al. (2015). A Plan for te Development of Superconducting Undulator Prototypes for LCLS-II and Future FELs. In *Proceedings of FEL2014*, page THA03.

[Esarey et al., 2009] Esarey, E., Schroeder, C. B., and Leemans, W. P. (2009). Physics of laser-driven plasma-based electron accelerators. *Reviews Of Modern Physics*, 81(3):1229–1285.

[Faure et al., 2004] Faure, J., Glinec, Y., Pukhov, A., Kiselev, S., Gordienko, S., Lefebvre, E., Rousseau, J. P., Burgy, F., and Malka, V. (2004). A laser-plasma accelerator producing monoenergetic electron beams. *Nature*, 431(7008):541–544.

[Faure et al., 2006] Faure, J., Rechatin, C., Norlin, A., Lifschitz, A., Glinec, Y., and Malka, V. (2006). Controlled injection and acceleration of electrons in plasma wakefields by colliding laser pulses. *Nature*, 444(7120):737–739.

[Floettmann, 2011] Floettmann, K. (2011). *ASTRA - A Space Charge Tracking Algorithm*. User's Manual.

[Fuchert, 2009] Fuchert, G. (2009). Modelle für supraleitende Undulatoren an kompakten Synchrotronstrahlungsquellen mit Laser-Wakefield-Beschleunigern. Master's thesis, Karlsruhe Institute of Technology (KIT).

[Fuchert et al., 2012] Fuchert, G., Bernhard, A., Ehlers, S., Peiffer, P., Rossmanith, R., and Baumbach, T. (2012). A novel undulator concept for electron beams with a large energy spread. *Nuclear Instruments and Methods in Physics Research Section A: Accelerators, Spectrometers, Detectors and Associated Equipment*, 672(0):33–37.

[Fuchs et al., 2009] Fuchs, M., Weingartner, R., Popp, A., Major, Z., Becker, S., Osterhoff, J., Cortrie, I., Zeitler, B., Hoerlein, R., Tsakiris, G. D., Schramm, U., Rowlands-Rees, T. P., Hooker, S. M., Habs, D., Krausz, F., Karsch, S., and Gruener, F. (2009). Laser-driven soft-X-ray undulator source. *NATURE PHYSICS*, 5(11):826–829.

[Geddes et al., 2008] Geddes, C. G. R., Nakamura, K., Plateau, G. R., Toth, C., Cormier-Michel, E., Esarey, E., Schroeder, C. B., Cary, J. R., and Leemans, W. P. (2008). Plasma-density-gradient injection of low absolute-momentum-spread electron bunches. *Physical Review Letters*, 100(21):215004.

[Geddes et al., 2004] Geddes, C. G. R., Toth, C., van Tilborg, J., Esarey, E., Schroeder, C. B., Bruhwiler, D., Nieter, C., Cary, J., and Leemans, W. P. (2004). High-quality electron beams from a laser wakefield accelerator using plasma-channel guiding. *Nature*, 431(7008):538–541.

[GMW, 2013] GMW (2013). GMW electromagnet model 4370.

[Gonsalves et al., 2011] Gonsalves, A. J., Nakamura, K., Lin, C., Panasenko, D., Shiraishi, S., Sokollik, T., Benedetti, C., Schroeder, C. B., Geddes, C. G. R., van Tilborg, J., Osterhoff, J., Esarey, E., Toth, C., and Leemans, W. P. (2011). Tunable laser plasma accelerator based on longitudinal density tailoring. *Nat Phys*, 7(11):862–866.

[Grüner et al., 2007] Grüner, F., Becker, S., Schramm, U., Eichner, T., Fuchs, M., Weingartner, R., Habs, D., Meyer-ter Vehn, J., Geissler, M., Ferrario, M., Serafini, L., van der Geer, B., Backe, H., Lauth, W., and Reiche, S. (2007). Design considerations for table-top, laser-based VUV and X-ray free electron lasers. *Applied Physics B*, 86(3):431–435.

[Gschwendtner et al., 2014] Gschwendtner, E. et al. (2014). AWAKE: Advanced Proton Driven Plasma Wakefield Acceleration Experiment at CERN. In *Proceedings of LINAC2014*, page FRIOA06.

[Haerer, 2013] Haerer, B. (2013). Chromatische Korrektur einer Elektronenstrahlfuehrung fuer den Laser-Wakefield-Beschleuniger in Jena. Master's thesis, Karlsruhe Institute of Technology.

[Hofmann, 2004] Hofmann, A. (2004). *The Physics of Synchrotron Radiation*. Cambridge University Press.

[Hooker, 2013] Hooker, S. M. (2013). Developments in laser-driven plasma accelerators. *Nat Photon*, 7(10):775–782.

[Huang et al., 2012] Huang, Z., Ding, Y., and Schroeder, C. B. (2012). Compact X-ray Free-Electron Laser from a Laser-Plasma Accelerator Using a Transverse-Gradient Undulator. *Phys. Rev. Lett.*, 109:204801.

[Ivanyushenkov et al., 2013] Ivanyushenkov, Y. et al. (2013). Advances in Superconducting Undulators. In *Proceedings of PAC2013*, page FRYBB1, Pasadena, USA.

[Ivanyushenkov et al., 2015] Ivanyushenkov, Y., Harkay, K., Abliz, M., Boon, L., Borland, M., Capatina, D., Collins, J., Decker, G., Dejus, R., Dooling, J., Doose, C., Emery, L., Fuerst, J., Gagliano, J., Hasse, Q., Jaski, M., Kasa, M., Kim, S. H., Kustom, R., Lang, J. C., Liu, J., Moog, E., Robinson, D., Sajaev, V., Schroeder, K., Sereno, N., Shiroyanagi, Y., Skiadopoulos, D., Smith, M., Sun, X., Trakhtenberg, E., Vasserman, I., Vella, A., Xiao, A., Xu, J., Zholents, A., Gluskin, E., Lev, V., Mezentsev, N., Syrovatin, V., Tsukanov, V., Makarov, A., Pfotenhauer, J., and Potratz, D. (2015). Development and operating experience of a short-period superconducting undulator at the Advanced Photon Source. *Phys. Rev. ST Accel. Beams*, 18:040703.

[Jaroszynski et al., 2006] Jaroszynski, D., Bingham, R., Brunetti, E., Ersfeld, B., Gallacher, J., van der Geer, B., Issac, R., Jamison, S., Jones, D., de Loos, M., Lyachev, A., Pavlov, V., Reitsma, A., Saveliev, Y., Vieux, G., and Wiggins, S. (2006). Radiation sources based on laser–plasma interactions. *Philosophical Transactions of the Royal Society A: Mathematical, Physical and Engineering Sciences*, 364(1840):689–710.

[Kaluza, 2009] Kaluza, M. (2009). High intensity relativistic optics. Lecture Notes.

[Kaluza, 2012] Kaluza, M. (2012). private communication.

[Koppenhoefer, 2013] Koppenhoefer, M. (2013). Design eines Messaufbaus und Charakterisierung von Strahlführungsmagneten für einen Laser-Wakefield-Beschleuniger. Bachelor' Thesis.

[Kraemer et al., 2014] Kraemer, J., Baurichter, A., Budde, M., Bodker, F., Irman, A., Lehnert, U., Michel, P., and Schramm, U. (2014). Electron Beam Final Focus System for Thomson Scattering at ELBE. In *Proceedings of the IPAC 2014*, page THPRO055.

[Leemans et al., 2006] Leemans, W. P., Nagler, B., Gonsalves, A. J., Toth, C., Nakamura, K., Geddes, C. G. R., Esarey, E., Schroeder, C. B., and Hooker, S. M. (2006). GeV electron beams from a centimetre-scale accelerator. *Nature Physics*, 2(10):696–699.

[Leier, 2015] Leier, M. (2015). Evaluation of the Spectra. Internal Report.

[Letzelter, 2015] Letzelter, S. (2015). FLUKA-Studien zur Aufstreuung von Laser-Wakefield-beschleunigten Elektronenpaketen beim Durchgang durch verschiedene Materialien. Bachelor' Thesis.

[Lindau et al., 2008] Lindau, F., Lundh, O., Mangles, S. P. D., Kaluza, M. C., Krushelnick, K., Najmudin, Z., Persson, A., Thomas, A. G. R., and Wahlstrom, C. G. (2008). Characterization of quasi-monoenergetic electron beams at the lund laser centre. *Ieee Transactions On Plasma Science*, 36(4):1707–1714.

[Lundh et al., 2011] Lundh, O., Lim, J., Rechatin, C., Ammoura, L., Ben-Ismail, A., Davoine, X., Gallot, G., Goddet, J.-P., Lefebvre, E., Malka, V., and Faure, J. (2011). Few femtosecond, few kiloampere electron bunch produced by a laser-plasma accelerator. *Nat Phys*, 7(3):219–222.

[Machida and Fenning, 2010] Machida, S. and Fenning, R. (2010). Beam transport line with scaling fixed field alternating gradient type magnets. *Physical Review Special Topics-Accelerators and Beams*, 13(8):084001.

[MAD-X, 2002] MAD-X (2002). *MAD-X User's Guide*. CERN.

[Maier et al., 2012] Maier, A. R., Meseck, A., Reiche, S., Schroeder, C. B., Seggebrock, T., and Grüner, F. (2012). Demonstration Scheme for a Laser-Plasma-Driven Free-Electron Laser. *Phys. Rev. X*, 2:031019.

[Malka et al., 2008] Malka, V., Faure, J., Gauduel, Y. A., Lefebvre, E., Rousse, A., and Phuoc, K. T. (2008). Principles and applications of compact laser-plasma accelerators. *Nature Physics*, 4(6):447–453.

[Mangles et al., 2004] Mangles, S. P. D., Murphy, C. D., Najmudin, Z., Thomas, A. G. R., Collier, J. L., Dangor, A. E., Divall, E. J., Foster, P. S., Gallacher, J. G., Hooker, C. J., Jaroszynski, D. A., Langley, A. J., Mori, W. B., Norreys, P. A., Tsung, F. S., Viskup, R., Walton, B. R., and Krushelnick, K. (2004). Monoenergetic beams of relativistic electrons from intense laser-plasma interactions. *Nature*, 431(7008):535–538.

[Migliorati et al., 2013] Migliorati, M., Bacci, A., Benedetti, C., Chiadroni, E., Ferrario, M., Mostacci, A., Palumbo, L., Rossi, A. R., Serafini, L., and Antici, P. (2013). Intrinsic normalized emittance growth in laser-driven electron accelerators. *Phys. Rev. ST Accel. Beams*, 16:011302.

[Morcrette, 2012] Morcrette, M. (2012). Particle Beam Focusing in a Non-Planar Undulator. Master's thesis, Karlsruhe Institute of Technology (KIT).

[OPERA, 2014] OPERA (2014). Vector fields opera - electromagnetic simulation tool.

[Osterhoff et al., 2008] Osterhoff, J., Popp, A., Major, Z., Marx, B., Rowlands-Rees, T. P., Fuchs, M., Geissler, M., Hoerlein, R., Hidding, B., Becker, S., Peralta, E. A., Schramm, U., Gruener, F., Habs, D., Krausz, F., Hooker, S. M., and Karsch, S. (2008). Generation of stable, low-divergence electron beams by laser-wakefield acceleration in a steady-state-flow gas cell. *Physical Review Letters*, 101(8):085002.

[Plateau et al., 2012] Plateau, G. R., Geddes, C. G. R., Thorn, D. B., Chen, M., Benedetti, C., Esarey, E., Gonsalves, A. J., Matlis, N. H., Nakamura, K., Schroeder, C. B., Shiraishi, S., Sokollik, T., van Tilborg, J., Toth, C., Trotsenko, S., Kim, T. S., Battaglia, M., Stöhlker, T., and Leemans, W. P. (2012). Low-Emittance Electron Bunches from a Laser-Plasma Accelerator Measured using Single-Shot X-Ray Spectroscopy. *Phys. Rev. Lett.*, 109:064802.

[PTC, 2002] PTC (2002). *MAD-X User's Guide*. CERN. p. 209ff.

[Pukhov and Meyer-ter Vehn, 2002] Pukhov, A. and Meyer-ter Vehn, J. (2002). Laser wake field acceleration: the highly non-linear broken-wave regime. *Applied Physics B-Lasers And Optics*, 74(4-5):355–361.

[Rossbach and Schmueser, 1994a] Rossbach, J. and Schmueser, P. (1994a). *Basic Course on Acceleartor Optics*, volume 1, page 17ff. CERN.

[Rossbach and Schmueser, 1994b] Rossbach, J. and Schmueser, P. (1994b). *Proceedings of the CERN Acclerator School 1992*, volume 1, page 22f. CERN.

[Saevert, 2015] Saevert, A. (2015). Evaluation of the Images of the Unfocused Electron Beam. Internal Report.

[Sävert et al., 2015] Sävert, A., Mangles, S. P. D., Schnell, M., Siminos, E., Cole, J. M., Leier, M., Reuter, M., Schwab, M. B., Möller, M., Poder, K., Jäckel, O., Paulus, G. G.,

Spielmann, C., Skupin, S., Najmudin, Z., and Kaluza, M. C. (2015). Direct Observation of the Injection Dynamics of a Laser Wakefield Accelerator Using Few-Femtosecond Shadowgraphy. *Phys. Rev. Lett.*, 115:055002.

[Scheer, 2012] Scheer, M. (2012). Wave - A Computer Code for the Tracking of Electrons through Magnetic Fields and the Calculation of Spontaneous Synchrotron Radiation. In *Proceedings of the ICAP 2012*, page TUACC2.

[Schlenvoigt et al., 2008] Schlenvoigt, H. P., Haupt, K., Debus, A., Budde, F., Jackel, O., Pfotenhauer, S., Schwoerer, H., Rohwer, E., Gallacher, J. G., Brunetti, E., Shanks, R. P., Wiggins, S. M., and Jaroszynski, D. A. (2008). A compact synchrotron radiation source driven by a laser-plasma wakefield accelerator. *Nature Physics*, 4(2):130–133.

[Schlenvoigt et al., 2010] Schlenvoigt, H.-P., Jaeckel, O., Pfotenhauer, S. M., and Kaluza, M. (2010). Laser-based particle acceleration. In Grishin, M., editor, *Advances in Solid-State Lasers: Development and Applications*, chapter 24. InTech.

[Schnell et al., 2012] Schnell, M., Sävert, A., Landgraf, B., Reuter, M., Nicolai, M., Jäckel, O., Peth, C., Thiele, T., Jansen, O., Pukhov, A., Willi, O., Kaluza, M. C., and Spielmann, C. (2012). Deducing the Electron-Beam Diameter in a Laser-Plasma Accelerator Using X-Ray Betatron Radiation. *Phys. Rev. Lett.*, 108:075001.

[Schroeder et al., 2006] Schroeder, C. B., M., F. W., Esarey, E., and Leemans, W. P. (2006). Design of an XUV FEL Driven by the Laser-Plasma Accelerator at the LBNL LOASIS Facility. In *Proceedings of the FEL 2006*, page TUPPH055.

[Tomboulian and Hartman, 1956] Tomboulian, D. H. and Hartman, P. L. (1956). Spectral and Angular Distribution of Ultraviolet Radiation from the 300-Mev Cornell Synchrotron. *Phys. Rev.*, 102:1423–1447.

[Turner, 1998] Turner, S., editor (1998). *Insertion Devices: Undulators and Wigglers*, Proceedings of the CAS 1996 - Sunchrotron Radiation and Free Electron Lasers. CERN.

[Walker, 1983] Walker, R. P. (1983). Electron beam focusing effects and matching conditions in plane periodic magnets. *Nuclear Instruments and Methods in Physics Research*, 214(2–3):497–504.

[Wang et al., 2013] Wang, X., Zgadzaj, R., Fazel, N., Li, Z., Yi, S. A., Zhang, X., Henderson, W., Chang, Y.-Y., Korzekwa, R., Tsai, H.-E., Pai, C.-H., Quevedo, H., Dyer, G., Gaul, E., Martinez, M., Bernstein, A. C., Borger, T., Spinks, M., Donovan, M.,

Khudik, V., Shvets, G., Ditmire, T., and Downer, M. C. (2013). Quasi-monoenergetic laser-plasma acceleration of electrons to 2 GeV. *Nat Commun*, 4.

[Weingartner et al., 2012] Weingartner, R., Raith, S., Popp, A., Chou, S., Wenz, J., Khrennikov, K., Heigoldt, M., Maier, A. R., Kajumba, N., Fuchs, M., Zeitler, B., Krausz, F., Karsch, S., and Grüner, F. (2012). Ultralow emittance electron beams from a laser-wakefield accelerator. *Phys. Rev. ST Accel. Beams*, 15:111302.

[Werner, 2013] Werner, W. (2013). Design und Optimierung von In-Vakuum-Multipolmagneten für die Strahlführung am Laser-Wakefield-Beschleuniger in Jena. Master's thesis, Karlsruhe Institute of Technology (KIT).

[Werner, 2014] Werner, W. (2014). Library for the Control of Power Supplies in EPICS. https://github.com/wernwa/lwfa-las.

[Wiedemann, 2003] Wiedemann, H. (2003). *Particle Accelerator Physics I - Basic Principles and Linear Beam Dynamics*. Springer.

[Wiggins et al., 2010] Wiggins, S. M., Issac, R. C., Welsh, G. H., Brunetti, E., Shanks, R. P., Anania, M. P., Cipiccia, S., Manahan, G. G., Aniculaesei, C., Ersfeld, B., Islam, M. R., Burgess, R. T. L., Vieux, G., Gillespie, W. A., MacLeod, A. M., van der Geer, S. B., de Loos, M. J., and Jaroszynski, D. A. (2010). High quality electron beams from a laser wakefield accelerator. *Plasma Physics and Controlled Fusion*, 52(12):124032.